Ben Gurion University of the Negev

Faculty of Natural Sciences

Department of Physics

M.Sc Thesis

^{171}Yb Optical Lattice Clock in BGU

Submitted by: Yosef Bivas

I.D: 039883681

Supervisor: Prof. Ron Folman

A thesis submitted in fulfillment of the requirements for the degree of

Master of Science

June 2021

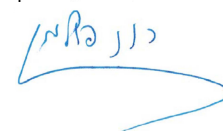# Ben Gurion University of the Negev

Faculty of Natural Sciences

Department of Physics

^{171}Yb Optical Lattice Clock in BGU

A thesis submitted in fulfillment of the requirements for the Master of Science degree Yosef Bivas under the supervision of Prof. Ron Folman

Signature of student: _____   _____   Date: _____30.06.2021_____

Signature of supervisor: _____   Date: _____30/6/2021_____

Signature of chairperson of the

committee for graduate studies _____   Date: _____

June 2021

Abstract

The last two decades have brought on several significant technological breakthroughs, which allowed improving the accuracy and stability of atomic clocks by about three orders of magnitude. Specifically, this is the result of probing optical transitions in a variety of rare earth elements rather than microwave transitions in the ground state of Rubidium and Cesium atoms. Hence the reference atomic frequency is about five orders of magnitude higher.

The systematic error budget that is reached by this type of clocks can be reduced down to a relative uncertainty of 10^{-18}, and the statistical instability can be also averaged down to a similar value within only several minutes of operation.

This unprecedented level of accuracy exhibited by the new clocks is orders of magnitude better than that of any other existing measuring device. Therefore, it is not only considered as an ultimate "frequency reference" but also as a sensor and a research tool for measuring gravity and exploring limits of theoretical predictions, including the foundations of quantum theory and relativity.

At the foreseeable state of advances in the field, accurate comparisons between different types of optical clocks could allow for a new definition of the SI second and other basic constants that can be derived from it, in the near future.

For the past two and a half years, I have been involved in the design and construction of the first optical lattice clock (OLC) in Israel. This clock is based on the $^1S_0 \rightarrow {}^3P_0$ optical transition in ^{171}Yb. This project is very engaging and challenging, but at the end, when the clock is fully operational, it will be an important achievement for the university as well as for the scientific community in Israel. Taking a major role in this project is very demanding in many aspects. On the other hand, this work is also satisfying as it is enabling me to develop my scientific skills and to contribute to the realization of an important cornerstone in a network of optical clocks in Israel.

In this thesis I provide a detailed description of my work in designing, computing, and building the ^{171}Yb OLC. This detailed documentation covers and explains all of the theoretical and technical aspects of the work. It is aimed to present my work to the scientific community and to help future students and researchers who join the clock team to learn about the system and about the fine details of its development.

The COVID-19 pandemic, which broke in Israel in March 2020, has slowed down the development work and although much was achieved, it is disappointing that some of the experimental innovations that we implemented in the clock system have yet to be tested at this stage. It is my intention that following the completion of this thesis I will complete the testing and hopefully publish some early results.

Acknowledgements

I'm a guitar
I used to be a tree, maybe
And in the resonance cavity
I remember everyone who played me
And I say - thank you…
(Naomi Shemer)

I would like to express my gratitude to everyone who supported me throughout this work.

I would first like to thank Prof. Ron Folman, who gave me the opportunity to join the Ytterbium clock team and to take part in this important and challenging project.

I would especially like to thank the head of the lab, Dr. David Grosswaser, who beyond his hard work in designing and building the clock, found the time and patience to assist and guide me in writing this work. I can't exaggerate the amount of time and patience that David has dedicated to my project.

Many thanks to Dr. Filippo Levi from INRIM, a real expert on clocks, who was kind enough to help us along the entire path of building the clock. Without Filippo, everything would have gone much slower.

Yaniv Bar-Haim, beyond being a talented, original, and creative technician whose fingerprints are felt in every part of the lab, you were for me a friend, and helped me a lot in orienting myself in the depths of the university and its paths. Thank you for that.

My gratitude also extends to all past and present members of the Atom Chip Group – Dr. Meny Givon, Dr. Omer Amit, Dr. Ketan Rathod, Dr. Yechezkel Schlussel, Eng. Mrs. Zina Binshtock, Or Dobkowski, Yossi Rosenzweig, Adi Kahana, Layla Eshet and everyone else who supported and assisted, some with good advice, some with help with calculations or technical help. Nice to work with people who are happy to give of their time and talent and help generously.

Great thanks is given to my dear parents, for educating me to be a good person and for the love of knowledge (especially physical knowledge ...), and for their great support throughout the years. Thanks also to all my teachers throughout my study years.

Finally, nothing of the past two and a half years would have been possible without the endless love and support of my dear wife Zehavit, who pushed me to come back to the academia and perfect and deepen my knowledge and understanding in physics. I thank you and love you so much.

List of Figures

viii

Abbreviations

ADEV……….…...	Allen deviation
AOM…………….	acousto-optic modulator
BBR…………….	black body radiation
BS………………..	beam splitter
CEO……………...	carrier-envelope offset
CF……………….	con-flat
DFG……………...	difference frequency generation
DPT…………….	differential pumping tube
ECDL…………….	external cavity diode laser
EOM…………….	electro optical modulator
FP……………….	Fabry Perrot
FSR……………...	free spectral range
FWHM…………	full width at half maximum
HWP…………….	half wave plate
IR……………….	infra-red
IUCC…………….	inter-university computation center
LBO……………...	Lithium triborate
LO……………….	local oscillator
MLL……………...	mode locked laser
MOT……………	magneto optical trap
OADM…………..	optical add/drop multiplexers
OFC……………...	optical frequency comb
OLC…………….	optical lattice clock
PBS……………...	polarize beam splitter
PD………………...	photo detector
PDH…………….	Pound Drever Hall
PID……………….	proportional integral derivative
PLL……………...	phase locked loop
PMT…………….	photo multiplayer tube
PPLN…………….	periodically poled lithium niobate
QWP…………….	quarter wave plate
RF……………….	radio frequency
ROC…………….	radius of curvature
SHG…………….	second harmonic generation
SQL……………...	standard quantum limit
TCE……………..	temperature coefficient of expansion
TOF…………….	time of flight
UHV…………….	ultra-high vacuum
ULE…………….	ultra-low expansion
VCO……………….	voltage-controlled oscillator

Contents

1. Introduction

1.1 The Development of Time Measurement

For thousands of years, humans have measured time in different ways. In ancient history, time was mostly measured by the motion of heavenly bodies, mainly the sun and the moon, which, in the wake of their motion, defined time constants - year, month, day, hour and second. More precise time measurement was achieved when the mechanical clocks were invented. For example, pendulum clocks enabled an accuracy with less than one minute of error per day. The 20th century heralded the introduction of the quartz clock. Its relative accuracy was improved to $2 \cdot 10^{-8}$, which is an error of less than one second per year.

1.2 Atomic Clocks

The Scottish physicist James Clerk Maxwell was perhaps the first person to recognize that atoms could be used to keep time. In his 1873 "Treatise on Electricity and Magnetism" he wrote, "A more universal unit of time might be found by taking the periodic time of vibration of the particular kind of light whose wavelength is the unit of length". There was no way of realizing this excellent idea in 1873, since the periodic time of light was much too short to be measured[1]. Maxwell remarkably suggested to William Thomson (Lord Kelvin) that the "period of vibration of a piece of quartz crystal" would be a better absolute standard of time than the mean solar second, but would still depend "essentially on one particular piece of matter, and is therefore liable to accidents." Atoms would work even better as a natural standard of time, as Thomson wrote in the second edition of his "Elements of Natural Philosophy", published in 1879[2].

Later, the atomic clock was invented, and it became the most accurate frequency standard in the world. Atomic ground-state microwave transitions are ideally suited for timekeeping, because the atom's energy levels are largely immune to environmental effects. Microwave radiation oscillates very fast (about 10 billion times per second) compared to the reference frequency of a crystal oscillator (about $1 - 100\,\mathrm{MHz}$), and therefore each time unit is divided into 100-10000 smaller parts, allowing for precision measurements of time and frequency. When microwave technology was applied to atomic spectroscopy, well defined atomic hyperfine resonances in alkali atoms started to be used as frequency standards. A basic operating scheme of such an atomic clock is depicted in Fig. 1.1.
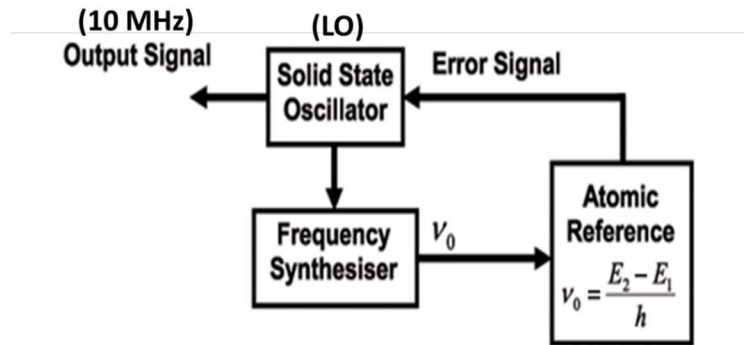
Figure 1.1: A conventional schematic diagram showing the working principle of an atomic vapor clock.

A tunable solid-state crystal oscillator (LO) is used to generate a reference frequency (typically 10 MHz) which is then used to synthesize the microwave frequency of the atomic resonance. The microwave radiation is applied on the atomic sample and generates population changes between the two clock states. This population difference is a measure for the deviation of the microwave frequency from the atomic resonance and can be used to generate an error signal for "locking" the output of the LO on the atomic resonance. In this case, any change in the LO output frequency is constantly detected and corrected.

The first accurate atomic clock, a Cs standard based on a certain transition of the caesium-133 atom, was built by Louis Essen and Jack Parry in 1955 at the National Physical Laboratory in the UK[3]. It is based on Ramsey interrogation (see chapter 2.3.2) of atoms that fly between two microwave antenna zones and during their time-of-flight (TOF) are not subjected to any applied disturbances by the driving microwave field. This kind of clock continues to be develop and improve, and with the combination of laser cooling techniques which evolved in the 1990's (Nobel Prize, 1997), led to the development of the fountain clock. In a fountain clock, a sample of ultra-cold atoms is launched upwards against the direction of gravity. As they travel up, they pass through a microwave antenna zone and after they reach the top of their trajectory they fall with gravity and pass through the same microwave region for the second time, realizing a longer TOF compared to a beam of "hot" atoms in a standard Ramsey beam clock.

In 1967, the Bureau International des Poids et Mesures (BIPM) defined the second 's' in standard international (SI) units according to the fixed numerical frequency of the unperturbed ground-state hyperfine transition frequency of the cesium-133 atom, which is 9,192,631,770 when expressed in the unit Hz [4], equal to s^{-1}.

The quality of a clock is mainly determined by two parameters: systematic uncertainty, typically called accuracy (the possible error of the measured transition frequency from its unperturbed value), and instability (the statistical precision that the clock exhibits in a measurement). The systematic uncertainty depends on physical experimental factors. For example, in OLCs, the leading terms that contribute to the systematic uncertainty are black body radiation (BBR) and collision shifts, as well as lattice light shift[5]. The statistical instability is usually measured by Allan deviation (ADEV), which is a measure of the correlation between one measurement interval and the one following it, and is given by[6]

$$\sigma^2(\tau) = \frac{1}{2(M-1)} \sum_{i=1}^{M-1} (\bar{y}_{i+1} - \bar{y}_i)^2, \tag{1.1}$$

where $\bar{y}_i$ is the average value of the i-th of M fractional frequency values averaged over the measurement (sampling) interval, τ. One can estimate the ultimate frequency stability of a frequency standard by[7]

$$\sigma(\tau) = \frac{1}{K} \frac{\Delta \nu}{\nu_0} \frac{1}{S/N} \sqrt{\frac{T}{\tau}}, \tag{1.2}$$

where K is a constant of the order unity that depends on the shape of the signal, T is the duration of one measurement cycle and τ is the interval averaging time (during the interval of averaging, τ, several cycles of measurements can be made). According to this equation, there are two quantities having a linear effect on the stability of the clock: the resonance quality factor ($Q = \nu_0 / \Delta \nu$) and the measurement signal-to-noise ratio (S/N). The quality factor is a dimensionless quantity that compares the width of a resonance, $\Delta \nu$, to its central frequency ν_0. The S/N is also dimensionless, and it gives information about the fidelity of each measurement. In general, there are many sources of noise that could diminish the S/N, but under certain conditions it is possible to reach the "Standard Quantum Limit" (SQL) of $S/N = \sqrt{N_{atom}}$, with N_{atom} being the number of atoms interrogated[8]. For example, an excellent Cs beam clock (ν_0= 9.192,263,770 Hz) with narrow linewidth of 1 Hz, and typical $N_{atom}= 10^6$, can reach an ADEV in the range of 10^{-13} after just 1 s of averaging time[9].

As noted, a considerable improvement in the accuracy of atomic clocks was made following the development of laser cooling technology. The short interrogation time of the Cs beam clock where the atoms pass between the two Ramsey zones at a speed of >300 m/s can be much extended. Therefore $\Delta \nu = 1/2T_{Ramsey}$ (see Sec. 2.3.2) can be significantly reduced, and Q is

improved. Here, T_{Ramsey} is the "dark" time between the two Ramsey zones. In addition, the slowing down of the atoms by the laser cooling process reduces the Doppler broadening and the total linewidth.

Today, the best fountain clocks are already working at their limit. The atom numbers are limited to about 10^6 atoms and the interrogation time is limited by the height of the fountain (~1 m). These constraints lead to a typical ADEV on the order of 10^{-13} in 1 s and long-term stability in the low 10^{-16} range [10]. The understanding that microwave fountain clocks are already operating at their limit spurred the search for new experimental systems that can beat the limitations imposed on previous generations of microwave clocks. In particular, the invention of the optical frequency comb in 2000[11] opened new possibilities for using optical instead of microwave transitions, so that Q can be improved by up to a factor of 10^5.

To compare completely different frequency standards, it is customary to use the relative quantity "fractional uncertainty", where the frequency uncertainty $\Delta\nu$ is divided by the central frequency ν_0. Unlike in the definition of Q, where $\Delta\nu$ is a fundamental limit derived from the width of the spectral line of the transition, equal to the natural linewidth of the atomic states, and in addition from the uncertainty principle limiting $\Delta\nu$ to one over the measurement (interrogation) time (sometimes referred to as the Fourier limited linewidth), here $\Delta\nu$ describes the practical uncertainty in the clock frequency, stemming from different noise sources. In general, statistical sources may be attenuated by statistical averaging. In such a case, we are left with systematic uncertainties. This is one of the reasons why the accuracy of a clock goes hand in hand with its stability, which allows for faster evaluations of systematic uncertainties[5]. Fig. 1.2 demonstrates the rate of improvement in the fractional uncertainty in optical clocks compared to microwave clocks. It is seen that the accelerated development of optical clocks allowed better fractional uncertainty values and that since 2007 optical clocks outperform the best microwave fountain clocks. Today the best optical clocks perform with about two orders of magnitude lower uncertainty relative to the best microwave fountain clocks.
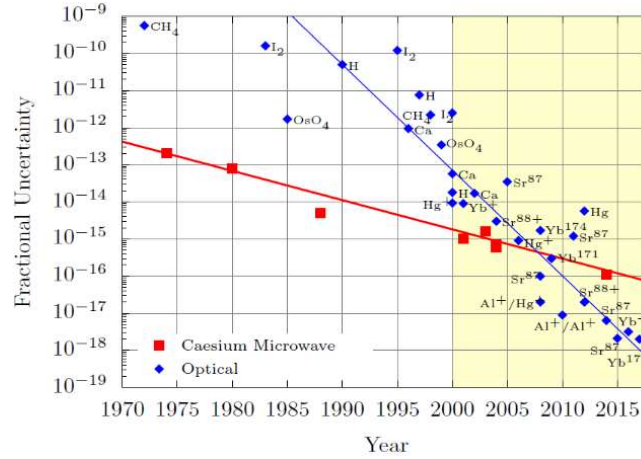
Figure 1.2: The improvement in the fractional uncertainty of optical and microwave clocks over the years.

1.3 Optical Clocks

As discussed above, the straightforward way to achieve higher stability is to improve the quality factor. This fact drives the motivation to investigate forbidden electronic transitions in the optical domain rather than microwave hyperfine ground state transitions. The change in the clock transition from the microwave to the optical domain accounts for a potential improvement factor of 100,000. Optical clocks thus offer tremendous advantages for improved time and frequency metrology. They are already used for a secondary definition of the SI second and it is expected that in the near future, they will be used to redefine it much more accurately[12,13]. In fact, we hope that the ^{171}Yb clock that is being developed in BGU will contribute to this definition in the future. Meanwhile, the BGU Atom-Chip Group is taking part in a European consortium under the EMPIR program, focused on robust optical clocks for international timescales (ROCIT)[14]. The ultimate goal of this program is for a new definition of the SI second based on a variety of optical clocks. For this purpose, the robustness of the clocks must be significantly improved and a program of accurate comparisons between remote clocks that are based on different atomic transitions must be performed. Although at this stage we aren't contributing to frequency comparisons, we are contributing to the development of robust subsystems such as an autonomous laser locking system and an error correcting system that monitors and adjusts the seeding of free-space laser beams into single mode optical fibers. Such systems are necessary for extending the maintenance-free operation times of the clocks. Operation reliability is a key parameter that is still needed to be improved for allowing such types of clocks to primarily define and represent the SI second. In this respect, it is important

to mention that only recently, NIMJ reported a continuous operation of ^{171}Yb clock for half a year[15].

The continuous improvements in accuracy and stability of optical clocks already enables scientists to set new limits to theoretical predictions and theories. For example, optical clocks can be applied to study the relationships between the quantum world and relativity[16-19], to set new limits on basic physical constants[20-22] and for searches for dark matter[23,24]. Further development of optical clocks seeks to enhance the miniaturization of the setup. Today, a typical optical clock setup can occupy a complete lab. However, there are efforts to produce mobile setups which can be used, for example, for geodesic surveys[25,26].

There are different types of optical clocks, but their basic principle of operation is similar, and they share similar components: A laser is electronically stabilized to a high-finesse and very stable optical cavity. This arrangement comprises the clock's local oscillator. The role of the optical cavity is to reduce the phase noise of the laser and to keep the short-term stability of the clock. In parallel, an atomic system serves as a long-term frequency reference and as a calibrating reference. Specifically, light from the stabilized laser is used to probe a narrow atomic resonance. If any drift occurs in the stable cavity, the spectroscopy which is applied on the atomic system will identify it and provide an evaluation of its magnitude. Accordingly, a correction signal will be implemented on the output beam that exits from the clock. The corrections are implemented by using an acousto-optical modulator (AOM) and the output beam is used to lock a frequency comb.

One of the main obstacles in the realization of optical clocks is the need to down-convert (so called frequency division) from optical to microwave and RF frequencies, to be used by electronic devices without degradation of the stability and accuracy provided in the optical domain. This frequency gap is also one of the reasons why the development of optical clocks was delayed, until the early 2000s, when the frequency comb was invented (Nobel Prize, 2005).

During the 2000's, the field of clocks based on optical transitions has rapidly evolved[27], first with ions, and later with trapped neutral atoms[28]. In ion clocks a single ion is trapped and cooled in an ion trap[7], while clocks that are based on neutral atoms make use of a lattice potential at a "magic frequency" to trap thousands of atoms at once[7]. Currently, the ^{171}Yb+ ion clock[29] exhibits a systematic uncertainty of $3.2 \cdot 10^{-18}$, and OLCs with neutral atoms[30] have reached a record frequency stability of $3.2 \cdot 10^{-19}$ and systematic uncertainty of $1.4 \cdot 10^{-18}$.

As noted, to this date, the ultimate systematic uncertainties of ion clocks and OLCs are very similar. However, the neutral atomic clocks can reach much better stability values at short averaging times thanks to the large number of trapped atoms that can be investigated simultaneously. Future improvements to the optical clock include attempts to improve the stability of ion clocks by capturing several dozen ions simultaneously while masking their interaction[31]. On the other hand, the accuracy of lattice clocks that trap thousands of neutral atoms is also pushed to new limits by further reduction of the BBR uncertainty[5,32] as well as by reducing inter-atomic interactions [33].

1.4 The Ytterbium (Yb) Atom

^{87}Sr and ^{171}Yb are the two most common realizations of OLCs. First, both are fermions which are favored over bosons due to the fact that bosonic atoms might be found in a common lattice site and the shift is then dominated by collisions. This situation is minimized with fermions at low temperatures, and theoretically can even be totally avoided in a 3D lattice. The reason is that in a 3D lattice, each site occupies only one atom due to the Pauli exclusion principle[34]. For a 1D optical lattice, the two-dimensional lattice sites typically have multiple occupancy and the use of fermionic isotopes at ultracold temperatures is advantageous since the wavefunctions for identical fermions eliminate collisions from even partial-wave collision channels, including the lowest order s-wave. At the same time, the lowest odd-wave (p-wave) collisions can be suppressed at sufficiently low temperatures. This fermionic resistance to cold collisions (and collision shifts) makes fermions particularly good candidates for atomic frequency standards[35].

In addition, both atoms have narrow (forbidden) electronic transitions (1 mHz for ^{87}Sr and 10 mHz for ^{171}Yb in the optical domain; ^{87}Sr clock transition: $\lambda_{clock}^{Sr} = 698$ nm and ^{171}Yb clock transition: $\lambda_{clock}^{Yb} = 578$ nm)[36] which are essential for a high Q-factor. However, it is important to note that if the transition is totally forbidden, it will be impossible to excite. Hence, the transition symmetry must be broken by some atomic interaction, so that the transition probability will be finite. A forbidden singlet-triplet electronic transition in an element having two electrons in the external shell is a logical choice. The two clock states are the $^1S_0$ (singlet ground state) and the $^3P_0$ (triplet excited state). The radiative transition between these two levels is both spin- and dipole-forbidden: the number to the left of P and S represents the spin quantum number (and equals 2s+1), while the number to the right represents the total electronic angular momentum of the atom, J. According to selection rules, both $\Delta s \neq 0$ and J=0 $\rightarrow$ J=0 are forbidden transitions[7]. In addition, it is important to choose an odd isotope of those elements, also because the symmetry-breaking of the $^3P_0$ state due to the hyperfine interaction with the

nuclei spin which in turn promotes mixing of the $^3P_0$ level with other nearby states resulting in a hyperfine-quenched $^3P_0$ lifetime of several tens of seconds[37]. These odd-mass-number fermionic isotopes are less abundant than the (spin-0) even-mass-number isotopes, but usually have enough natural abundance to carry out experiments. (The natural abundance[38] of ^{171}Yb is 14.3%).

While the nuclear spin is beneficial for its hyperfine quenching and resistance to cold collisions, it entails several other effects that could be deleterious for high-precision spectroscopy. The clock states are no longer purely $J = 0$, but instead should be labelled by their total angular momentum $F = J + I$. This effect creates $2I + 1$ substates in both the ground and excited clock states, each substate with its own sensitivity to magnetic fields through the Zeeman effect. With Sr, for example, the only abundant odd isotope has $I = 9/2$, for which the complexity associated with these effects is substantial.

Second, the spherical symmetry of the $J = 0$ state is partially lost, which allows for a small interaction between the atom and the polarization of the lattice light field. These concerns led researchers to revisit the idea of the ($I = 0$) even isotopes. Several theoretical proposals showed[39-41] that the addition of an external field (either another light field or a magnetic field) could dramatically increase the transition strength without significantly perturbing the clock transition frequency. The trade-off, then, is between the simplicity of a pure two-level system for which we must calibrate the substantial frequency shift of the external field, or the benefits of the odd isotope transition, that comes with the additional complexity of nuclear substructure. But suppose the nuclear spin is small, $I = 1/2$ being the smallest. Then, there are only two ground states and two excited states, between which we could drive two π-transitions or two σ-transitions. This makes first-order Zeeman shifts and optical pumping more straightforward to control. Moreover, one can show that one of the substate-dependent light shifts (namely the tensor shift) is absent for this special case. Thus, the ^{171}Yb spin-1/2 isotope enjoys many of the benefits of both higher- and zero-angular momentum systems and is ideally suited for high-accuracy optical spectroscopy[8].

In addition to all this, and as noted above, one of the most influential contributors to the clock uncertainty is the black body radiation coming from the clock's environment. Calculations show that the contribution to uncertainty arising from this effect at room temperature (300K) is not negligible when it comes to fractional uncertainties on the order of 10^{-18}. Recent studies show, however, that compared to ^{87}Sr and ^{199}Hg, ^{171}Yb clocks have the lowest sensitivity to

variations in ambient temperature in terms of BBR[42]. This uncertainty can be reduced to a level of $1 \cdot 10^{-18}$ by careful regulation of the temperature homogeneity and stability of the vacuum chamber[43]. Alternatively, the atoms in the lattice can be transferred to a cryogenic cell for the duration of the interrogation step in the experimental cycle[44]. The motivation for this approach is the T^4 dependence of the BBR shift[45].

^{171}Yb has some other useful accessible optical transitions that are required for performing primary and secondary cooling (reaching a Doppler limit of several micro-kelvin), as well as for detection and for repumping the atoms from the metastable $^3P_0$ state to the ground state during the detection phase. Furthermore, ^{171}Yb exhibits a magic wavelength, which allows trapping the atoms in the lattice while maintaining the energy difference of the clock transition unperturbed[46,47]. All relevant wavelengths are shown in Fig. 1.3.

Several OLCs based on ^{171}Yb atoms have been developed in national metrological institutes like the National Institute of Standards and Technology (NIST) in the USA, the National Metrological Institute of Japan (NMIJ-AIST) and RIKEN in Japan, the Korea Research Institute of Standards and Science (KRISS) and the Istituto Nazionale di Ricerca Metrologica (INRIM) in Italy. One Yb lattice clock is in use at MIT[46], focused on improving the stability by generating entanglement between the atoms, which will hopefully will enable overcoming the standard quantum limit towards the Heisenberg limit[48].

For all the above reasons, we decided to base the BGU optical clock on ^{171}Yb atoms. This is the first OLC to be developed in Israel and the second optical clock following the ^{87}Sr+ ion clock developed in the group of Roee Ozeri at the Weizmann Institute[49]. We hope that with this clock we will be able to conduct various experiments in fundamental physics in the coming years. It is also planned that this clock will serve as a primary node in an optical network for distribution of time and frequency standards in Israel, which will allow for improved synchronization and research by state-of-the-art frequency comparisons.

To conclude, Yb is an element with atomic number 70, which is the second last lanthanoid element that has a closed 4f shell and two electrons filling the outermost 6S orbital. There are seven stable isotopes of Yb. Because the atomic number is even, nuclear spin is nonzero only for fermionic isotopes, ^{171}Yb and ^{173}Yb. The electronic structure and the relevant atomic transitions of ^{171}Yb are described in Fig. 1.3.
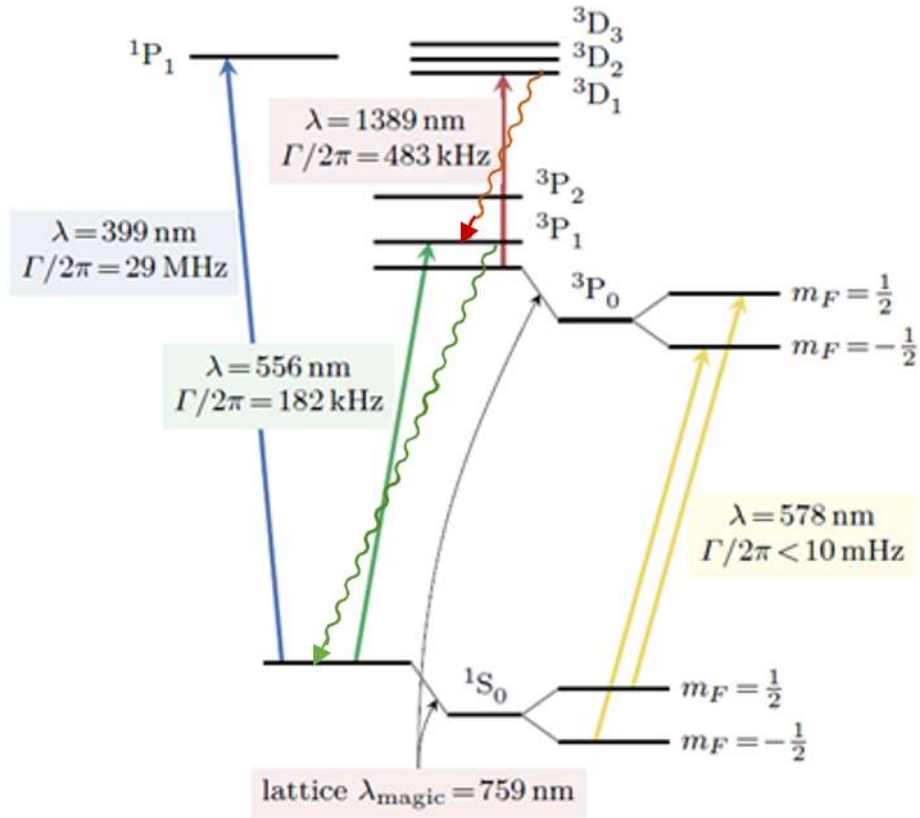
Figure 1.3: Relevant energy levels for ^{171}Yb including the hyperfine splitting of the clock transition. The $^1S_0 \rightarrow ^3P_0$ transition is the clock transition at λ=578 nm (yellow laser, see Sec. 7.5) with Γ<10 mHz. The $^1S_0 \rightarrow ^1P_1$ strong transition at 399 nm (blue laser, see Sec. 7.1) is used for first stage laser cooling and for detection. The $^1S_0 \rightarrow ^3P_1$ transition at 556 nm (green laser, see Sec. 7.2) is used for second stage cooling in a 3D MOT and for spin polarization. The 1389 nm laser light (Sec. 7.4) is used for repumping during the spectroscopy stage (the wavy arrows represent decay of the repumped atom from the $^3D_1$ state to the ground state, via the $^3P_1$ state). The 759 nm (Sec. 7.3) is the 'magic wavelength' for the optical lattice trapping potential.

In the following chapters of this thesis, I will describe our clock system and its operating principles in detail.

2. Theoretical Background

2.1 Atom Cooling & Trapping

2.1.1 Laser Cooling

According to the principle of momentum conservation, an atom can be slowed down by absorbing light, if it moves in the opposite direction to a resonant laser beam. The atom will then absorb photons from the beam, with every such absorption being associated with a quanta of momentum transfer $\hbar \boldsymbol{k}$. In the above scenario, this momentum "kick" is always in the opposite direction to the atom's direction of propagation. However, the spontaneous emission which follows each absorption occurs in random directionality. Therefore, the net force after many such cycles resembles a friction force. The atom is effectively slowed down ("cooled") by the laser beam. One can estimate the deceleration of the atom according to this process as the absorption rate multiplied by the photon momentum[50]

$$\boldsymbol{a} = \hbar \boldsymbol{k} \frac{\Gamma}{2m} \frac{I/I_S}{1+I/I_S+(2\Delta/\Gamma)^2}. \tag{2.1}$$

Here, Γ is the linewidth of the excited state, m is the mass of the atom, I and I_S are the laser light and saturation intensities, and Δ is the detuning of the laser frequency from resonance. If $I \gg I_s$, and Δ is small relative to Γ, the deceleration is approximated to be $\boldsymbol{a}_{max} = \hbar \boldsymbol{k} \frac{\Gamma}{2m}$. This limit is set by the spontaneous emission rate, or excited state lifetime $1/\Gamma$, which determines the number of scattered photons per unit time. The factor ½ is a consequence of the saturation regime where the laser intensity is so high, that as soon as the atom decays, it is immediately re-excited. This means that the populations of ground and excited states approach ½. To quantify this force, we can consider ^{171}Yb ($m \simeq 2.86 \cdot 10^{-25}$ kg) atoms with the $^1S_0 - {}^1P_1$ transition at $\lambda = 2\pi/k = 399$ nm and $\Gamma/2 = \pi \cdot 29$ MHz $\simeq 9 \cdot 10^7$ photons scattered per second at saturation. The resulting acceleration is $\boldsymbol{a} \simeq 5 \cdot 10^5$ m/s^2 which is about 50,000 times larger than the Earth's gravitational acceleration. For comparison, the $^1S_0 - {}^3P_1$ transition at $\lambda = 556$ nm and $\Gamma/2 = \pi \cdot 182$ kHz $\simeq 5.7 \cdot 10^5$, has a resulting maximal acceleration of just $\boldsymbol{a} \simeq 2.3 \cdot 10^3$ m/s^2. We will explain further on why this latter transition is also used in the cooling process, although it is apparently much less effective.

The use of pairs of counter propagating laser beams with the same intensity and detuning ($\Delta < 0$) allows slowing the atoms as well as narrowing the velocity distribution in the direction of the laser beam. This is primarily because Δ is velocity dependent via the Doppler effect.

Including the Doppler shift $\Delta_D = \omega_0 v/c = kv$, the force exerted on the atoms by two identical counter propagating beams at frequency ω is

$$\boldsymbol{F} = \hbar \boldsymbol{k} \frac{\Gamma}{2} \left[\frac{I/I_s}{1+[4(\omega-\omega_0-kv)^2]/\Gamma^2} - \frac{I/I_s}{1+[4(\omega-\omega_0-kv)^2]/\Gamma^2} \right]. \tag{2.2}$$

This equation shows that an atom at rest will experience no force from the laser beams. While, if the atom is moving towards one of the two beams, the balance between the scattering rates is violated and it will experience a force countering the direction of its motion. Let us emphasize, that the probability of absorbing photons from the beam co-propagating with the atom's velocity is very low due to the red-detuning ($\Delta < 0$) of the laser beams.

Expanding this force for small velocities gives

$$\boldsymbol{F} \cong -\alpha \mathbf{v} + \mathcal{O}(\mathbf{v}^3), \tag{2.3}$$

which corresponds to a friction force with damping coefficient

$$\alpha = -8\hbar k^2 \frac{I}{I_s} \frac{\Delta/\Gamma}{1+(2\Delta/\ )^2}. \tag{2.4}$$

This friction force is indeed positive for $\Delta < 0$ and it maximized for $\Delta = -\Gamma/2$. This kind of arrangement is called *optical molasses*.

The concept of laser cooling implicitly refers to the temperature of the atomic sample. Since the system is not in thermal equilibrium, but rather in a steady-state regime where the atoms are in continuously interaction with the light, the temperature is not trivially defined. From the equipartition theorem we can express an effective temperature from the averaged squared velocity $\langle v^2 \rangle$ of the atomic ensemble in the optical molasses as

$$\frac{1}{2} k_B T = \frac{1}{2} m \langle v^2 \rangle. \tag{2.5}$$

A steady state is achived when the radiation pressure force equals the heating effects that are caused by the atom recoil after spontaneous emissions together with fluctuation in the intensity of the laser beams. This sets a lower temperature limit called the Doppler temperature

$$T_D = \frac{\hbar \Gamma}{4k_B} \frac{1+(2\Delta/\Gamma)^2}{(2\Delta/\Gamma)}, \tag{2.6}$$

which is minimized for $|\Delta| = \Gamma/2$ (tantamount to maximal damping force) giving

12

$$T_D^{min} = \frac{\hbar\Gamma}{2k_B}. \tag{2.7}$$

The Doppler limit is a useful tool to estimate the lowest temperature as a function of the atomic transition linewidth. Getting back to the ^{171}Yb example, the strong $^1S_0 - {}^1P_1$ transition has a linewidth of $\Gamma = 2\pi\cdot 29\,\text{MHz}$, obtaining $T_D^{min} \simeq 700\,\mu\text{K}$. However, if we laser-cool on the weaker (spin forbidden) $^1S_0 - {}^3P_1$ transition that has a linewidth of $\Gamma = 2\pi\cdot 182\,\text{kHz}$, we will reach a much lower temperature $T_D^{min} \simeq 5\,\mu\text{K}$.

2.1.2 Magneto Optical Trap (MOT)

So far, we showed how to reduce the average velocity of an atomic ensemble by laser radiation and thus cool it. But, if we want to control the cloud position, and increase its density, it is not enough. In addition to the friction force, we also need to apply a restoring force which will keep the atoms close to one point in space. This can be achieved by adding a magnetic gradient and taking advantage of the Zeeman interaction. While light also provides the restoring force, the Zeeman interaction provides the necessary selection rules.
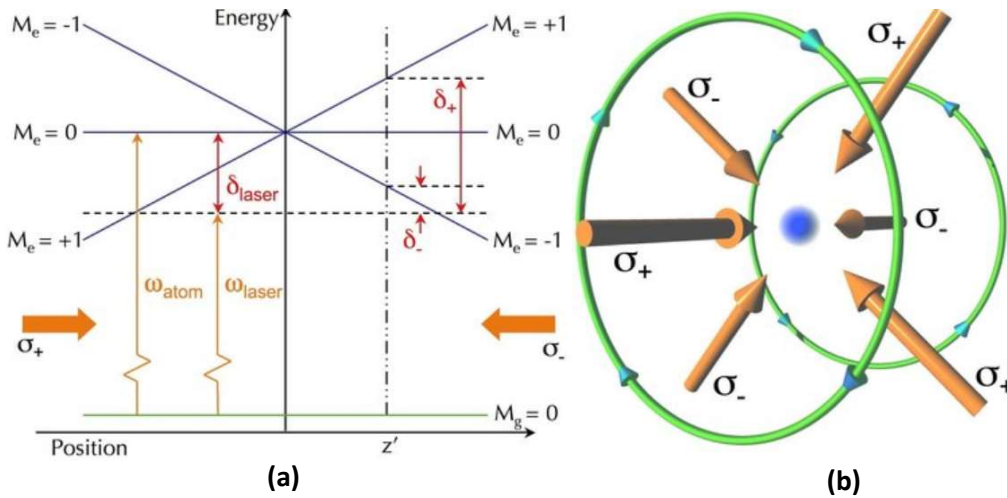
Figure 2.1: (a) A simplified picture of laser cooling and trapping of an arbitrary atom having a ground state hyperfine level Fg=0 and a Zeeman state Mg=0. In the presence of a magnetic field, the degenerate excited state hyperfine level Fe=1 is split to three Zeeman levels Me=-1, 0, +1. An atom moving to the left or to the right from the center will experience a restoring force by absorbing light from only one direction. (b) A schematic description of anti-Helmholtz coils with the six laser beams' direction and polarization, creating a 3D MOT. The polarizations are in the laboratory frame. In the frame of the local magnetic field (local quantization axis), the two beams on the quadrupole axis should have the same polarization, and all 4 additional beams should have the opposite polarization.

Considering a simple 1D case, the presence of an inhomogeneous external magnetic field of the form B(z) = b·z which changes its sign at the origin, induces a linear spatially dependent Zeeman splitting of the atomic levels that nulls at z = 0. In the hypothetical case of an atom with total angular momentum M_g = 0 for the ground and M_e = 1 for the excited state, the external magnetic field will remove the degeneracy and split the excited levels to three by the Zeeman effect

$$\Delta E(z) = g_F \mu_B M_e B(z), \tag{2.8}$$

where g_F is the Landé factor for the excited state, μ_B is the Bohr magnetron and M_e = 0, +1 or -1 are the possible projections of the total angular momentum along the magnetic field axis. The spatial gradient of the external magnetic field causes the atomic resonance to become space dependent.

Fig. 2.1(a) shows a configuration of two red-detuned, counter-propagating laser beams of opposite circular polarizations, with a Zeeman shifted excited state, that is used to ensure that atoms propagating away from the center, absorb photons from only one side, giving them a recoil in the direction of the center. In Fig. 2.1(b) we demonstrate how a 3D magnetic gradient with zero at the origin is realized by a pair of anti-Helmholtz coils. In this configuration the currents in the two coils are flowing in opposite directions, thus generating a zero field right in the middle between the coils on the axis connecting the centers of each coil. As a result, the direction of the magnetic field along each of the three axes is flipping at the origin.

With the addition of the Zeeman shift to Eq. 2.2, the radiation force is always directed toward the center of the trap. It can be quantitatively expressed as

$$\boldsymbol{F} \cong \hbar\boldsymbol{k}\frac{\Gamma}{2}\left[\frac{I/I_s}{1+[4(\omega-\omega_0-k\mathrm{v}-g_F\mu_B bz/\hbar)^2]/\Gamma^2} - \frac{I/I_s}{1+[4(\omega-\omega_0+k\mathrm{v}+g_F\mu_B bz/\hbar)^2]/\Gamma^2}\right]. \tag{2.9}$$

Expanding this equation for small **z** and **v** we obtain

$$\boldsymbol{F_z} \cong -\alpha\mathbf{v} - \kappa\boldsymbol{z} \text{ , with } \kappa = \frac{g_F\mu_B b}{\hbar k}\alpha \text{ and } \alpha = -8\hbar k^2\frac{I}{I_s}\frac{\Delta/\Gamma}{1+(2\Delta/\ )^2}, \tag{2.10}$$

which is the equation of a damped harmonic oscillator with spring constant κ. The method can be extended in the 3D case by using three pairs of counter-propagating polarized laser beams along the three orthogonal axes, and a quadrupole magnetic field generated by a pair of anti-Helmholtz coils [see Fig. 2.1(b)]. In this setup which is called a magneto optical trap (MOT),

the atoms are both cooled and trapped. To conclude, thermal atomic vapor in ultra-high vacuum chambers (pressure $< 10^{-9}$ torr) can be cooled and its density may be increased. After a brief loading time, the MOT reaches its steady state when the number of atoms lost mainly due to collisions with residual gas particles equals the rate of collecting atoms from the background vapor.

In the case of ^{171}Yb, the MOT is realized in two stages. In the first stage we use a "blue" 399 nm 2D MOT, operating on the strong $^1S_0 - {}^1P_1$ transition, for slowing the atoms along two axes. This transition has a large capture range in velocity due to the short lifetime of the transition. This stage is necessary for preventing the atoms from exiting the cooling zone, but on the other hand, the Doppler limit is high ($\simeq 700\,\mu K$) and the atoms' temperature is not cold enough for trapping them in the lattice potential. This is the role of the second 3D "green" cooling stage at 556 nm, which does not cause strong acceleration, and allows for a much lower temperature limit ($\simeq 5\,\mu K$).

2.2 Optical Lattice for Atomic Frequency Reference

2.2.1 Optical Lattice and the 'Magic Frequency'

After the first and second cooling stages, the atoms are cold enough for trapping them in an optical lattice potential with a spatially periodic intensity pattern, created by a standing wave, typically made by counter-propagating beams, or as in our case, a cavity. The optical potential is a result of the induced dipole interaction with the electric field of the focused laser beams.

In the presence of laser light at frequency ω and electric field $E(\omega)$, an atom experiences an AC Stark potential[7,33]

$$U_i(\omega) = -\frac{1}{4}\alpha_i(\omega)|E(\omega)|^2 = -\frac{1}{2\varepsilon_0 c}\alpha_i(\omega)I, \qquad (2.11)$$

where $\alpha_i(\omega)$ is the real part of the induced polarizability of the atom in state i, and $I = \frac{1}{2}\varepsilon_0 c|E(\omega)|^2$ is the laser intensity. If there is an intensity gradient, a dipole-force is applied on the atom

$$\boldsymbol{F} = \frac{1}{2\varepsilon_0 c}\alpha_i(\omega)\vec{\nabla}I. \qquad (2.12)$$

According to the fact that α_i depends on the laser detuning, this force is directed towards the high intensity area in the case of red-detuning and in the opposite direction in the case of blue-detuning (the detuning is with respect to the resonance frequency between two atomic levels).

A focused laser beam can trap thousands of atoms at high densities. However, this situation is not favorable for achieving an accurate atomic clock due to the uncertainty that is associated with the interactions and the collisional shifts between the atoms. The way to circumvent this situation is to load low density atomic samples into an optical lattice potential that is created in the waist of the laser standing wave. As a result, every lattice site will hold very few atoms (possibly only one), and thus the collisional uncertainty can be significantly reduced. The three possible optical potentials are: 3D lattices, which generate an "egg-crate" shaped configuration; 2D potential which results in "cigar" shaped traps; and a 1D lattice that creates traps in the shape of "pancakes" every half wavelength.

The 1D lattice potential is the easiest and most common configuration to produce, in most cases it is also sufficient as collisional shifts become smaller compared to other possible uncertainties, such as BBR. Naturally, we plan to use a 1D lattice potential in the early stages of our clock development and modifications are considered as will be discussed later in the outlook.

A 1D optical lattice potential can be easily achieved by retroreflecting a focused laser beam as depicted in Fig. 2.2. Every half a wavelength, this lattice potential has alternating regions of high and low light intensities in the shape of "pancakes". In the case of red-detuned light, the atoms will be attracted to the high intensity regions on the one-dimensional lattice. Alternatively, the lattice can be generated inside a Fabry-Perot (FP) resonator and achieve significantly higher intensities.
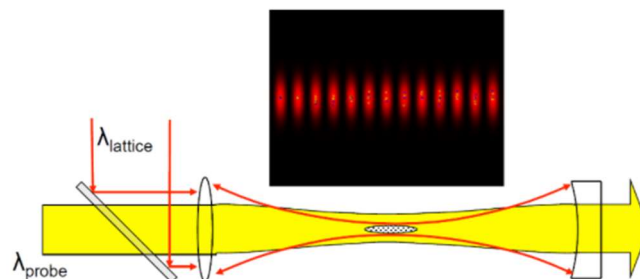
Figure 2.2: A conventional optical array for creating a 1D lattice. A focused Gaussian laser beam is retroreflected by a curved mirror. At the top – repeating "pancake" shaped nodes and anti-nodes of light intensity every half a wavelength.

The lattice configuration makes it possible to hold thousands of atoms in thousands of lattice sites. This property is important for achieving high S/N. In addition, relative to free-falling atoms in a similar-sized chamber, the atoms can be trapped in such a lattice for a long time, thus allowing high Q. The tight confinement (high trapping frequency) suppresses the Doppler

shift thus reducing this uncertainty. All of these factors contribute to the unprecedented stability of the clock (see Eq. 1.2). Let us also mention here that the high trapping frequencies made available (in 1D) by the lattice, enable side-band cooling (see Sec. 2.2.2).

It is also worth noting that when the trap frequency is higher compared to the recoil energy, there will be no heating during the probing or detection of the atoms (so-called Lamb-Dicke regime). This is another important benefit of a 3D lattice configuration, where the potential is tight in any direction, and thus absorption or emission recoil cannot excite the atoms. One can present the 1D lattice as an attractive potential of the form

$$U_{(z,\rho)} = -U_0 cos^2(2\pi z/\lambda)e^{-2\rho^2/\rho_0^2}, \tag{2.13}$$

where z and ρ are the longitudinal and radial coordinates respectively, U_0 is the trap depth (at the center of the Gaussian beam and at the central anti-node point of the standing wave), and ρ_0 is the beam waist radius. The trap depth can be deduced from the (one pass) optical power P as[7]

$$U_0 = \frac{4\alpha_i(\omega)P}{c\varepsilon_0\rho_0^2}. \tag{2.14}$$

The dipole interaction giving rise to the AC Stark shift is used for trapping the atoms in a lattice, but it creates a new problem for the frequency calibration of the standard: The position and time dependent intensity variations in the trapping field, will perturb the clock transition in an uncontrolled manner.

The frequency Stark shift to state i is

$$\Delta\omega_i = -\frac{1}{2\hbar}\alpha_i(\omega_L,\vec{e})E_0^2, \tag{2.15}$$

$\alpha_i(\omega_L,\vec{e})$ being the atomic polarizability tensor in direction $\vec{e}$ in response to the laser frequency ω_L, and E_0 is the amplitude of the electric field of the laser light.

The frequency difference between the ground and the exited states becomes[47]

$$\widetilde{\omega}_{eg} = \omega_{eg} - \frac{1}{2\hbar}\Delta\alpha_{eg}(\omega_L,\vec{e})E_0^2 + \mathcal{O}(E_0^4), \tag{2.16}$$

where $\Delta\alpha_{eg} = \alpha_e - \alpha_g$ is the difference of dipole polarizabilities between both states.

It is practically impossible to stabilize the laser intensity so as to make this shift constant in time. Furthermore, because of the intensity gradient in the trap, this shift is also position dependent. In 2002, H. Katori proposed to tune the lattice frequency to null the polarizability difference by operating the lattice at a "magic frequency"[28,51]. at which $\alpha_e(\omega_{magic}) = \alpha_g(\omega_{magic})$, and so $\Delta\alpha_{eg} = 0$. Fig. 2.3 shows the polarizabilities of the $^1S_0$ and $^3P_0$ clock states in the ^{171}Yb atom. The magic wavelength occurs at 759.35596 nm[8]. In addition, it has been demonstrated that the scalar nature of the clock states (J = 0) gives a negligible dependency on the polarization of the lattice light, and consequently we can drop the $\vec{e}$ dependency of the scalar polarizability.
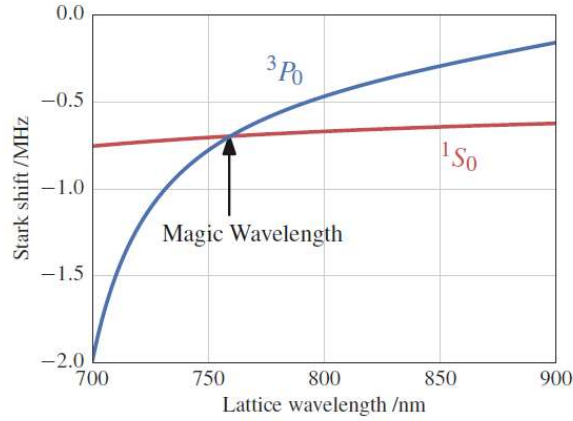
Figure 2.3: AC Stark shift on the clock ground (red) and excited (blue) states in ^{171}Yb. The cross point at λ~759 nm is the 'magic wavelength'. In addition, one can see the weak dependence of the ground state shift on the lattice wavelength in comparison to the excited state shift. Taken from[47].

When approaching fractional uncertainties below the 10^{-16} level, the concept of zero differential Stark shift breaks down and higher order corrections need to be considered[52]. $\mathcal{O}(E_0^4)$ in Eq. 2.16 is the second order term that contributes to the Stark shift. Taking this term into account gives

$$\widetilde{\omega}_{eg} = \omega_{eg} - \frac{1}{2\hbar}\Delta\alpha_{eg}(\omega_L)E_0^2 + \frac{1}{64\hbar}\Delta\gamma_{eg}(\omega_L, \vec{e})E_0^4. \tag{2.17}$$

The second order shift is characterized by the difference between hyperpolarizabilities of the upper and lower states, $\Delta\gamma$, coming from two-photon interactions close to the magic wavelength. Even though the scalar term is nulled at the magic wavelength, the quadratic term still introduces a shift of about 10^{-17} to the clock transition, which, if not properly controlled, can limit the accuracy of the standard[53].

2.2.2 Sideband Cooling in an Optical Lattice

The potential of the Stark interaction described in Eq. 2.13 is approximated as:

$$U(z,\rho) \approx U_0 \left[\left(\frac{2\pi z}{\lambda} \right)^2 + \frac{2\rho^2}{\rho_0^2} \right] = \frac{1}{2} m\omega_z^2 z^2 + \frac{1}{2} m\omega_\rho^2 \rho^2 \qquad (2.18)$$

with $\omega_z \equiv \frac{2\pi}{\lambda} \sqrt{\frac{2U_0}{m}}$ and $\omega_\rho \equiv \frac{1}{\rho_0} \sqrt{\frac{2U_0}{m}}$, where m is the atom mass. The variation of the intensity along the longitudinal z direction is much greater compared to that in the transverse directions, and effective sideband cooling is performed along this axis. The well-known (longitudinal) energy levels are:

$$E_n = \hbar\omega_z(n + 1/2), \qquad (2.19)$$

where the integer n is the vibrational quantum number. The atomic wavefunction can be divided into two parts: the electronic part (internal degree of freedom) and the motional part (external degree of freedom). The energy levels of the trapped atoms are also described separately. Consequently, when the trapped atoms are probed by a laser sent along the lattice axis, they can make purely electronic transitions $|g, n\rangle \rightarrow |e, n\rangle$ at the electronic transition frequency ω_0, or can exchange a quantum of motion $|g, n\rangle \rightarrow |e, m\rangle$ at frequency: $\omega_0 + (m-n)\omega_z$. Let us define η, called the 'Lamb-Dicke parameter', as the square root of the ratio between the recoil energy of an atom exchanging a photon at the probing light resonance ω_0, and the energy spacing between the longitudinal harmonic oscillator levels:

$$\eta = \sqrt{\frac{\hbar\omega_{Recoil}}{\hbar\omega_z}} = \frac{2\pi}{\lambda} \sqrt{\frac{\hbar}{2m\omega_z}} = 2\pi \frac{\Delta z}{\lambda} , \qquad (2.20)$$

where Δz is the ground state size of the harmonic potential. If $\eta \ll 1$, the atom is in the "Lamb-Dicke regime" where it is trapped in a region smaller than the wavelength of the probing transition. In this regime, the dominant motional transitions are $\Delta n = 0, \pm 1$ [54]. Furthermore, under these conditions, the atoms are not heated up in the lattice due to recoil. Sideband cooling is performed on the clock transition with a narrow linewidth laser ~ 1 Hz, while the typical motional frequency in the lattice ω_z is in the order of a few kHz. The situation occurring when the transition linewidth is much smaller than the motional frequency is called "resolved sideband cooling".

The possible motional transitions in the Lamb-Dicke regime are shown in Fig. 2.4(a), and their relative amplitudes in Fig. 2.4(b). The relative amplitude of the motional sidebands carries information about the average occupancy of the motional energy levels.
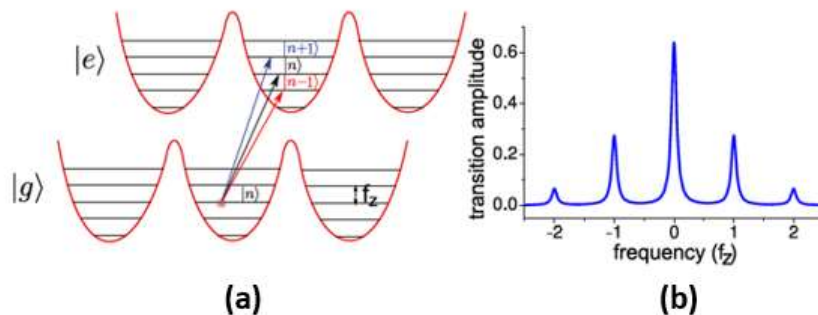
Figure 2.4: (a) Schematic description of the internal energy levels (ground $|g\rangle$ and excited $|e\rangle$ states) and the external energy levels ($|n\rangle$) of a trapped atom in an optical lattice. Black indicates the carrier, which is a pure electronic transition while red is the first red sideband and blue is the first blue sideband. Here, $f_z = \omega_z/2\pi$. (b) Schematic sidebands spectrum, with equal spectral spacings of $n \times f_z$. One can see the carrier unpertubed electronic transition, and the well-resolved sidebands. Taken from[35].

When atoms are strongly trapped in the optical lattice they are distributed among the vibrational levels of the trapping potential. In the sideband cooling technique, a red-detuned light pulse, resonant to the transition $|g,n\rangle \rightarrow |e,n-1\rangle$ is applied. This pulse drives a forbidden motional transition according to the Frank-Condon overlap integral $\langle n|n-1\rangle$[55]. The lifetime of the excited state is very long and this driving field will only induce Rabi oscillations between the two states and will not cool the atoms in the lattice. However, if a second (repumper) laser to pump the atoms from $|e,n-1\rangle$ to a fast decaying state $|e',n-1\rangle$ is applied, a sponteneous decay process $|e',n-1\rangle \rightarrow |g,n-1\rangle$ will follow dominantly without a change of a motional quantum number as first demonstrated by Diedrich et al.[56]. The overall process is $|g,n\rangle \rightarrow |g,n-1\rangle$, hence a loss of vibrational quanta in the ground state and cooling to the zero motional level after susequent cycles.
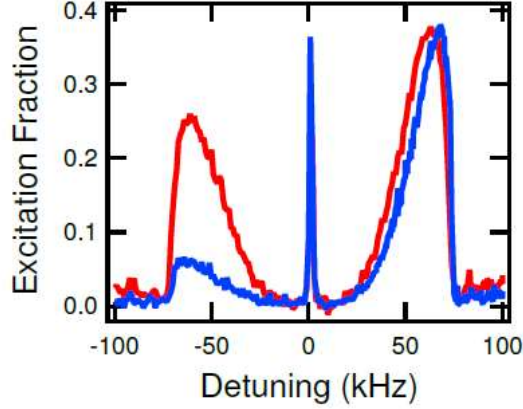
Figure 2.5: Sideband spectra of the trapped atoms with (blue) and without (red) sideband cooling at the same trap depth. A strongly suppressed red sideband is visible in the blue curve. The only difference between the two spectra is that the repumper is activated during sideband cooling. Taken from[57].

Once the atom approaches the ground state, it can no longer be excited by the red sideband, and consequently, the red sideband of the spectrum is significantly suppressed as can be seen in Fig. 2.5, resulting in a reduced atomic temperature in the longitudinal direction to a few μK.

2.3 Spectroscopy Methods

2.3.1 Rabi Spectroscopy

The basis of the atomic clock is a well-defined two-level system driven by an electromagnetic radiation field from a local oscillator. As early as the 1930s, I. I. Rabi explored and described such systems, and provided the physical and mathematical basis for their analysis (Nobel Prize, 1944). Using this theory, the atomic transition frequency of atoms trapped in an optical lattice can be investigated and applied for the calibration of drifts in the local oscillator output frequency.

When an applied radiation field excites a two-level system, the population of the excited level depends on the intensity, the duration τ (to be distinguished from the averaging time used in Eq. 1.2), and detuning of the radiation from the resonance δ, according to the expression[58]

$$P_e(\delta, \tau) = \frac{\Omega^2}{\Omega'^2} sin^2(\frac{\Omega'\tau}{2}), \tag{2.21}$$

where the Rabi frequency Ω is equal to $\frac{\vec{d}\cdot\vec{E}}{\hbar}$ and $\Omega' \equiv \sqrt{\Omega^2 + \delta^2}$ is the generalized Rabi frequency. Here, $\vec{d}$ is the transition dipole moment for the specific transition and $\vec{E}$ is the electric field of the radiation vector. One can see that if $\tau = \frac{\pi}{\Omega}$ (π-pulse), the probability becomes a squared sinc function that is maximized for $\delta = 0$, as shown in Fig. 2.6. The Fourier

limited FWHM of the resulting line-shape central fringe is $\Delta\nu_{Rabi} \propto 1/\tau$, which emphasizes the importance of an extended interrogation time, τ. Longer τ gives narrower spectroscopic lines, but in practice, the linewidth of the probing laser limits the measured transition linewidth and longer interrogation times are not necessarily beneficial[47].
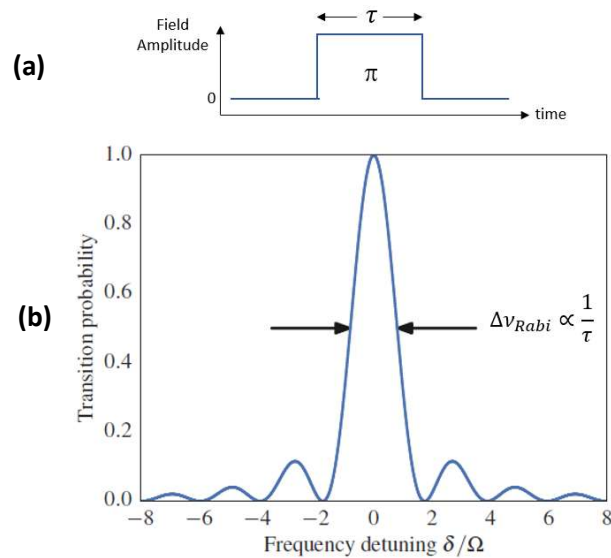
Figure 2.6: (a) A Rabi pulse. (b) Typical Rabi spectrum obtained with a π pulse. Taken from[47].

In this spectroscopic technique, the atoms are excited using a π-pulse of the clock laser (578 nm, Fig. 1.3), while the detection laser (in our case, the 399 nm laser driving a strong transition to collect high fluorescence) counts the ground level population, and the clock laser is tuned by a feedback loop so that the excited state population is maximized, thus keeping $\delta=0$.

2.3.2 Ramsey Spectroscopy

Another spectroscopic method was developed by Rabi's student, N.F. Ramsey, in 1950 (Nobel Prize, 1989). In this technique, the two-level system is irradiated by two exciting $\pi/2$ pulses at a duration of $\tau = \pi/2\Omega$, separated by a free evolution time ('dark time'). If the two-level system is initialized in the ground state (one of the poles of the Bloch sphere, on the z axis), the first $\pi/2$ pulse rotates the Bloch vector by 90 degrees, and brings it into a superposition state (on the equator, or the x-y plane, of the Bloch sphere). During the free evolution time T, the superposition freely evolves without any disturbance of the driving field at a frequency ω_0, which is the frequency between the ground and excited state. After the dark time, the second $\pi/2$ pulse is applied and again rotates the vector by 90 degrees. At the interrogation stage, the measurement collapses the atom into one of the two basis states on the z axis. If we consider an atomic ensemble, the statistics of the excited state population is a measure of the phase accumulated during the dark time, where the excitation probability may be expressed as[59]

$$P_e(\delta, \Omega, \tau, T) = \frac{4\Omega^2}{\Omega'^2} sin^2(\frac{\Omega'\tau}{2}) \left[cos\left(\frac{\Omega'\tau}{2}\right) cos\left(\frac{T\delta}{2}\right) - \frac{\delta}{\Omega'} sin\left(\frac{\Omega'\tau}{2}\right) sin\left(\frac{T\delta}{2}\right) \right]^2, \qquad (2.22)$$

where $\delta = \omega - \omega_0$ and ω is the frequency of the driving oscillator.

A typical Ramsey spectrum is shown in Fig. 2.7, where we can identify a broad envelope (width $\propto 1/\tau$) called a Rabi pedestal, with many fringes. If $T \gg \tau$, then the linewidth of the central fringe is[60] $\Delta \nu_{Ramsey} = 1/2T$ (note the extra factor of 2 relative to the classical uncertainty relation).
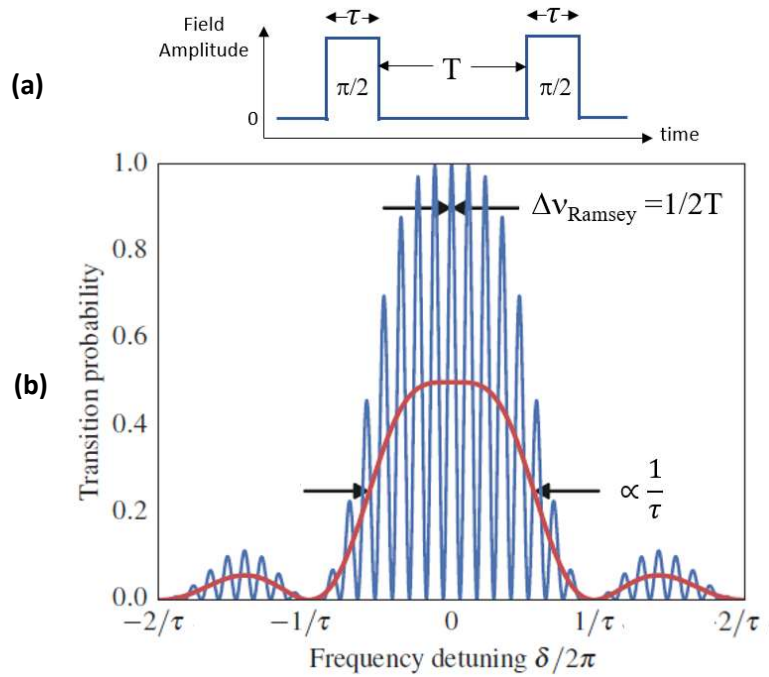
Figure 2.7: (a) Typical Ramsey sequence composed of two $\pi/2$ pulses, separated by a dark time T. (b) The Ramsey envelope with the Rabi signal shape. Taken from[47].

The choice of Ramsey spectroscopy maximizes the line Q factor in comparison to the Rabi method (the achievable resolution with Ramsey excitation is about twice that of Rabi excitation for the same interrogation time[7]). However, although Ramsey spectroscopy gives narrower features at equal spectroscopy times, its use is more complex and causes experimental difficulty in controlling the phase of the probe laser between the two pulses. Therefore, its benefits should be weighed in light of these difficulties[60-62].

3. Clock setup

3.1 General Description

Fig. 3.1 shows a blocks-diagram of the clock systems. Each subsystem (block) will be explained in detail in the following chapters. See also Fig. 1.3 for the energy level diagram.

Figure 3.1: A diagram of the whole clock system. The 1156 nm laser [(1), see Sec. 7.5] used as a local oscillator. It is calibrated by ^{171}Yb atoms (2), stabilized by a 30 cm long high-finesse cavity [(3), Chap. 6] and forms the clock output signal via an optical frequency comb [(4), Chap. 9]. The optical fibers from the laser to the cavity and to the comb are stabilized by a mini-link system [(5), Chap. 10]. The trapping of the Yb atoms takes place in a vacuum system [(6), Sec. 3.2], which includes a 2D MOT chamber [(7), Sec. 3.3] for preliminary cooling and a 3D MOT chamber [(8), Sec. 3.4] for secondary cooling and trapping. The Yb atoms come from two optional sources [(9), Sec. 3.2] – an oven or a dispenser, and are eventually trapped and detected in an optical lattice [(10), Chap. 8]. The cooling, trapping, and detecting processes require several lasers at different wavelengths. All of these lasers are stabilized by a 5 cm long cavity [(11), Chap. 5]. The 798 nm laser [(12), Sec. 7.1] is doubled (13) and used for preliminary cooling (14) and detecting [(15), Chap. 8]. It is also used as a slowing beam for the Zeeman slower and in the transition between the first cell and the second cell (Secs. 3.2 and 3.1, respectively. Not shown in this diagram). The 1112 nm laser [(16), Sec. 7.2] is doubled and used for second stage cooling. The 759 nm laser [(17), Sec 7.3] creates the optical lattice and the 1389 nm laser [(18), Sec. 7.4] is used as a repumper in the spectroscopy process.

The planned experimental sequence is illustrated in Fig. 3.2. The cycle starts with the operation of the blue (399 nm) 2D MOT that is used to load a green (556 nm) 3D MOT at 80-100 ms. The green MOT cools the atoms to a μK temperature range. The optical lattice laser, operating at 759 nm, is activated during the entire clock cycle and the ultracold atoms are now trapped in the lattice potential. This is the start of the resolved sideband cooling stage. A bias field is applied to remove the degeneracy between the I±1/2 Zeeman levels. The clock laser at 578 nm is activated for about 10 ms and is red-detuned to excite one of the two Zeeman states and to

24

drive a Δn=-1 vibrational lattice transition (see Sec. 2.2.2). In this step, we also need the repumper (1389 nm) as the clock states have a long lifetime, and for the cooling process we need a fast cycle time. In the next step, a circularly-polarized green laser is activated to drive the population into a single Zeeman level, in a 'spin polarization' process (see Sec. 7.2). At the end of this stage, all the atoms occupy the lattice ground state. This is the end of the preparation stage, after which spectroscopy may commence. The typical number of trapped atoms ready to be interrogated is a few thousands.

As discussed, the interrogation phase varies depending on the use of either Rabi or Ramsey spectroscopy. For the former, a π-pulse of typically 100-150 ms is applied, resulting in a Fourier limited spectroscopy line of a few Hz. The pulse length can be optimized to match the local oscillator coherence time. When Ramsey interrogation is applied, the usual $\pi/2$-pulse duration is a few ms, separated by a free evolution time of several hundred ms which can result in central fringes narrower than 1 Hz.
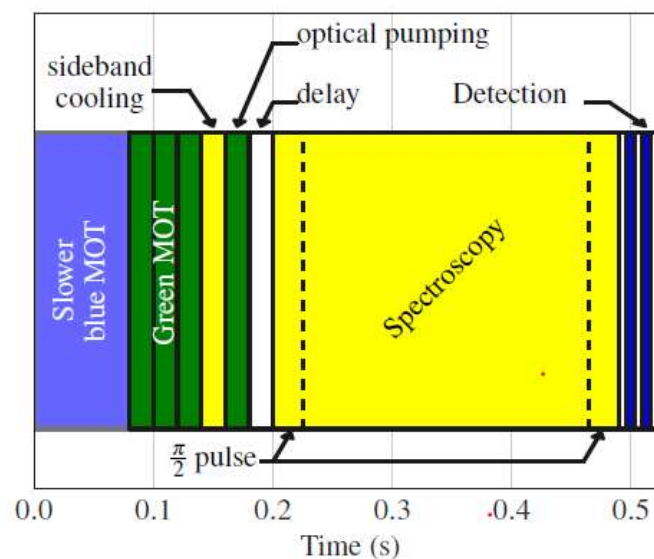

Figure 3.2: A schematic diagram of the clock sequence. In case of Ramsey spectroscopy, the $\pi/2$ pulses are represented with dashed lines. In Rabi spectroscopy the π pulse lasts for the entire spectroscopy time. The total cycle duration is a few hundred ms, depending on the experimental requirements.

For the detection phase, we apply the atomic shelving technique: as the detection operates on the $^1S_0 - {}^1P_1$ transition, the 399 nm beam interacts only with atoms present in the ground state. Three pulses are used, the first pulse measures the atoms that remain in the ground state after spectroscopy (P_g). The second one, since the excited atoms are in the metastable excited state

^{3}P$_0$, detects the background fluorescence caused by scattered light and hot background gas atoms (P_b). To bring the atoms excited during spectroscopy back to the ground state, we utilize the short-lived ^{3}D$_1$ level which has a strong decay channel to ^{1}S$_0$. To this end, we apply a pulse of 10 mW of resonant 1389 nm light for 4 ms which optically pumps the atoms to the ground state with 90% efficiency. Last, a third 399 nm pulse detects these atoms which represent the excited fraction (P_e). The fluorescence from the three 399 nm light pulses is recorded to evaluate the number of atoms in the ground state $|g\rangle$, the background and the exited state $|e\rangle$ respectively (7 ms pulses separated by 6 ms). The fluorescent light is recorded by a photomultiplier tube (PMT) and its output is proportional to the atomic population in the different states (P_g and P_e).

The normalized atomic signal Ψ is calculated as

$$\Psi \equiv \frac{|e\rangle}{|e\rangle + |g\rangle} \approx \frac{P_e - P_b}{P_e + P_g - 2P_b}. \tag{3.1}$$

3.2 Vacuum System

The heart of the clock setup is an ultra-high vacuum (UHV) system designed for the introduction, cooling, trapping, and interrogating of the Ytterbium atoms. It consists of two main cells separated by a differential pumping tube (DPT) as depicted in Fig. 3.3:
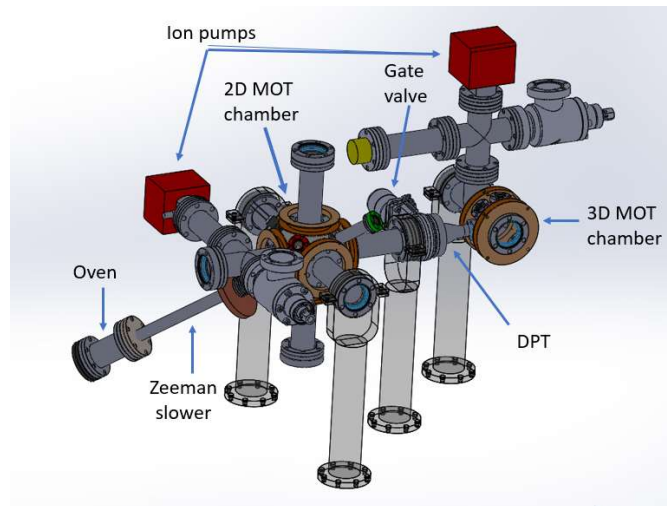

Figure 3.3: General view of the vacuum system.

The 2D MOT chamber is a 316LN stainless steel cube cell by Kimball Physics Inc, designed for the initial stage of cooling by the 399 nm radiation. Inside the cube we fitted two pairs of anti-Helmholtz coils. Hence, four internal coils are fitted inside the cube for achieving gradients of up to 40 G/cm at moderate currents of up to 10 A.

Two natural Yb sources are connected to the cube: the first is an oven + Zeeman slower, and the second is a Yb dispenser. In the 2D MOT chamber the hot atoms from the Yb source, regardless of whether it is the oven or the dispenser, are first cooled in two dimensions. and then directed to the second cell by a push beam[63].

Alternatively, if we use the oven with the Zeeman slower, it is possible to deflect the atoms towards the 3D MOT chamber by using two-sets of moving-molasses to extract a cold beam of ^{171}Yb atoms continuously[64].

The 3D MOT (science chamber) is a 316LN stainless steel CF16 octagon cell by Kimball Physics Inc. Here we plan to apply a 399 nm stop beam in combination with a green (556 nm) laser cooling in a 3D MOT configuration (second stage cooling). This cell has seven AR coated CF16 windows (the 8th window is taken by the DPT) to allow 759 nm for the lattice, 1389 nm for repumping, 399 nm for detection and slowing and, of course, the 578 nm clock laser. It also has two CF40 windows with AR coating in the blue and the green to allow efficient input of the green MOT beams and also efficient blue fluorescence collection. Each vacuum chamber is pumped by a single pump (NexTorr D-200, SAES GETTER). The two chambers are separated by a nipple and a gate valve (VAT, Mini UHV gate valve DN 40). The purpose of the gate valve is to allow maintenance to different parts of the vacuum chamber without breaking the vacuum on the other side. In the nipple we have inserted a DPT made of 316LN stainless steel (Fig. 3.3). This tube is designed to allow the passing of the collimated atomic beam from the 2D MOT chamber to the 3D MOT chamber, while preventing background gasses to cross between the two sides of the vacuum system, and consequently enabling to maintain deep UHV conditions (P<10^{-10} torr) in the region of the optical lattice.
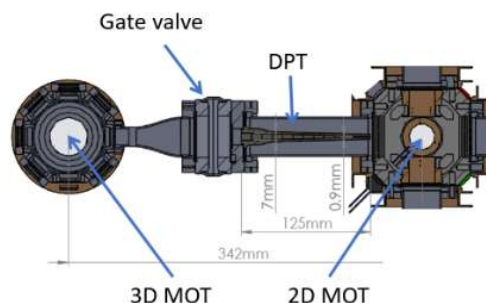

Figure 3.4: A cross section of the differential pumping tube.

3.3 Ytterbium Sources

3.3.1 The Ytterbium Oven

The vapor pressure of Ytterbium is extremely low at room temperature (vapor pressure smaller than 10^{-20} torr at $300\,\text{K}$[65]). Hence, the sample must be heated to above $400°\,\text{C}$ to generate sufficient atomic flux (vapor pressure of about 10^{-3} torr). As noted, in our design, the Ytterbium can be introduced into the vacuum chamber from two different sources - an oven or a dispenser. The purpose of using two optional sources is to examine the "green" 3D MOT loading efficiency with one method compared to the other, in terms of the loading rate, and background pressure. This is also a part of an attempt to optimize the setup in terms of power consumption and miniaturization.

The oven in our system is based on a design by Marco Schioppo for strontium[66], with some modifications that we introduced. The main advantages of this design are the compact dimensions, low energy consumption, and a high flux of a collimated atomic beam towards the 2D MOT region.

The oven cross section is shown in Fig. 3.5. It is made of a cylinder of molybdenum (diameter 14.25 mm, length 20 mm) into which ~3 gr of pure natural Yb (Sigma Aldrich ytterbium, chips, 99.9%) was inserted. The cap of this cell is screwed to allow additional Yb loading if needed (modification to the original design). The center of this cap is drilled and filled with about 100 thin steel capillaries (diameter 4 mm, length 8 mm, by MicroGroup MAT-CUT-HYPO), whose role is to collimate the atomic beam to the center of the 2D MOT chamber. This cylindrical sample compartment is inserted inside an alumina tube (diameter 14.3 mm, length 34 mm), in which a heating tantalum wire is threaded to comprise the oven. The alumina is an electrical insulator (specific resistance $10^{10}\,\Omega\text{cm}$ at $500°\,\text{C}$), but at the same time has a high thermal conductivity ($11\,\text{Wm}^{-1}\text{K}^{-1}$ at $500°\,\text{C}$). It is also suitable for use in UHV. The expansion coefficient of the alumina is just a fraction larger compared to molybdenum, thus insuring good thermal contact up to $500°\,\text{C}$ without the risk of breakage during heating and cooling. The layer around the alumina is a thermal aluminum shield, which functions to stop the radiation from being emitted from the oven.

This entire oven system is held inside a 100 mm long CF40 tube. It is connected to the CF 40 flange by 3 screws and an intermediate MACOR base to avoid heat loss by contact. The power connections to the heater and electrical connections to the temperature sensor are fed through the CF40 flange with electrical feedthroughs.
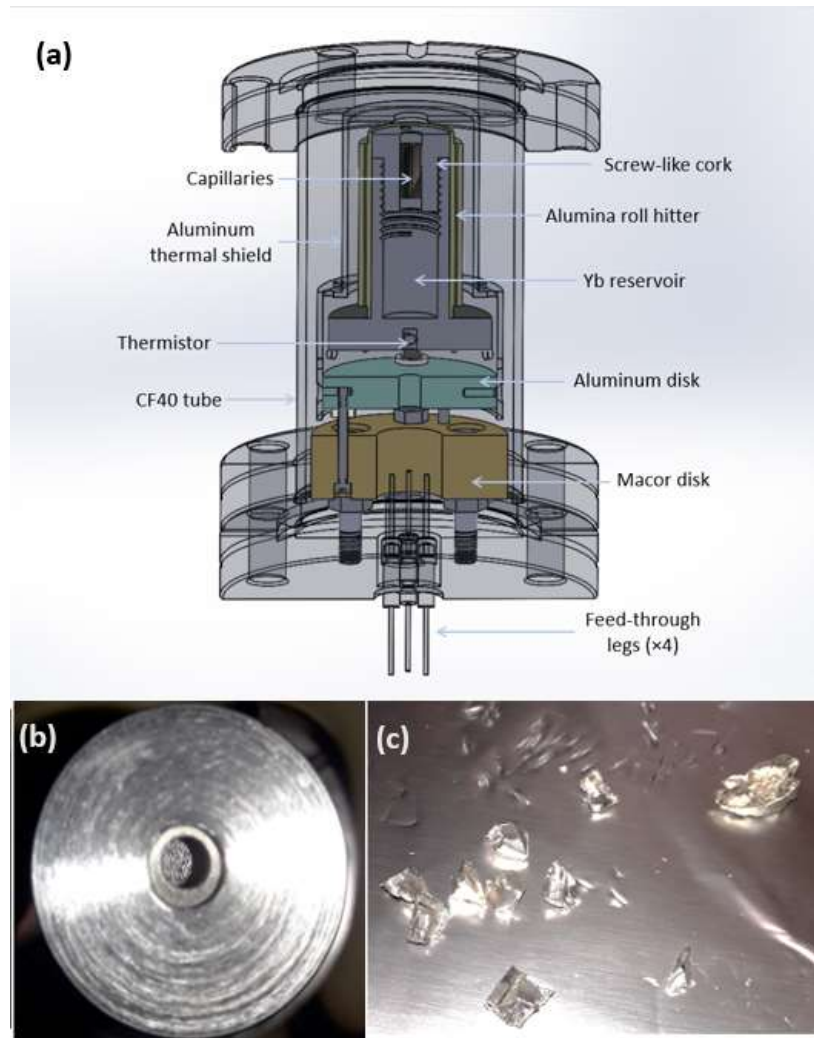
Figure 3.5: (a) The oven cross section. (b) A top view of the oven cap filled with 100 capillaries. (c) Pieces of natural ytterbium, before placing in the oven.

3.3.2 Zeeman Slower

A Zeeman slower is designed to slow down an atomic beam in one dimension. We apply a resonant $399\,\mathrm{nm}$ laser beam opposite the direction of the propagation of the collimated atomic beam emitted through the capillaries in the oven cap. This $399\,\mathrm{nm}$ beam slow the atoms by creating a maximal deceleration of $a_{max} = \hbar k \frac{\Gamma}{2m}$ due to the absorption rate of photons, each having a momentum $\hbar k$ (see Eq. 2.1). The problem in this simplistic description is that the detuning from the resonance changes as a function of the position, because the Doppler shift is reduced as the atoms are slowed during their propagation. The solution to overcome this problem is to continuously compensate for the Doppler shift with a spatial dependent Zeeman shift. This is the purpose of the 'Zeeman slower' tube.

The magnetic field along the atomic beam propagation direction (z-axis), varies to compensate for the position dependent Doppler effect according to Eq. 3.2[64]:

$$\omega_0 + (g_{F'} m_{F'} - g_F m_F) \frac{\mu_B B(z)}{\hbar} = \omega_L + \frac{2\pi v(z)}{\lambda_0}, \tag{3.2}$$

where $\omega_0 = \frac{2\pi}{\lambda_0}$ is the resonance frequency in the rest frame, $g_{F'}$ and g_F are the Landé g-factor of the excited and ground states, respectively, $m_{F'}$ and m_F are the z-components of the total angular momentum of the two levels, $\mu_B = 1.4 \cdot 10^6$ Hz/G is the Bohr magneton, $B(z)$ is the magnetic field along the z-axis in Gauss, ω_L is the laser frequency and $v(z)$ is the velocity of the atoms in the beam.

Accordingly, the magnetic field as a function of the position should be[64,67]

$$B(z) = \frac{1}{(g_{F'} m_{F'} - g_F m_F)} \frac{\hbar}{\mu_B} \left[\Delta + \frac{2\pi v(z)}{\lambda_0} \right], \tag{3.3}$$

where $\Delta = \omega_L - \omega_0$ is the laser detuning from resonance.

Taking the acceleration to be constant, the velocity at any point z will be[64]

$$v(z) = \sqrt{v_i^2 - 2az}, \tag{3.4}$$

where v_i is the initial velocity of the atoms. If we wish the atoms to be brought to a halt after a distance L_0, then $a = \frac{v_i^2}{2L_0}$. Using this relation, Eq. 3.3 becomes

$$B(z) = \frac{1}{(g_{F'} m_{F'} - g_F m_F)} \frac{\hbar}{\mu_B} \left[\Delta + \frac{2\pi v_i}{\lambda_0} \sqrt{1 - \frac{z}{L_0}} \right]. \tag{3.5}$$

In practice, the atomic beam is slowed to a small finite velocity as the Zeeman slower is truncated to a length $L < L_0$. The spatial dependent magnetic field profile for a final velocity v_f corresponding to this shorter length L is given by[64]

$$B(z) = B_1 + B_2 \sqrt{1 - \frac{z}{L}}, \tag{3.6}$$

where the constants B_1 and B_2 are determined by the boundary conditions

$$B(z = 0) = B_1 + B_2 = \frac{\hbar}{(g_{F'} m_{F'} - g_F m_F)\mu_B} \left[\Delta + \frac{2\pi v_i}{\lambda_0} \right], \tag{3.7}$$

$$B(z = L) = B_1 = \frac{\hbar}{(g_{F'}m_{F'} - g_F m_F)\mu_B}\left[\Delta + \frac{2\pi v_f}{\lambda_0}\right].$$

The resulting expression for the magnetic field profile is

$$B(z) = \frac{\hbar}{\left(g_{F'}m_{F'} - g_F m_F\right)\mu_B}\left[\Delta + \frac{2\pi v_f}{\lambda_0}\right] + \frac{\hbar}{\left(g_{F'}m_{F'} - g_F m_F\right)\mu_B}\left[\Delta + \frac{2\pi(v_i - v_f)}{\lambda_0}\right]\sqrt{1 - \frac{z}{L}}. \quad (3.8)$$

Even after the meticulous analysis just presented, there are evidently quite a few free variables that we can choose, such as the final velocity, the length of the slower and the detuning from resonance. In our system, we chose parameters to optimize a compact and low power slower.

In the atomic beam that is emitted from the oven (unlike atomic gas with 3D symmetry), the velocities follow the Maxwell distribution probability in 1D according to[68]

$$p(v) = 2\left(\frac{m}{2k_B T}\right)^2 v^3 e^{-mv^2/2k_B T}, \quad (3.9)$$

where m=2.86·10^{-25} kg is the ^{171}Yb atomic mass, $k_B = 1.38 \cdot 10^{-23}$ JK^{-1} is the Boltzmann constant and T is the oven temperature (about 450^0 C in our case). The most probable velocity in the atomic beam is[66,68]

$$\bar{v} = \sqrt{\frac{3k_B T}{m}} \approx 330\frac{m}{s}. \quad (3.10)$$

The atoms are fast and heavy and therefore the fraction that can be trapped without a slower is very small. The atomic beam needs to be slowed down to a value within the capture range of the trap, a few tens of m/s. The values that we used in the optimization are: 350 m/s for the initial velocity and 30 m/s for the final. In addition, we wanted to reduce the length of the slower as much as possible, without applying very high external magnetic fields that will complicate the coil design and require water cooling of the coils. Note that the length of the slower cannot be too short, also because it must match an acceleration that does not exceed the maximum possible acceleration $a_{max} = \hbar k \frac{\Gamma}{2m} \approx 5 \cdot 10^5 \, m/s^2$ (see Eq. 2.1). In our design, $a = \sqrt{(v_f^2 - v_i^2)/2L} = \sqrt{(350^2 - 30^2)/2 \cdot 0.18} = 3.38 \cdot 10^5 \, m/s^2 \approx 0.63 a_{max}$. For practical reasons, like the requirement for high laser power as well as of high magnetic gradient, we do not work at the maximal acceleration. In the simulation we conducted, we set the slower length to L=18 cm, and the detuning to a value of $\Delta/2\pi$=-400 MHz (red-detuned). In our case,

λ_0=398.911 nm and[67] $(g_{F'}m_{F'} - g_F m_F) \approx 1$. Furthermore, in order to minimize the penetration of an intense magnetic field into the 2D MOT region, we added a 'field-flip Zeeman coil'. Around this coil the magnetic field gradually turns from positive to negative. This configuration is beneficial for two reasons: a) It allows to achieve a higher magnetic gradient at lower currents, and b) the magnetic field gradient drops faster towards the direction of the 2D MOT region. The magnetic profile in our optimal configuration is shown in Fig. 3.6. The values of the magnetic fields in Eq. 3.6 are: B_1= -232 G and B_2= 573 G (or $B_{(z=0)}$=341 G and $B_{(z=L)}$=-232 G).
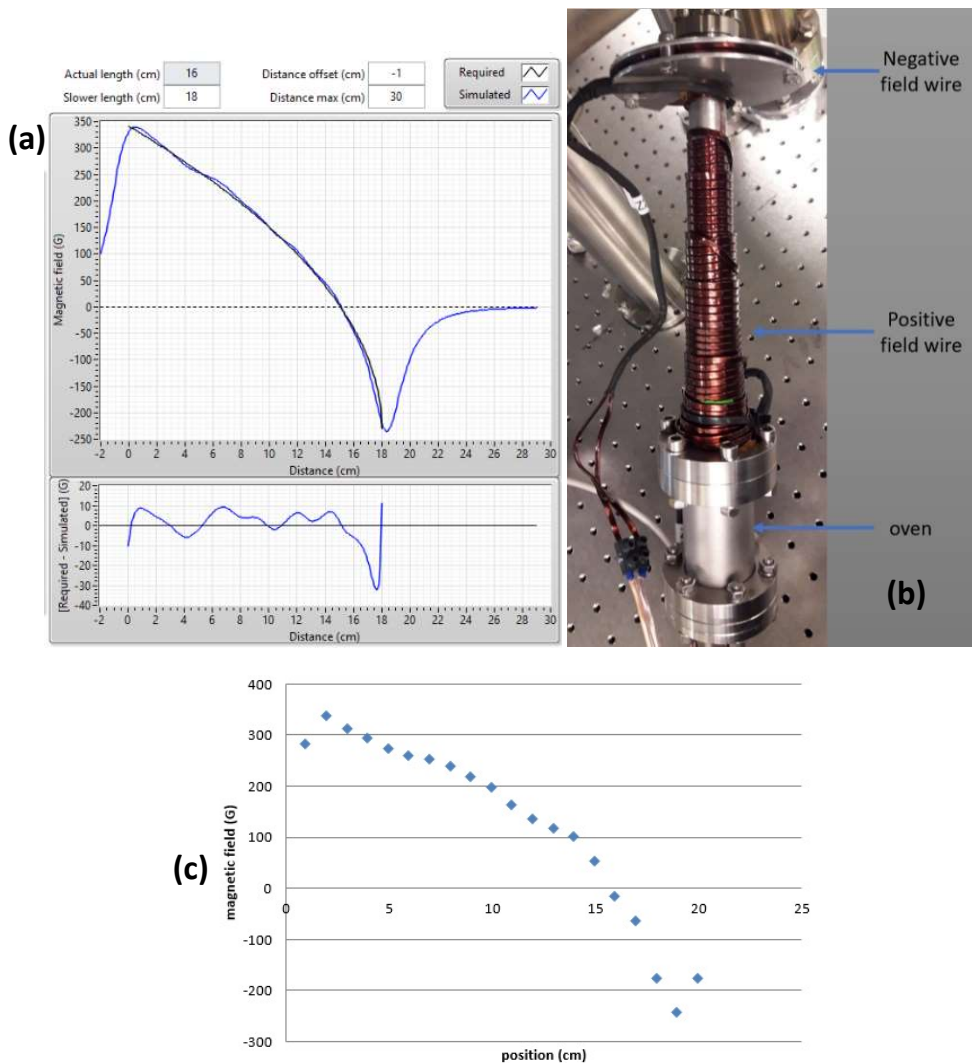

Figure 3.6: (a) A graph of the optimal magnetic-field profile in the middle of the slower tube (black line), and of the simulated field according to the practical design of the wires. The difference between the two curves is plotted below. (b) The oven and slower as connected to the experimental setup. On the slower one can see the positive field coil (bottom of the tube) and the negative field-flip coil (one large coil at the top). (c) We used a (LakeShore 460 3-channel) Gaussmeter to measure the z-component of the magnetic field in the center of the slower tube.

We based the construction of the Zeeman slower on a CF16 tube with outer diameter of 20 mm. The coil is made of an insulated copper wire with a rectangular cross-section of 4 mm·1.25 mm, where in the 'positive' coil the current is 21 A. The total length of the wire in this coil is about 12 m. In the 'negative' coil we run 35 A and the total wire length is 2.9 m. The total electrical power consumption is 30 Watt, so the slower generates significant heat. To evacuate this heat, we designed custom radiators, which are cooled by air flow from a fan.

3.3.3 Dispenser

Based on previous investigations[69] we fitted a dispenser as an alternative Ytterbium source. The dispenser (Alfa-Vakuo Yb 7f) dimensions are 90 mm long, and 7 mm in diameter. It is filled with 5 gr of natural Yb. The dispenser is heated by electric current to $\sim 450^0$ C. In order to further collimate the atomic beam to the center of the cell, we designed a 10 mm long, cone shaped cap, and drilled it (1 mm driller) at an angle towards the center of the 2D MOT. The dispenser is connected to a CF16 electrical feedthrough and is inserted into a CF16 nipple. To avoid shorts, we designed two homemade MACOR discs that are used as spacers.
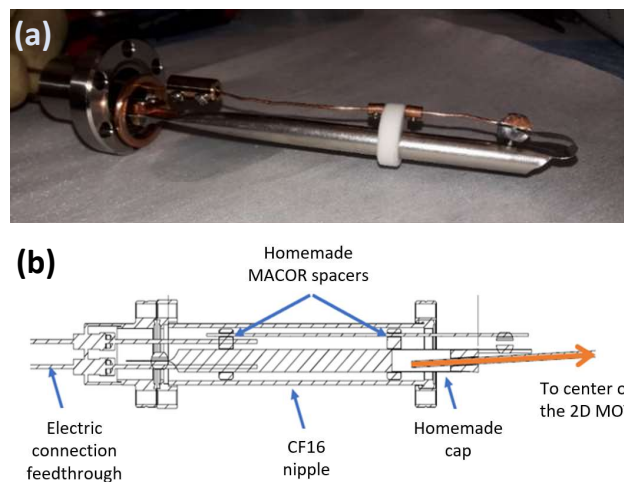

Figure 3.7: (a) The dispenser is ready for connection to the vacuum system. (b) dispenser cross section diagram. In (a) one of the macor spacers is not visibile as it was not placed yet.

3.4 2D MOT

The fact that the two Ytterbium sources are loading an intermediate 2D MOT stage (or moving molasses deflecting beams) is important for two reasons. First, in this way we avoid a "hot spot" which is directly viewed from the direction of the atoms in the lattice and will contribute to high BBR uncertainty. Second, in this way the background pressure in the 3D MOT chamber is lower, thus prolonging the lattice lifetime and avoiding harmful collisions with the background.

The 2D MOT is the first cooling stage in our system. As noted, it takes place in the custom Kimball Physics cube chamber. This is a 316LN stainless steel 3.68'' part, with an internal spherical space of 3.30" in diameter. It has six 2.75" CF ports in the facets, and eight 1.33" CF ports in the corners. To generate a ~40 G/cm magnetic field gradient for the MOT without requiring water cooling, a very compact assembly must be designed. For this reason, we decided to insert the coils into the cell. The two pairs of coil frames (outer diameter 27 mm) were fitted to specially designed threads under the 2.75" CF ports. Care was given to maximize the contact area as much as possible for optimized heat transfer from the coils to the chamber. The coils are made from Kapton insulated Cu wire, D=1.02 mm. In one pair we counted 35 windings while the other had 36.

The axial separation between the centers of each coil pair is 49 mm, and the z-component of the magnetic field (parallel to each pair's axis) that is created in the center of the chamber (for a current of 1 A) is shown in Fig. 3.8. In addition to the inner coils, six external coils were also attached, allowing for fine control of the field gradients at the center of the cell if needed.
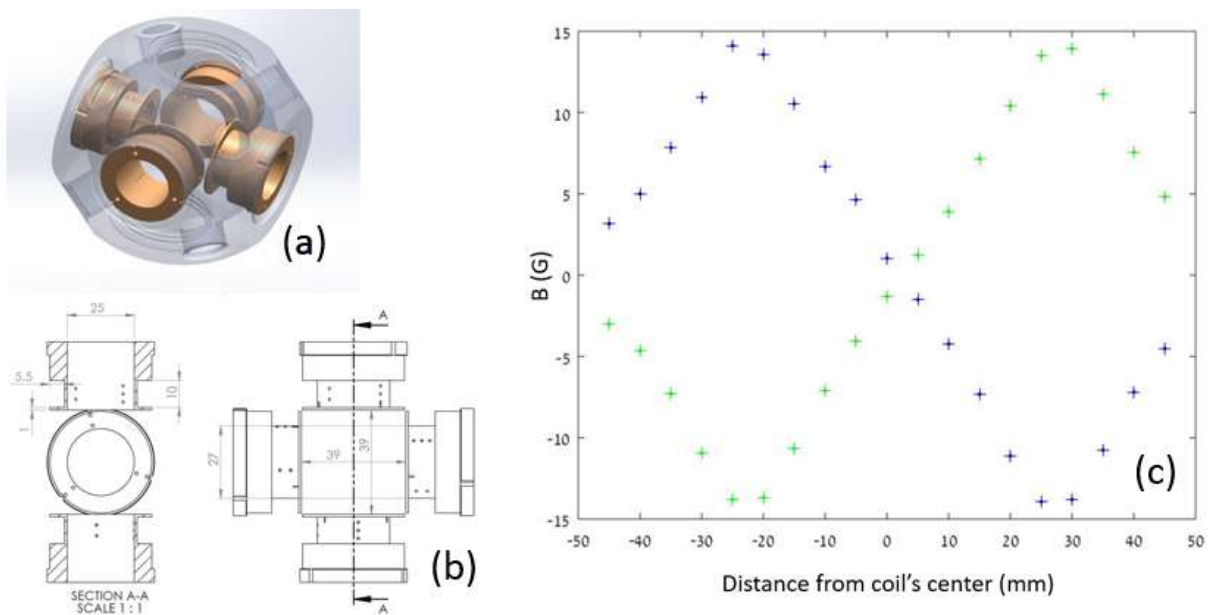
Figure 3.8: (a) A 3D view of the cube chamber. The copper coil frames are connected to threads close to four viewports in the same plane (the wires themselves are not shown). (b) Cross section and dimensions of the coils' frames. (c) The intensity of the magnetic field component parallel to the coil axis at different distances from the center of the cell (for a current of 1 A), created by the X-axis coils (blue crosses) and by the Y-axis coils (green crosses).

Laser light at 399 nm is introduced through four Lesker 2.75" CF viewports (VPZL−SPLXXX − DUV, fused silica laser grade, non−magnetic, AR coating on both sides @ 350−600nm) and the internal coils to complete the 2D MOT scheme. A polarization maintaining optical fiber splitter from OZ OPTICS (FOBS-12P-111-3.5/125-PPP-556-50/50-40-A3AHPCA3AHPCA3AHPC-3-1-HPO.5) delivers the laser light to two collimators that are connected to two CF40 viewports on the two axes of the 2D MOT. These two beams acquire a circular polarization after passing through a λ/4 waveplate and are retro reflected from the other side of the chamber following a double pass through a second λ/4 waveplate to complete the necessary 2D MOT configuration.

One of the additional two 2.75"CF ports in this cube is used to enter a "push" beam, the other (opposite) 2.75"CF port is used to connect the cube to the rest of the vacuum system via a DPT.

Two of the remaining eight 1.33" CF ports are used for the ytterbium sources. One 1.33" CF opposite to the oven is closed by a viewport to enter the Zeeman slowing beam. This viewport is also heated to 400°C to keep ytterbium from sticking to it.

Two more 1.33" CF ports are used for electrical feedthroughs to connect the internal 2D MOT coils. We connected two viewports for monitoring the 2D MOT build-up and the last of the eight ports is simply closed with a blank flange.

It is important to note that all of the abovementioned viewports are not directly attached to the cube. Instead, they are connected to it via a nipple which is connected to the cube. In this way, we avoid any direct line of sight between the ytterbium sources and the windows as shown in Fig. 3.9.
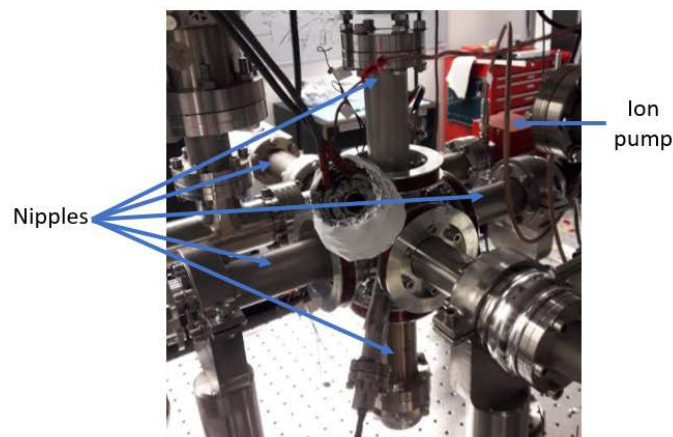

Figure 3.9: Distancing of the windows from ytterbium atoms by CF40 nipples. One can see on the right the NexTorr ion pump (red cube), as described in Fig. 3.3.

3.5 3D MOT

The second stage cooling in our design takes place in the Kimball Physics octagon 3D MOT chamber. It is a 68.4 mm height 316LN stainless steel octagon with a circular internal volume of 152 cc. It includes eight CF16 ports (in one plane), and two CF40 ports (in the other dimension). This is a very narrow (50 mm) chamber, so it is possible to design external quadrupole coils that do not require water cooling and can generate the desired magnetic gradient required for the 3D MOT. This is realized by two parallel anti-Helmholtz coils (inner diameter 80 mm) that are connected to the CF40 ports of the octagon. The separation between the coils' centers is 50 mm, and each one of the coils comprises 20 windings.

All CF40 and CF16 openings (except for the one connected to the DPT) are closed by Kurt-Lesker CF quartz non-magnetic viewports. The two CF40 and four out of the eight CF16 viewports are used for the 556 nm 3D MOT (VPZL−SPLXXX − DUV laser grade, fused silica, non−magnetic, AR coating on both sides @ 350−600 nm). The two vertical view ports are used to insert the 759 nm lattice laser, the 578 nm clock laser and the 1389 nm repumper laser (VPZL−SPLXXX − DUV laser grade, fused silica, non−magnetic, AR coat on both sides @ 550−850nm). The 399 nm slowing beam enters through the viewport, in opposite direction to the 2D MOT push beam (same window as the 3D MOT viewports). A nipple is connected to one of the horizontal CF40 windows, to which the second NexTorr ion pump is connected, as shown in Fig. 3.3. The optical array for inserting all of these laser beams into the octagon cell is complex and requires optimal design. A detailed description of it can be found in Chap. 8.

4. Laser Locking by the Pound-Drever-Hall Technique

The atomic clock involves five different laser systems. Each laser is used for performing a different atomic manipulation and operates on a different transition. However, we use the same frequency stabilization method to "lock" their frequencies and stabilize them for long periods and to overcome various environmental disturbances. For this purpose, we use as a reference a resonance of an isolated, high finesse and high frequency stability cavity.

The resonances of the cavity can be detected by monitoring the transmission or reflection of the input beam from the cavity with a photodetector (PD). However, this signal is always positive and is not ideal to be used as an "error" signal in a servo system. In contrast, the phase of the complex reflection coefficient does change sign around these resonances and is therefore suitable for this purpose. The Pound-Drever-Hall (PDH) technique allows extracting such a phase dependent signal. The PDH setup is presented in Fig. 4.1.
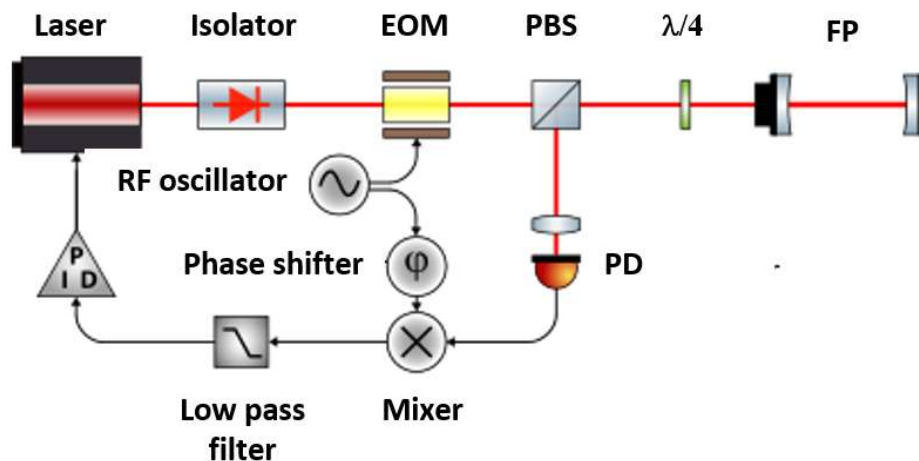

Figure 4.1: General description of the PDH setup: light from the laser is passed via an electro-optical-modulator (EOM) into a FP resonator. The reflected light from the resonator is detected on a PD. The signal from the PD is mixed with the modulation signal and then passed through a low-pass filter. The resulting error signal serves as an input to a PID servo regulator which keeps the laser frequency locked on the FP resonance.

The signal from the PD is proportional to the reflected power hitting it: $P \propto |F(\omega)|^2$, where the reflection coefficient is the ratio between the electric fields of the reflected and the incident fields: $F(\omega) = E_{ref}/E_{inc}$. The intensity of the reflected signal is symmetric and never changes sign as a function of the laser detuning from the cavity resonance, $\delta \nu_L$. It is worth noting that the reflected signal has contributions from light that never entered the cavity and is reflected from the first mirror, and from leakage of light that was inside the cavity and leaked back

through the first mirror. On resonance, the phase difference between these two fields is exactly π and the total reflected beam vanishes[70] (i.e. all the incident light is transmitted into the cavity).

The PD signal does not allow to determine to which "side" of the cavity resonance the laser is tuned. Therefore, attempting to use this signal as an input to a servo system is possible only on the side of the resonance fringe but not on the peak of the fringe.

In contrast to the reflected power from the cavity, both the derivative of the reflected power with respect to δv_L and the phase of $F(\omega)$ (arctan $[\text{Im}(F)/\text{Re}(F)]$) can be used as an error input signal to a servo system. The PDH method [71,72] allows extracting this phase from the reflected signal.

An EOM modulation generates sidebands at frequencies $\omega_L \pm \Omega$, where ω_L is the carrier frequency and Ω is the modulation frequency. The total field reflected off the cavity is the vector sum of the reflected carrier and the two sidebands. The power measured on the PD is thus[72]

$$P_{ref}(\omega_L) = |F(\omega_L)\boldsymbol{E}_{carrier} + [F(\omega_L + \Omega) + F(\omega_L - \Omega)]\boldsymbol{E}_{sideband}|^2 = \qquad (4.1)$$
$$= |F(\omega_L)\boldsymbol{E}_{carrier}|^2 + |\boldsymbol{E}_{sideband}|^2(|F(\omega_L + \Omega)|^2 + |F(\omega_L - \Omega)|^2)$$
$$+2\boldsymbol{E}_{carrier}\boldsymbol{E}_{sideband}\{\text{Re}[\chi(\omega_L)]\cos(\Omega t) + \text{Im}[\chi(\omega_L)]\sin(\Omega t)\} + \mathcal{O}(2\Omega),$$

with $\chi(\omega_L) = F(\omega_L)F^*(\omega_L + \Omega) - F^*(\omega_L)F(\omega_L - \Omega)$.

We are interested in the two terms oscillating at the modulation frequency and resulting from interference of the sidebands with the carrier, because they sample the phase of the reflected carrier.

The PD signal is demodulated by mixing it with a phase-delayed version of the original modulation voltage in a mixer, then passing it via low pass filter to leave only the $\chi(\omega_L)$ term, which is an antisymmetric function of δv_L, perfectly suitable to be used as a correction signal in a servo loop.
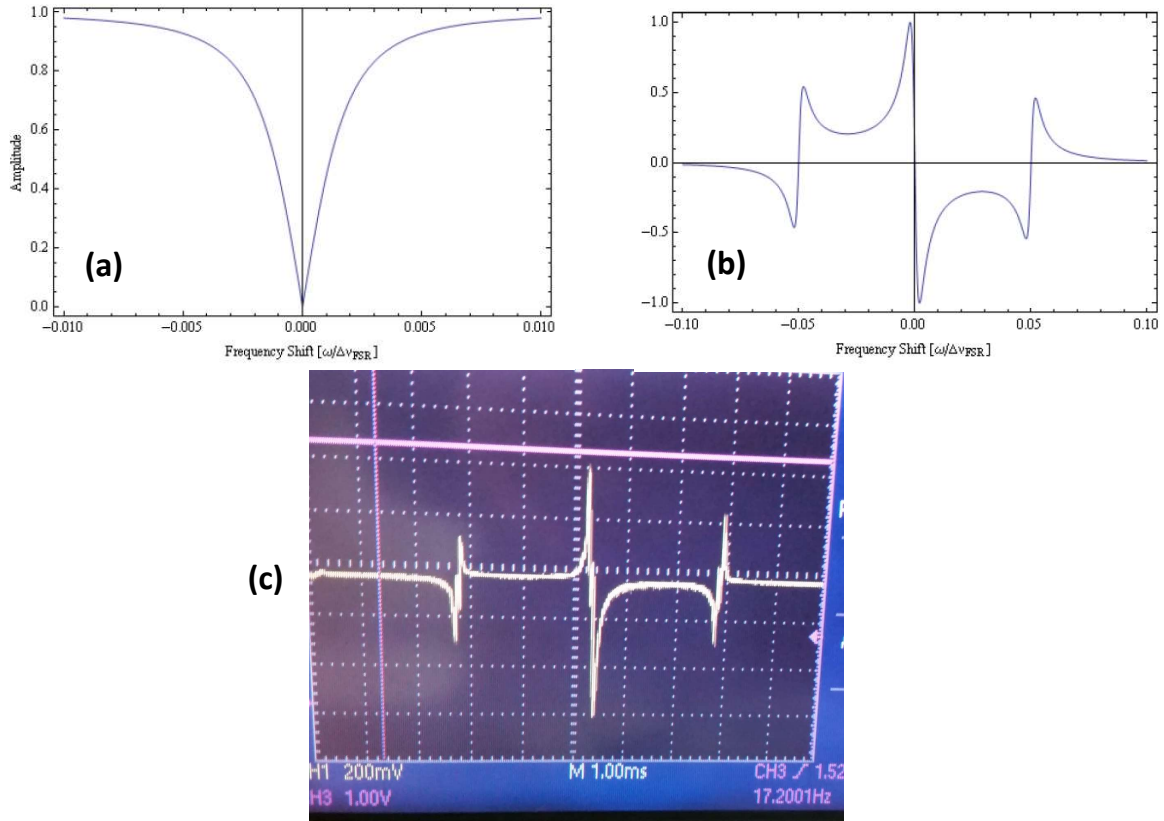
Figure 4.2: (a) A plot of the reflected light as a function of the detuning from resonance. (b) A plot of the expected error signal obtained by the PDH technique. (c) A PDH error signal realized in our setup. One can see the error signals from the carrier and the two sidebands.

It may now be understood how the PDH method can be used to reduce the line width of a free-running laser to a sub-Hz range[73] although the laser is locked to a cavity that has a linewidth $(1/\tau_c)$ which is on the order of several thousands or hundreds of Hz. The free running laser linewidth is limited by phase noise[74,75] which is caused by spontaneous emission of photons into the laser beam. This process causes instantaneous phase and frequency fluctuations that are present on the carrier and the two sidebands.

The leakage beam acts as a stable reference, averaging both the frequency and the phase of the laser over the storage time of the cavity. Any frequency jumps caused by phase noise in the laser will be detected if the instantaneous phase deviates from that of the stable leakage field which is averaged over the storage time of the cavity. The PDH method translates these instantaneous phase changes to voltage which is input to a fast servo system[72]. Thus, what is actually limiting the laser linewidth, is the servo response time and not necessarily the cavity resonance linewidth.

5. Multi-Color Cavity for Laser Locking

Apart from the clock laser, which requires exceptionally high stability and is locked to a 30 cm long cavity with mirror coatings designed for 1156 nm (see Chap. 6), the other four lasers are locked to a 5 cm long Stable Laser Systems FP cavity. It is a hemispherical resonator (ROC_1=0.50 m, $ROC_2 \sim \infty$), which is kept under UHV conditions (P<$2 \cdot 10^{-8}$ torr) and at the zero-crossing temperature of TCE (T=40.00° C). In contrast to the extremely high finesse cavity, which is designed to narrow the linewidth of the clock laser, here the mirrors' coatings are designed to cover several spectral regions and the reflectivity is also lower. One range of the HR coatings on the mirrors is specifically designed for locking the laser at 798 nm, which is used after second harmonic generation (SHG) for first stage cooling. The mirror coating also covers the operation wavelength of the lattice laser at 759 nm. An additional HR coating is also applied on the mirrors to cover the 1112 nm range of the laser which is used for second stage cooling after SHG in a PPLN waveguide. This coating is also designed for high reflectivity at 1139 nm, at which the repumper laser operates. Table 5.1 and Fig. 5.1 show the cavity parameters for the four different laser wavelengths. The mirror coatings also include AR coatings on the external side of the mirrors.

We follow the locking scheme described by Milani et al.[76]. A fraction of the light from each laser (~1 mW) is sent via fiber coupled EOM to the cavity (iXblue Litium Niobate EOM). The EOM is designed to generate sidebands at frequencies <3 GHz [this is the free spectral range (FSR) of the cavity]. These sidebands help to bridge between the resonances of the cavity and the desired frequency of operation. A second RF modulation is also applied on the EOM for the generation of the error signal as in a standard PDH setup. To conclude, the carrier frequency is tuned to the desired transition, and this frequency is not necessary resonant with the cavity modes, therefore a microwave modulation frequency is tuned to generate sidebands, such that one of them coincides with the nearest resonance of the cavity. The sideband is kept locked to the cavity fringe by standard PDH following RF modulation. If this sideband is locked to the cavity, the carrier is also locked.

λ (nm)	Q factor	Calc. Finesse	FSR (GHz)	Reflection (%)	Transmission (%)
759	$4.14 \cdot 10^9$	$3.14 \cdot 10^4$	3	99.99	0.01
798	$1.71 \cdot 10^9$	$1.37 \cdot 10^4$	3	99.977	0.023
1112	$3.53 \cdot 10^9$	$3.93 \cdot 10^4$	3	99.992	0.008
1388	$1.19 \cdot 10^9$	$1.65 \cdot 10^4$	3	99.981	0.019

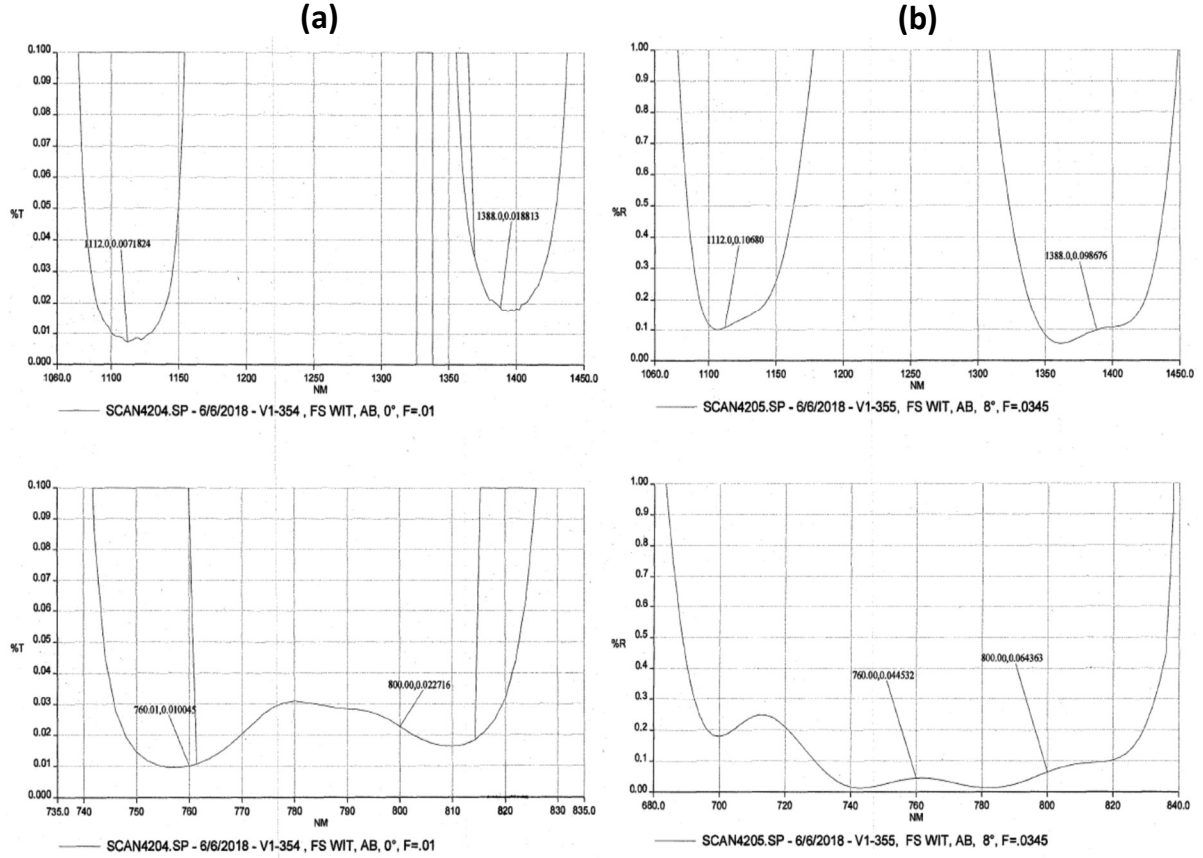Table 5.1: Cavity parameters for the four different laser wavelengths (as measured by the manufacturer).

Figure 5.1: FP resonator high-reflective (HR) coating data (a) and anti-reflective (AR) coating data (b) for all 4 wavelengths (manufacturer data). The AR is on the external sides of the mirrors while the HR is deposited on the internal sides.

The PDH optical arrangement for locking the four lasers on the 5 cm multi-color cavity is shown in Fig. 5.2. This is a compact array placed on a 45 cm×30 cm Thorlabs optical breadboard. We take advantage of the fact that the lattice and first stage cooling (before doubling) lasers operate at close wavelengths (798 nm and 759 nm), and that the repumper and second stage cooling (before doubling) lasers also operate in the same spectral region (1389 nm and 1112 nm), in order to overlap these two laser pairs into two separate optical lines towards the cavity. The reflections from the cavity are detected by fast amplified PDs.
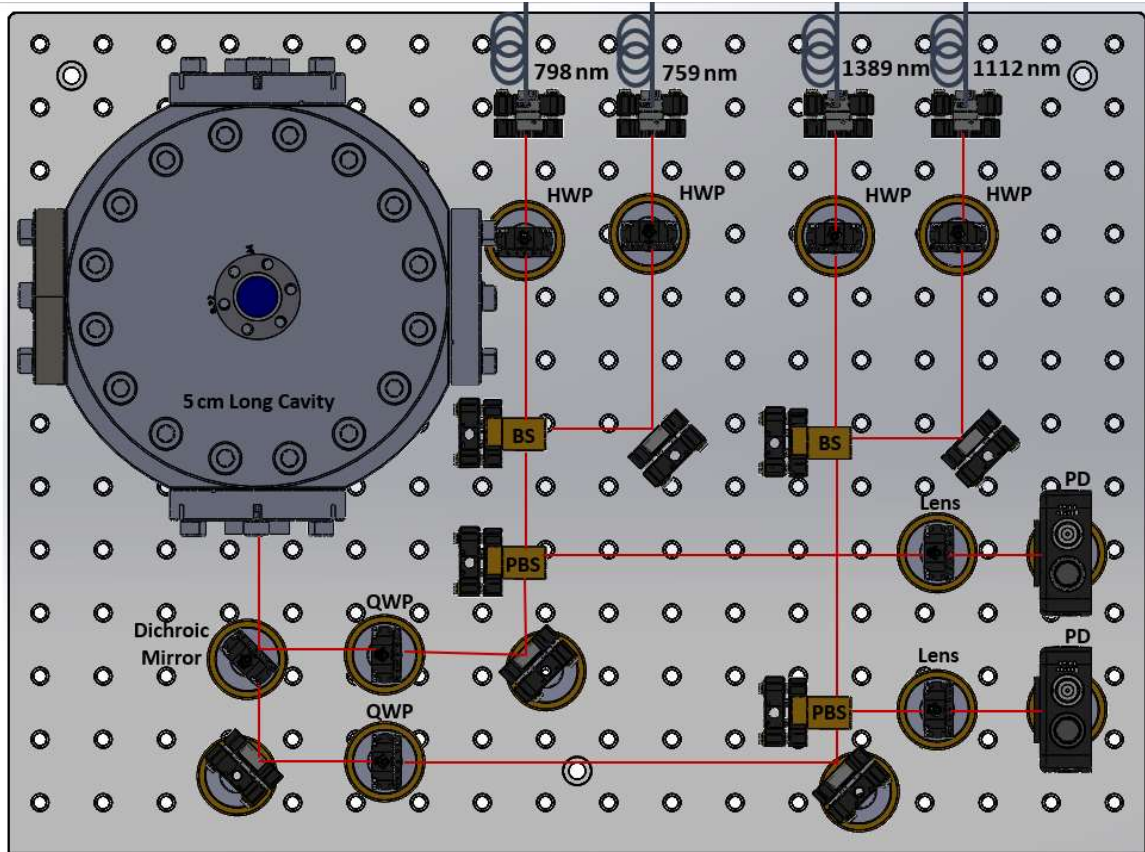
Figure 5.2: The optical layout of the laser locking scheme. All the elements are positioned on a 30 cm×45 cm aluminium breadboard. In this compact PDH array, four laser beams are aligned into a stable 5 cm long FP cavity in two separated lines: one line combines the red (759 nm and 798 nm) beams, and the second line combines the IR (1112 nm and 1389 nm) beams. Linearly polarized light from the polarization maintaining fibers is collimated and propagated via polarizing beam splitters (PBS) and λ/4 waveplates (QWP) into the cavity. The retroreflected light passes via the λ/4 waveplates again and is reflected from the PBS toward a fast PD.

For the fast PDs, we use EOT model ET-2030 (for the red line) and EOT model ET-3000 (for the IR line). Each laser is modulated at a different RF frequency, and then is demodulated separately. For this purpose, we use two Toptica PDD 110 units, and also two home-made circuits. A Labview based PID system was designed for automatic locking. It receives the error signal from each laser and applies a correction for keeping its frequency unchanged.

6. The Clock Reference Cavity

6.1 Ultra-Stable 30 cm Long Cavity

The reference cavity for stabilizing the clock laser in our system is made by Stable Laser Systems. It is a hemispherical FP resonator, with radiuses of curvature and length of $ROC_1=1$ m, $ROC_2 \sim \infty$, L=0.3 m, which is made from ULE and is kept under UHV conditions (P<5·10^{-9} torr). It is maintained at the zero-crossing temperature of TCE (T=32.7° C) by a Stanford Research Systems (SRS) PTC10 temperature controller. The mirrors' coatings were produced by FiveNine Optics. The mirrors' sides facing the outside of the resonator, are coated with an AR dielectric optical coating and the sides facing the inside of the resonator are coated with a HR coating. The measured transmission and the reflectivity (at an angle of incidence of 8°) spectra of the coatings are presented in Fig. 6.1. The estimated finesse can be evaluated by using the transmission value at 1156 nm (T $\approx 5 \cdot 10^{-4}$%) and the relation: $F_c = \frac{\Delta v_{FSR}}{\Delta v_c} = \frac{2\pi}{-\ln(R_1 R_2)}$. Here, Δv_{FSR} is the FSR of the cavity and Δv_c is the Lorentzian linewidth of the resonances. The reflectivity of both mirrors is the same: $R_1 = R_2 = 1 - T = 0.999995$. Under the assumption of no losses, the calculated finesse of this cavity at 1156 nm is thus F_c=628,000. We plan to characterize the optical cavity by direct measurements in the near future.
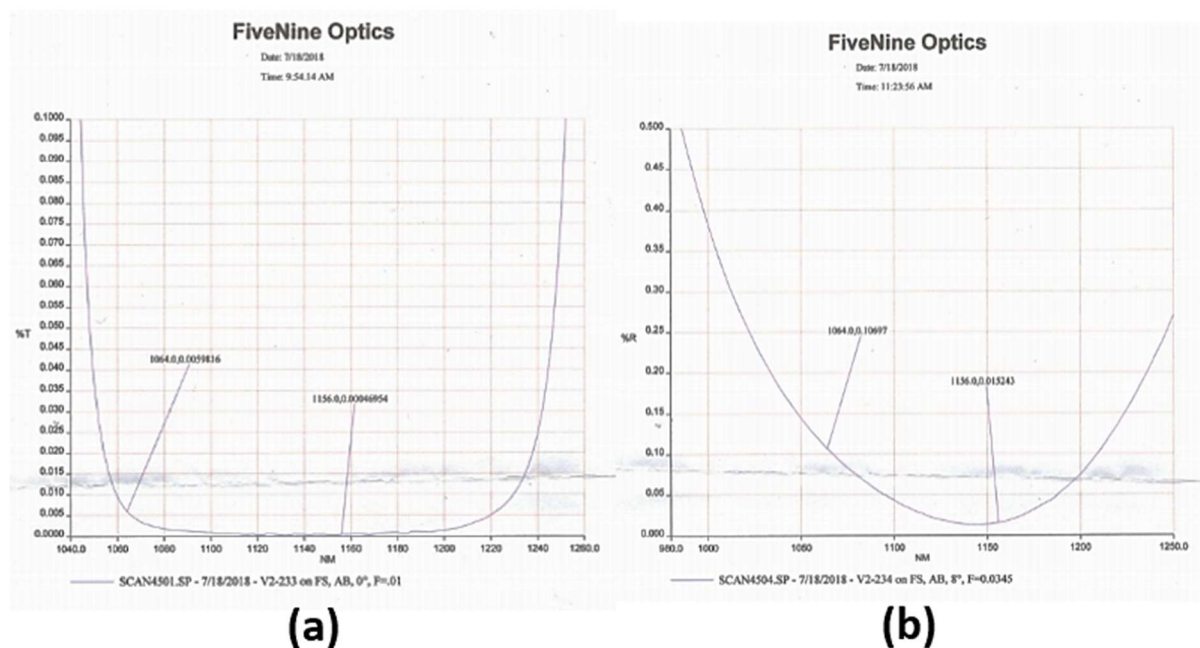

Figure 6.1: (a) HR coating data and (b) AR coating data around 1156 nm (manufacturer data).

The resonator is placed on top of four small plastic supports that rest on a Zerodur base mount. These supports are placed on the Airy points of the cavity. In this way vertical accelerations do not result in length variation of the optical axis of the cavity. This mount is installed inside a Stable Laser System P370 vacuum housing.
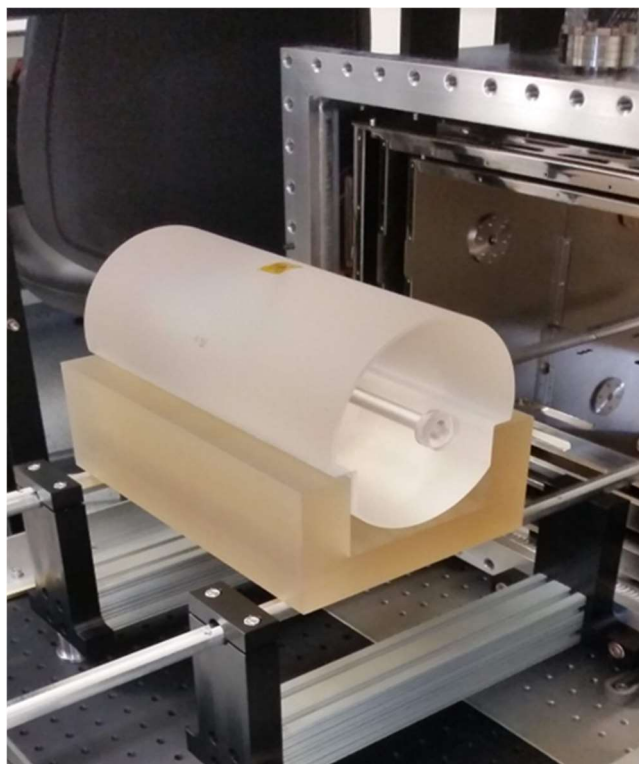

Figure 6.2: The 30 cm long ULE cavity on top of the Zerodur base mount is inserted into the vacuum chamber. The vacuume chamber contains three shielding layers for high temperature stabilization and acoustic noise isolation. Estimated finesse >600,000.

The total weight of this vacuum chamber is 210 kg. The three shielding layers inside the vacuum housing achieve a temperature stability of < 1 mK for low frequency temperature drift in the 5-50° C range.

The vacuum chamber is positioned on a stainless steel breadboard inside a custom acoustic enclosure made by Herzan LTD. The specifications promise >30 dB sound reduction over the acoustic spectrum (we also added an additional isolation layer by the manufacurer and heavy isolation material that is designed for the car industry). We cut an aluminium breadboard and installed it around the vacuum chamber at a convenient height, so that all of the optical components are at the same height as the optical axis of the cavity. In Fig. 6.3 we show the systems that are assembeled on the breadboard.
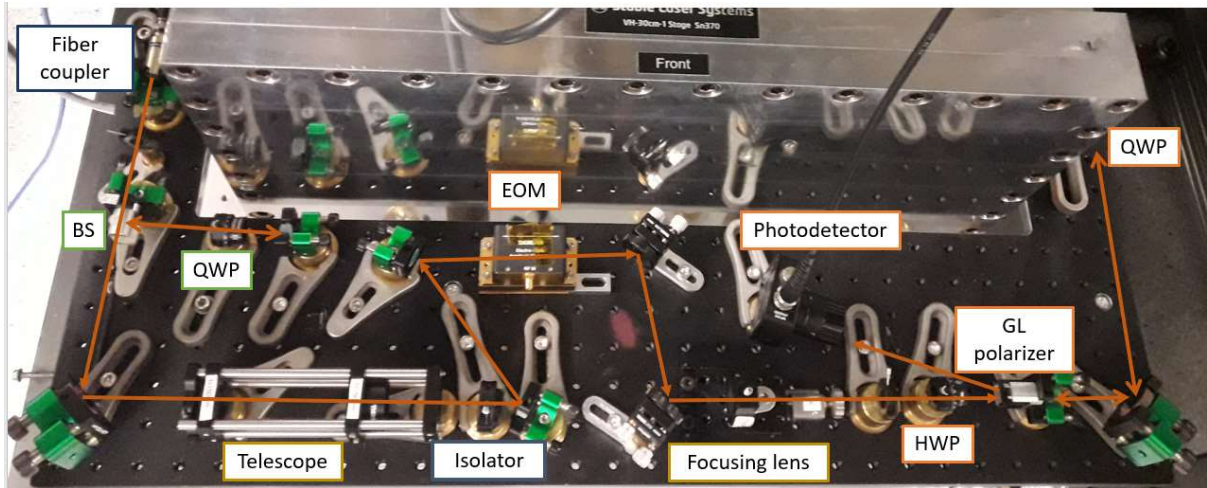
Figure 6.3 The optical systems inside the acoustic enclosure, including: retroreflection into the fiber for phase noise cancelation; a telescope and a focusing lens for mode matching the input beam into the cavity; and the parts for the PDH arrangement.

The optical arrangement must include all the elements for the PDH scheme. We use a free-space EOM (Photonics Technologies, EOM-01-20-IR, AR coated for 1000-1500 nm) for modulation and an IR-sensitive PD (Thorlabs DET-10N2) for detection. The retroreflected signal is directed to the photodiode by reflection from a Glen laser polarizer (GL10-C26). In addition, the optical setup is designed for mode matching the input beam on the fundamental TM_{00} Gaussian mode of the cavity. For proper mode matching we must first calculate the shape of the mode inside the cavity and then propagate it outside. We then overlap the input beam on this outward propagating mode. This overlap is typically performed by use of a telescope which is used to generate a collimated beam with a suitable diameter followed by a focusing lens.

The mode matching simulation is based on the Gaussian beam paraxial approximation method. We are considering here an empty hemispherical cavity, constituting a planar mirror and a spherical concave mirror. The notion of cavity stability relies on geometrical optics. Namely, a cavity is said to be stable if any optical ray remains confined forever in the resonator as it bounces back and forth between the mirrors. In a hemispherical cavity as the one we have, this leads to the stability condition[77]: $0 < L < R_c$ where L is the length of the cavity and R_c is the radius of curvature (ROC) of the curved mirror. In the frame of the paraxial approximation, we look for a complex beam parameter of a Gaussian eigenmode $\tilde{q} = z + iz_R$ that has a waist on the flat mirror. This can be calculated by applying the ABCD matrix method. We can propagate this mode one round trip in the cavity so it will repeat itself without changing, this is shown in Eq. 6.1-6.3 as follows[77]:

$$\tilde{q}' = \frac{(R_c - 2L)\tilde{q} + 2L(R_c - L)}{-2\tilde{q} + R_c - 2L}, \tag{6.1}$$

where $\tilde{q}$ and $\tilde{q}'$ are the initial and the round-trip complex beam parameters respectively. If we require $\tilde{q}' = \tilde{q}$ we get

$$\tilde{q}^2 = -L(R_c - L), \tag{6.2}$$

so $\tilde{q}$ is purely imaginary, and hence

$$z_R = \sqrt{L(R_c - L)}. \tag{6.3}$$

This means that for achieving a stable cavity, the beam mode must have a spescific Rayleigh-range, a specific waist, and hence a specific angle of divergence. For the parameters of our cavity (L=0.3 m, R$_c$=1 m, λ=1156 nm) we get a beam waist (radius) of 0.41 mm on the planar mirror and beam radius of 0.49 mm on the curved mirror. The half angle of divergence is 0.8975 mRadian. In Fig. 6.4 we show a simulation for mode matching by propagation of the TEM$_{00}$ mode out of the cavity using the "GaussianBeam" application.
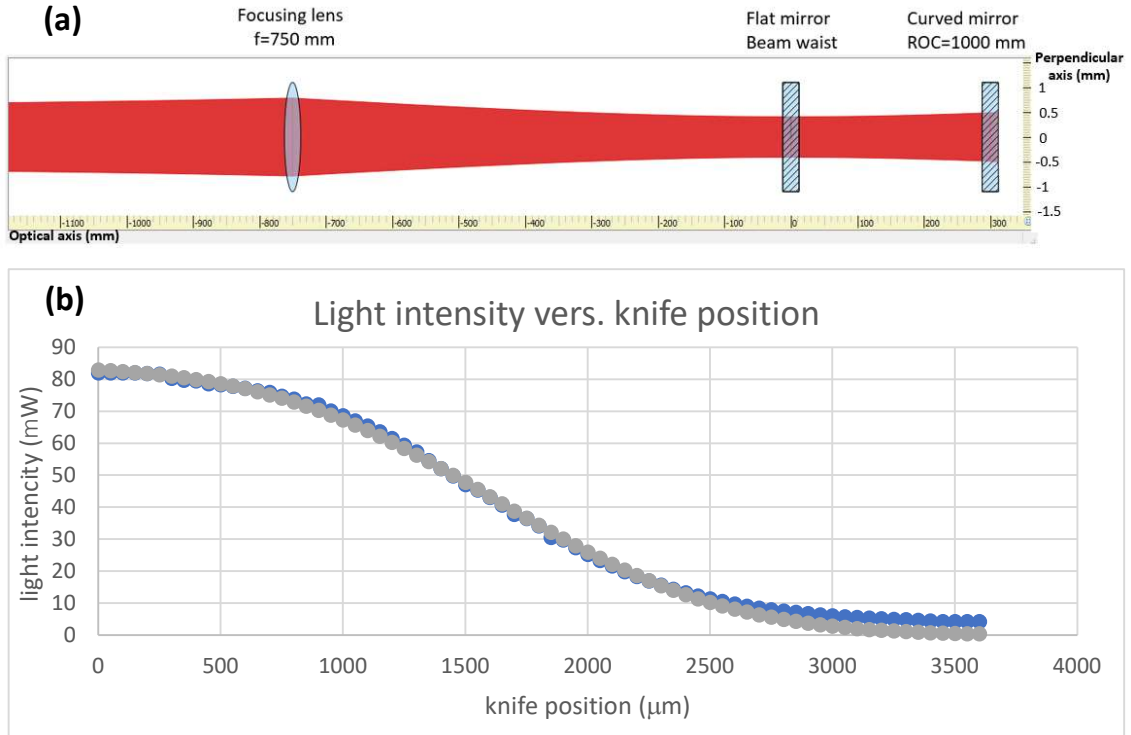
Figure 6.4: (a) Gaussian beam propagation simulation. The fundamental Gaussian mode of the resonator has its waist on the flat mirror, ρ_0=0.41 mm, and a radius of 0.49 mm on the curved mirror. This mode propagates from the flat mirror towards a 750 mm focusing lens and is collimated to a ~1.4 mm diameter beam. We have to input a similar beam in order to achieve good mode-matching. (b) An example of measuring the width of a beam, as we did in our system. This graph describes the measurement of the vertical component of a beam width, by measuring the intensity of light absorbed by a powermeter partially covered by a knife blade at different positions (blue dots) and fitting the resulting curve to the expected complementary error function (erfc) curve (grey dots).

46

We introduce the 1156 nm beam into the acoustic enclosure by an optical fiber (Schafter and Kirchoff, PMC-980-6.4-NA012-3-APC-600-P). The light from the fiber is collimated using a fiber coupler, as presented in Fig. 6.3 (Schafter and Kirchoff, 60FC-4-M18-08). The radius of the beam measured just outside the coupler is about 2 mm, and the beam is almost perfectly collimated over a distance of ~5 m. The mode-matching optical system includes a 3:1 telescope that reduces the beam radius to ~0.7 mm and a focusing lens (f=750 mm, placed 750 mm from the cavity planar mirror) to give the beam the correct angle of divergence and waist.

6.2 Vibration Isolation

The role of the 30 cm long cavity is to maintain the short-term stability of the clock laser, but for that it must be very stable itself. Any geometric changes in the resonator, whether thermal, acoustic, or mechanical (seismic vibrations) cause the cavity resonance frequency to change, and thus increases the spectral linewidth of the laser and harm the Q of the clock. To prevent this, acoustic noise from the air is damped by over 30 dB in the acoustic enclosure. Furthermore, the resonator is thermally isolated from the environment by holding it in a UHV (P<5·10^{-9} torr) chamber, with three layers of thermal isolation surrounding it. The general structure of the isolation may be seen in Fig. 6.5.
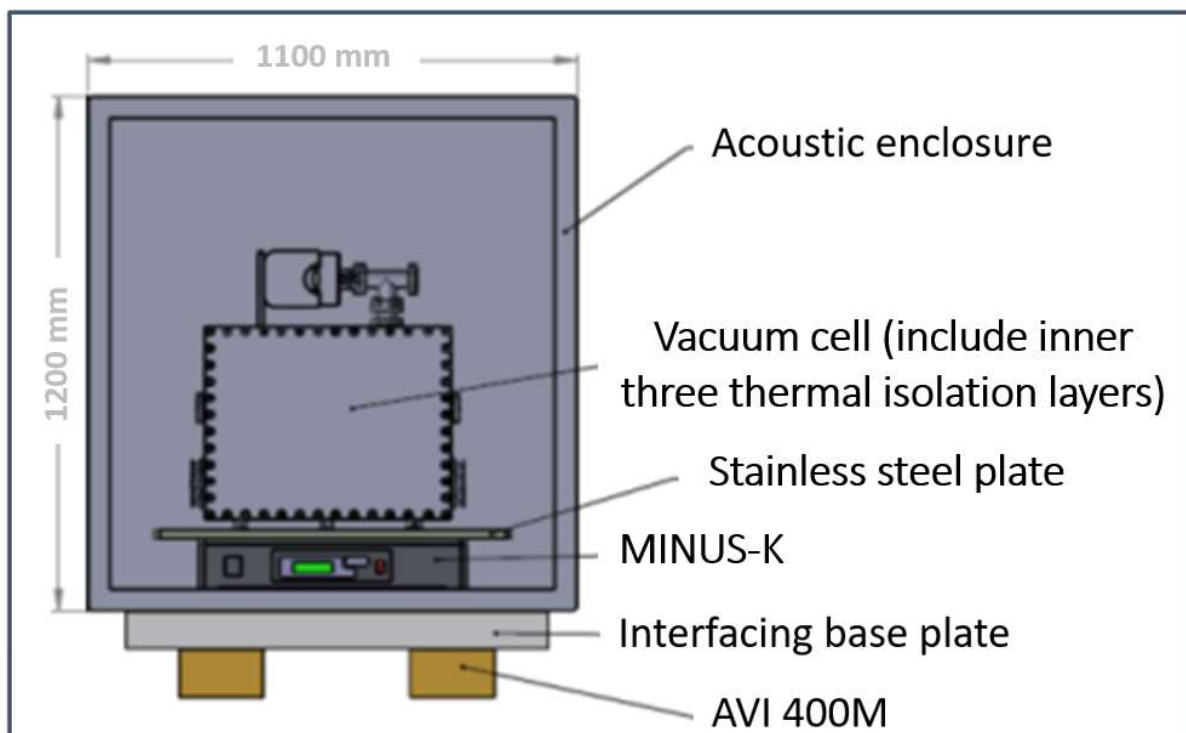

Figure 6.5: The optical cavity inside the isolation systems. We tested two vibration isolation stages inside the acoustic enclosure. The first is an active stage (Herzan ST-300) and the second is passive (MINUS-K, 850-1). We eventually found that the passive MINUS-K 850-1 performs a little better.

In order to prevent vibrations, the cavity is placed on two vibration isolation stages - one passive (MINUS-K 850-1) and one active (Herzan AVI 400M, max. weight 900 kg). The total weight of the cavity and the other elements that are placed on the passive stage is almost 300 kg and the total weight on the active stage is almost 900 kg.

To test the vibration suppression using these stages, we made several measurements with a dummy load of about 300 kg and measured the vibration spectrum using a sensor (Wilcoxon Research 731A Seismic Accelerometer). The preparations for any such measurement were not simple, not only because of the need to lift such a heavy load, but also because of the need to place it exactly on the center of the stage's spring system. In Fig. 6.6, one can see the effectiveness of the two stages in reducing the external vibrational noise. The reduction shown here is similar to the results obtained on similar clock systems[78].
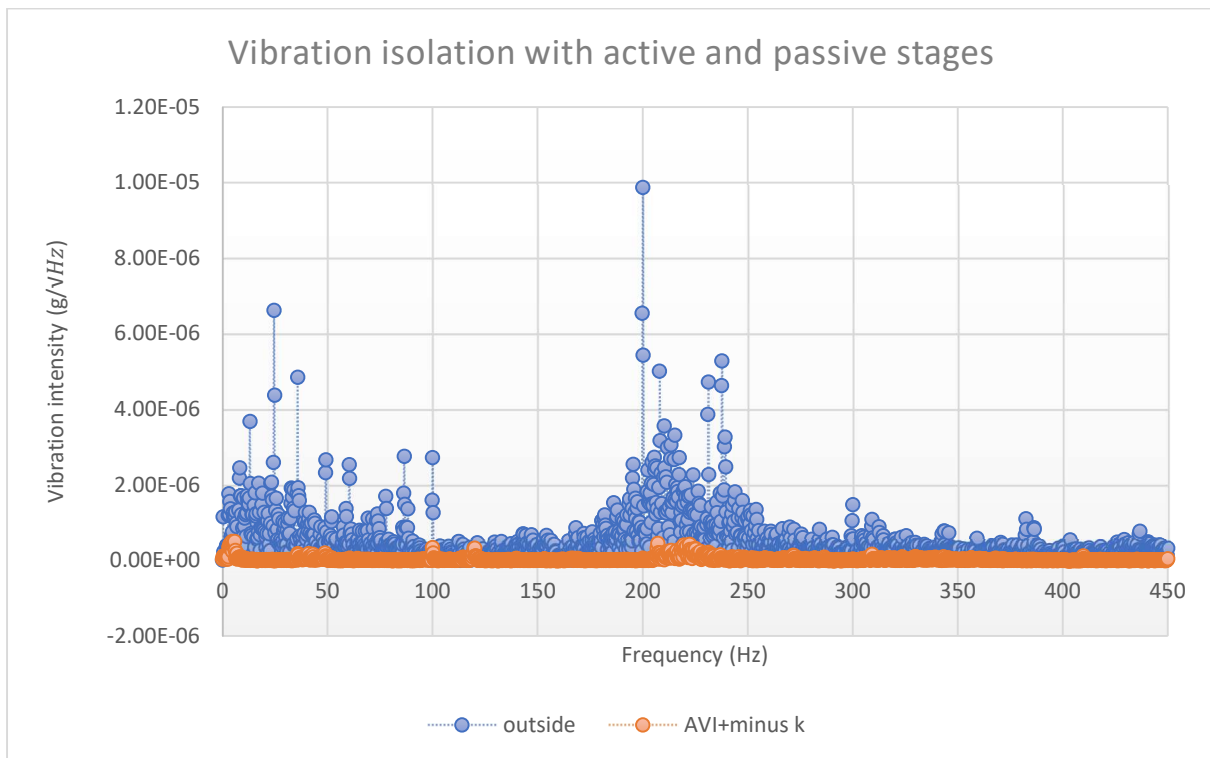

Figure 6.6: Acoustic and mechanical noise spectrum as measured on the lab floor (blue) and on the active stage (orange). At most frequencies, the noise was reduced to the shot-noise of the vibration probe.

7. Lasers

7.1 399 nm Laser System for First Stage Laser Cooling and Detection

In the clock sequence, we use blue laser light (λ=399 nm) to perform several tasks (see Figs. 1.3 and 3.1). It is tuned to the strong $^1S_0 \rightarrow {}^1P_1$ transition and is suitable for slowing down the atomic beam in the Zeeman slower, for fast cooling in the 2D MOT, or optionally for deflection by a moving molasses of the atomic beam towards the science (3D MOT) chamber. We also plan to apply a blue slowing beam in the science chamber in an opposite direction to the atomic beam coming from the direction of the 2D MOT chamber. In addition to cooling, we also utilize this strong transition to scatter many photons in the detection stage of the clock cycle. This is necessary for counting the number of atoms that are in the ground state.

It is estimated that we will need a power of several hundred milli-Watts in total for all the above operations. Such strong diodes are not available at 399 nm in the market, so the other option is to double 798 nm laser light in a nonlinear crystal. The efficiency of single pass second harmonic generation (SHG) in bulk is not so high. Therefore, it is often performed in a resonator.

The source for the 798 nm beam is a tapered amplified external cavity diode laser by Toptica Photonics (DLC-Pro). This laser outputs ~1800 mW in a single mode fiber.

Toptica also produces a SHG in a bow-tie cavity resonator configuration (model DLC TA-SHG Pro), but as the price was too high, we decided to build this setup in-house, based on a publication from INRIM[79], which we modified and is presented in Fig. 7.1.

The frequency-doubling process is done using a Raicol lithium triborate (LBO) crystal placed in the middle between two concave mirrors and mounted on a OptoSigma mirror holder (BSHL-12.7-TF/15-TF) for fine adjustment. The LBO crystal is hydroscopic, and must be protected from moisture, and therefore the bow-tie cavity is completely sealed and is filled with dry nitrogen gas. In addition, a regulated heater keeps the crystal hot in comparison to the environment.
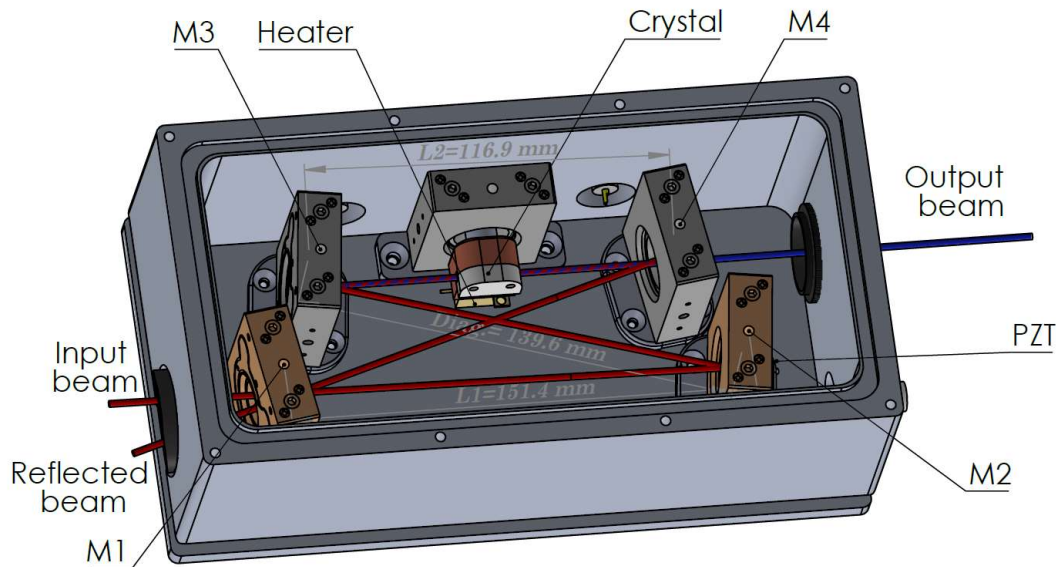
Figure 7.1: Bow-tie cavity design for SHG (total length = 547.5 mm, $FSR_{798\,nm}$ = 548 MHz). This cavity contains two planar mirrors placed L1=151.4 mm apart, and two concave mirrors (ROC3=ROC4=100 mm) separated by L2=116.9 mm with the LBO crystal in the middle between them. The diagonal length is 139.6 mm. The M2 planar mirror is mounted on a PZT, for cavity stabilization by controlling the cavity length. The stabilization process is by means of a feedback signal on the piezo, according to the Hänsch-Couillaud technique.

The bow-tie cavity includes four mirrors, by OptoSigma: the entering mirror, M1, is a planar mirror with a dielectric beam-splitter coating at 798 nm and a dielectric AR coating on its rear surface. For this mirror, T (transmission coefficient) is 1.2% and R (reflection coefficient) is 98.8%, so a fraction of the light can enter the cavity; A second planar mirror, M2, which is placed on a PZT mount, has a dielectric coating at 798 nm with R>99.9%; The first concave mirror, M3, has a dielectric coating at 798 nm on its curved side (ROC=100 mm, and R>99.9%); The output concave mirror, M4 (ROC=100 mm), has a dichroic coating on its concave surface ($R_{798\,nm}$> 99.9%, $T_{399\,nm}$> 95%) and a dielectric AR coating on its rear surface. All four mirrors are intended for CW laser light at the range of 1-3 W and are mounted by OptoSigma mirror holders (BSHL-12.7-TF/15-TF).

The cavity length is stabilized by applying a correction signal on the PZT which holds the M2 mirror. This signal is produced according to the Hänsch-Couillaud cavity locking method[80], which allows to generate an error signal by measuring the polarization rotation of the light reflected from the cavity using a polarimeter (see Fig. 7.2).

To optimize the bow-tie cavity gain, it is important to place the beam center in the middle of the crystal, and to match its waist to the LBO parameters according to the Boyd-Kleinman factor[81]. In our case [crystal length is 15 mm, the ordinary index of refraction at 798 nm (equal to the extraordinary index of refraction at 399 nm) is 1.611], the calculated optimal waist radius is 36 μm.

In practice, we applied the paraxial beam approximation (see Chap. 6) and propagated the beam on a round-trip in the cavity using the ABCD matrix method[79]. With the given cavity dimentions and curvature radius of the mirrors, we calculated the beam waist radius at the position of the crystal to be ρ_0=42 μm. The slight deviation of the beam waist from the optimum is not crucial, since the SHG efficiency does not strongly depend on this parameter around the optimal value[81]. Like in the clock reference cavity case, for proper mode-matching, we propagate this mode outside of the cavity through mirror M1 and overlap it with the input beam.
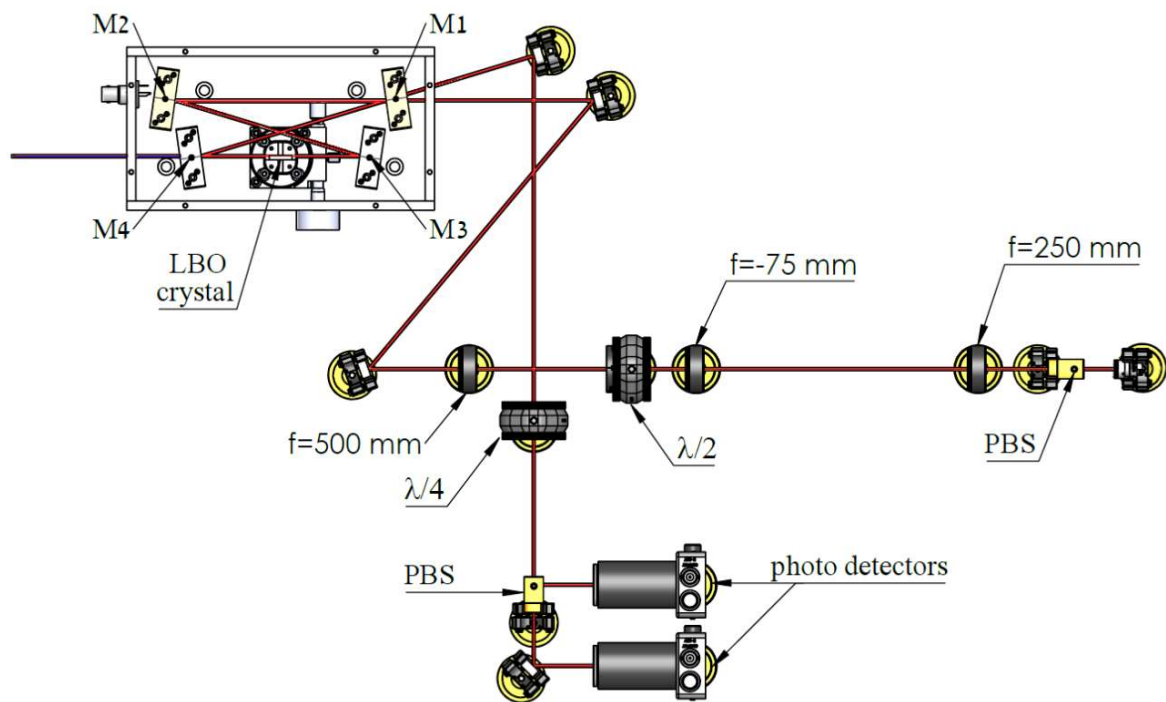
Figure 7.2: SHG in a bow-tie cavity with an LBO crystal, including a Hänsch- Couillaud cavity locking polarimeter that comprises a λ/4 waveplate, a polarizing beam splitter, two PDs, and a differential amplifier (not shown). Also shown in the input beam mode-matching optical setup.

The 798 nm input beam is emitted from a Schafter and Kirchoff collimator (60FC-4-A18-02). The beam diameter is ~3.2 mm. The input mode-matching process is achived by means of a 10:3 telescope (f₁=250 mm, f₂= -75 mm) and a focusing lens (f=500 mm) which is located one

focal length apart from the middle between the two planar mirrors (see Fig. 7.2). In a bow-tie cavity the eigen modes exhibit a second waist in this position[79,82,83], which we calculated to be 226 μm on the horizontal axis and 247 μm on the vertical axis, due to the astigmatism caused by the reflections from the curved mirrors (in perfect accord with[79]). The measured input vertical beam waist at this position is 257 μm, indicating a good overlap.

The expected SHG effeciency from this type of cavity[79] is >80% and we can expect to have over 1 W of light at 399 nm which is sufficient for our setup.

7.2 The 556 nm Green Laser for Second Stage Cooling and Spin Polarization

The $^1S_0 \rightarrow ^3P_1$ transition at 556 nm is used in the clock system for two purposes (see Figs. 1.3 and 3.1). First, it is applied for second stage cooling in the 3D MOT which is loaded with pre-cooled atoms that are launched towards it from the 2D MOT chamber. The expected velocity of such a pre-cooled atomic beam is on the order of tens of m/s and the Doppler limit of the pre-cooled atoms is about 700 μK (see Eq. 2.7). Applying this additional cooling stage on a narrow transition allows further cooling down to a few μK.

The second use of the 556 nm light is spin polarization and it takes place after the atoms are loaded in the optical lattice. As the lattice differential light shift (~100 Hz) of the $^1S_0$-$^3P_1$ transition, is smaller than the 556 nm laser light linewidth of 200 kHz, and smaller than the transition width of 182 kHz, the same laser can still be operated while the atoms are trapped in the lattice. The $^1S_0$ ground state is split to the $m_F = \pm 1/2$ spin states which are probed during the clock cycle (see Fig 1.3). The probing process starts by preparing the atoms in one of these two states. This process is performed by optical pumping and is often called "spin polarization". A bias vertical magnetic field is generated using the Z-axis compensation coils driven by a custom-made power supply controlled by a PC. The bias magnetic field is set to about 0.4 mT to split between the Zeeman sublevels, and the light intensity to about 5 μW. The light frequency and correct circular polarization are chosen to drive one of the two $\Delta m_F = \pm 1$ transitions. However, the spontaneous decay from the $^3P_1$ excited state back to the $^1S_0$ ground state occurs favourably by $\Delta m_F = 0$ transitions. Following 1 ms of optical pumping, ~98% of the atoms are expected to end in the desired opposite m_F state. Since the bias field is aligned along the Z-axis, also the green spin polarization beam has to be along Z (see Fig. 8.1).

The 556 nm beam is generated by SHG in a fiber-coupled PPLN waveguide (HCP Mixer SC19139-01-01). The fundamental 1111.6 nm beam is generated by a Keopsys CW fiber laser (CYFL-KILO-02-LP) which emits about 2 W. The output beam of the laser is reduced and

collimated by a telescope (f_1= 750 mm, f_2= 500 mm), and then is separated by a glass window into two beams: a fraction of the light is injected into the fiber for laser stabilization by the multi-color cavity, while most of the power is transmitted and injected into the PPLN waveguide. The damage threshold of the waveguide is 2000 mW, so care is taken not to exceed this limit. The waveguide temperature is stabilized at 64.4° C for perfect phase matching. The light from the PPLN enters a double-pass AOM scheme for frequency and intensity control. This beam is divided to two branches: most of it is used for the 3D MOT, while only a few μW are needed for spin polarization. Mechanical optical shutters are installed before the light is injected into polarization maintaining fibers for total blocking of residual light scattering from the AOM.

The green MOT is made of three retro-reflecting beams (see Fig. 8.1). Hence, we further split the MOT branch to two beams by a ratio of 1:2. The strong beam is injected via a coupler (OZ Optics HPUC-2A3AHP-556-P-6.2AS-1) to a 50:50 fiber optic beam splitter (OZ Optics FOBS-12P-111-3.5/125-PPP-556-50/50-40-), which delivers the light to two axes of the MOT, while the weaker beam is injected into a fiber which delivers light to the third axis (see Fig. 7.3).
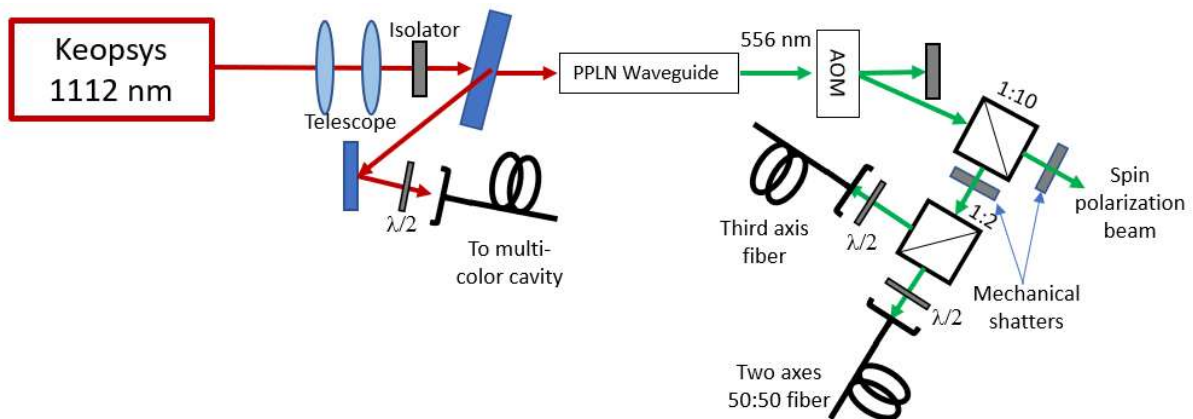
Figure 7.3: Schematic optical array for creating and propagation of the green beam.

7.3 759 nm Optical Lattice Laser

The optical lattice, which is used for trapping the atoms, operates at the magic wavelength of 759 nm (see Sec. 2.2). The laser linewidth at this frequency must be as small as possible and for this we use a Coherent MBR110 Ti:Sapphire laser. This is a wide-spectrum and high intensity laser in the range of roughly 600-1100 nm. The lasing medium is Ti^{3+} ions, embedded in a sapphire crystal which is pumped by a Coherent VERDI 10 $Nd:YVO_4$ laser at 532 nm (maximal output power 18 W, held at 18.5° C by a water radiator).

The light emitted from the MBR110 laser is propagated in free space to the science chamber to create the optical lattice potential. The laser frequency is locked to the multi-color cavity by the PDH technique as described in Chap. 5. Alternatively, it can also be locked to the frequency comb. Although the linewidth of the MBR laser is very narrow ($<$ 75 kHz), the output also includes a broad pedestal of amplified spontaneous emission (ASE). This background radiation is filtered out using a narrow bandpass (FWHM $<$ 0.005 nm) Bragg filter (Optigrate BragGrate Reflective Bragg Grating F2T SPC-759, design wavelength: 759.678 nm in air at $22°$C).

The maximum output power of the MBR is $>$ 2.5 W. This high power is necessary for the evaluation of hyperpolarizability terms which do not cancel at the magic frequency and contribute to the Stark shift[57]. During the operation of the lattice, it is crucial to keep the intensity stable. This is achieved by means of a control loop that operates on the amplitude of an AOM as described in Fig. 7.4. The optics setup for the creation of the optical lattice is shown in Fig. 8.1.
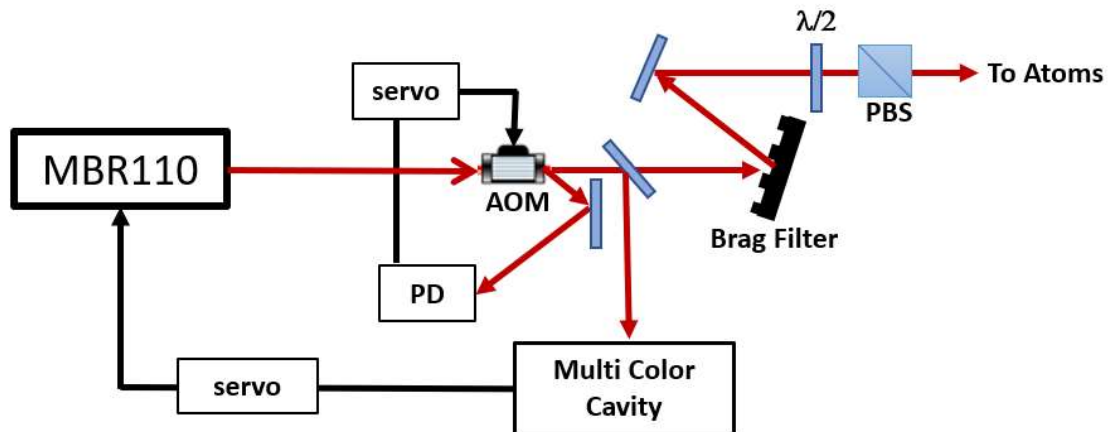
Figure 7.4: Optical layout for power and frequency stabilization, as well as frequency filtering of the 759 nm lattice beam.

7.4 The 1389 nm Repumper Laser

The repumper laser is applied at the end of the cycle during the detection stage (see Sec. 3.1). Normalized counting of the fraction of atoms in each of the two clock states ($^1S_0$ and $^3P_0$) is more reliable than counting the atoms only in one state and relying on the assumption that the total number from one cycle to another is stable. Therefore, a detection scheme is derived for this purpose and it involves the following steps (see Fig. 1.3):

1. After the Rabi/Ramsey interrogation, the atomic population is distributed between the two clock states.

2. A 399 nm pulse excites the atoms in the $^1S_0$ state using the strong $^1S_0 \rightarrow {}^1P_1$ transition, hence producing a strong fluorescent signal proportional to the number of atoms in this state which is ideal for detection. Each atom can scatter many photons before it heats up and is lost from the lattice.

3. At this stage we can start investigating the number of atoms remaining in the long-lived $^3P_0$ state remaining in the lattice (the typical lifetime of the atoms in the lattice is about $3\,s$[84]).

4. A repumper laser pulse of a few mW is applied for a duration of $\sim 5\,ms$. This pulse will pump the atoms out of the $^3P_0$ state to the $^3D_1$ state very efficiently. The Rabi frequency of the $^3P_0$-$^3D_1$ transition is about $70\,kHz$, so hundreds of Rabi cycles occur during this period. We note that the laser does not excite the $^3D_2$ and $^3D_3$ as they are separated by THz frequencies.

5. The atoms in the $^3D_1$ state decay very fast to the $^1S_0$ ground level through the $^3P_1$ state (see Fig. 1.3) with a lifetime of $100\,ns$[85], and then to the $^1S_0$ with a lifetime of $875\,ns$[85]. Next, step number 2 is applied again. This time the measured fluorescence is proportional to the number of atoms which were in the $^3P_0$ state.

By knowing the total number of atoms in each cycle we can obtain a normalized reading independent of atom number fluctuations from cycle to cycle (see Eq. 3.1).
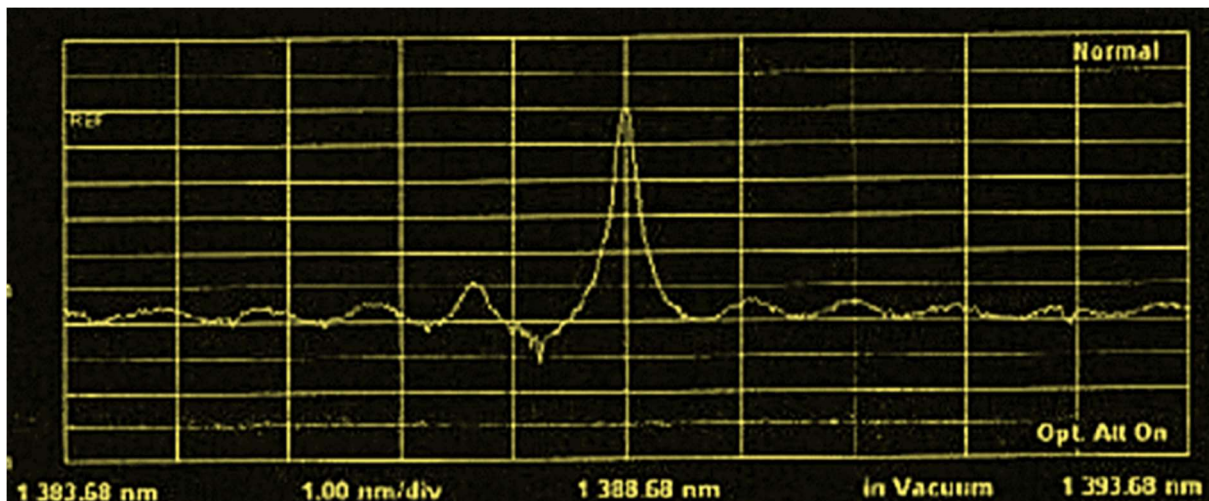

Figure 7.5: Manufacturer data of the emission spectrum of the diode laser.

The repumper laser in most labs is made by NTT-Photonics which unfortunately do not sell to BGU. Hence, we had to find an alternative solution. It is not trivial to find good diodes at this wavelength but eventually we found one such DFB laser by Frankfurt Laser Company (FPLD-1389-10-DFB-BTF). The diode output is via a single-mode fiber, and the power rating at $25°\,C$ is $10\,mW$ at $1389\,nm$ (see emission spectrum in Fig. 7.5). This laser diode is connected to a universal 14-pin butterfly laser-diode mount (Thorlabs LM1482). This laser diode is also frequency stabilized to the multi-color cavity by the PDH technique.

7.5 578 nm clock laser system

The heart of an optical atomic clock is an ultra-stable laser system, which together with the optical cavity, acts as a local oscillator. The clock transition in ^{171}Yb is at $578\,nm$ (see Figs. 1.3 and 3.1). Narrow linewidth diode lasers at this wavelength are unavailable. Instead, we use a SHG light of a quantum dot laser at $1156\,nm$ by Innolume (model 1156AR150) which is mounted inside an external cavity diode laser (ECDL) model "Cateye" by MOGLabs. This system is based on an interference filter placed inside the external cavity as depicted in Fig. 7.6.
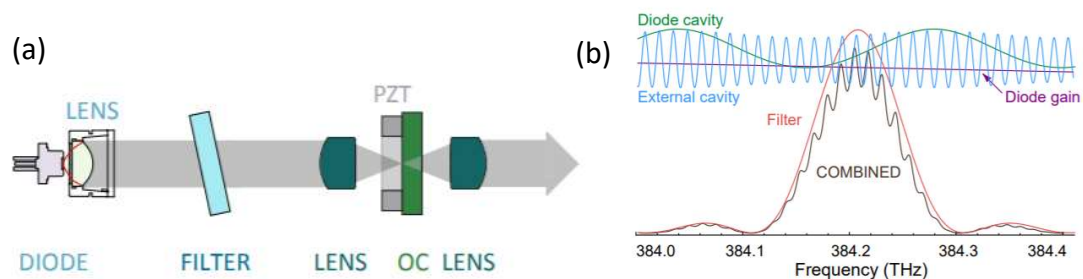
Figure 7.6: (a) A schematic description of the MOGLabs ECDL - external filter design: The light emitted from the quantum dot diode propagates through an ultranarrow intracavity bandpass filter and is retroreflected from the output coupler (OC) which is mounted on a PZT and is the front facet of the cavity. (b) General representation of the line-narrowing scheme in the ECDL configuration. Here shown for operation at a wavelength $\lambda = 780\,nm$ and external cavity length $L_{ext} = 15\,mm$. The brown peaks represent the individual modes. Taken from[86].

The output from the laser exhibits a hysteresis behavior with noticeable power jumps as the current is increased and smoother behavior when power is decreased (see Fig. 7.7).
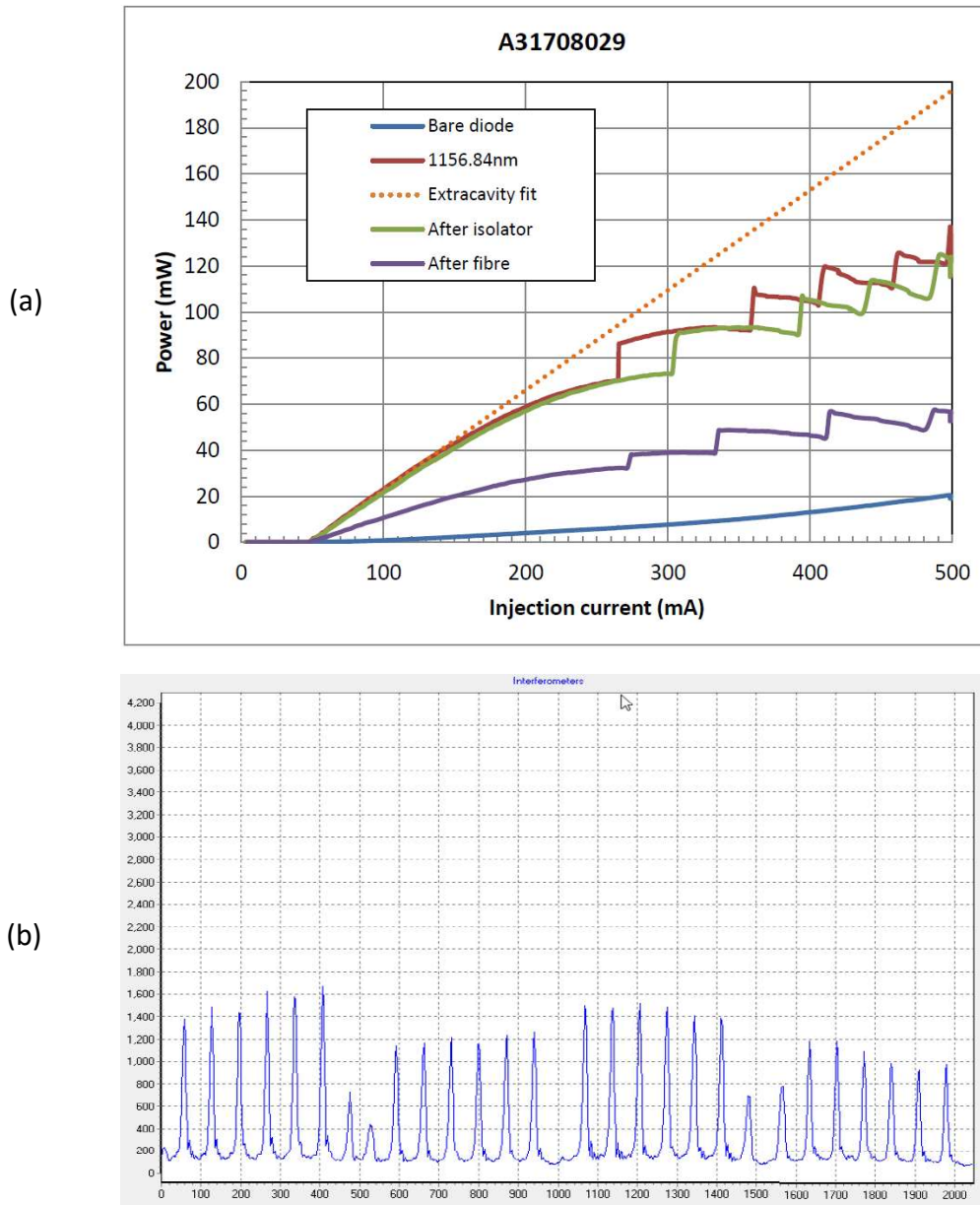
Figure 7.7: MogLabs Cateye (a) output and (b) single-mode operation from the Innolume quantum dot laser diode at 1156.84 nm.

The 578 nm light is produced by SHG in a fiber-coupled PPLN waveguide (AdvR, RSH-T0578_P98FSALO-19051051, see Fig. 7.8). After the waveguide, we can separate the remaining fundamental beam from the second harmonic beam by a dichroic mirror (Thorlabs DMLP650T). While the 578 nm beam is nicely collimated, the 1156 nm is diverging, and we have to correct it with a f=250 mm plano-convex lens. The 1156 nm power after the dichroic mirror is 28.5 mW. In Fig. 7.9 we show how the power of the two wavelengths is distributed between the optical cavity, the frequency comb, and the atoms.

Figure 7.8: AdvR PPLN waveguide. Conversion efficiency ~200%/W with ~50% coupling per facet. This means that for an input beam of $100\,\text{mW}$ we get $50\,\text{mW}$ of $1156\,\text{nm}$ in the SHG medium, that produce by the quadratic process $200\% \cdot (50 \cdot 10^{-3})^2 W^2/W = 5\,\text{mW}$ of $578\,\text{nm}$ light. After the second facet, it becomes $2.5\,\text{mW}$. In reality we obtain $10\,\text{mW}$.

The $578\,\text{nm}$ beam is double passed in a $100\,\text{MHz}$ AOM (AOM 1) crystal (Gooch & Housego 3100-125), before the light is transmitted in free space to probe the atoms. The $1156\,\text{nm}$ beam is also double passed through a $125\,\text{MHz}$ AOM (AOM 2) crystal (ACM-1202AA32.2) which is used to tune the laser frequency to the nearest resonance of the cavity. The laser is always locked on the cavity resonance using PDH. However, as the cavity starts to drift, the yellow probe beam becomes off-resonance and corrections are applied to this AOM. The output following the double pass scheme is divided to two branches. The first branch delivers the light to the cavity via an optical fiber and the second branch transmits the output of the clock to the optical frequency comb.

Figure 7.9: Optical array of the clock laser system.

58

Because these two lines are transmitted through fibers, it is necessary to perform a frequency stabilization process to avoid frequency instabilities that result from thermal or acoustic noise in the fiber. This is the role of AOM 3 and AOM 4, as well as the two PDs (see Chap. 10).

To conclude: The laser is locked to the ultra-stable reference cavity by the PDH method which narrows the laser linewidth and provides a short-term stability[73,87] of $\sim 10^{-16}$. But even this stable cavity suffers from a slow drift (about 1 MHz per year[87]). This long-term drift is detected by spectroscopy performed on the atoms in the lattice and is corrected by shifting the output frequency using an AOM (AOM2).

8. The Optical Setup Around the Science Chamber

The main part of the experiment takes place in the octagon cell (see Sec. 3.5). The atoms from the 2D MOT chamber enter this region through the differential pumping tube (DPT) at an estimated velocity of few tens of m/s (see Fig. 8.1). This is followed by a series of preparation steps inside the octagon. First, a pulse of a counter propagating slowing 399 nm beam is applied before a second stage MOT using the green laser (556 nm) is performed. In parallel, a 759 nm lattice beam is always present and ultra-cold atoms can already be trapped in this potential. Once atoms are loaded into the lattice, it is necessary to cool them to the ground state of the lattice potential and sideband cooling (see Sec. 2.2.2), Spectroscopy (578 nm), and detection (399 nm and 1389 nm) are performed to this end. To complete the preparation of the atoms, a spin polarization (556 nm) step is performed, using an external magnetic bias field and a pulse of the green laser along the same direction. Only after all these preparation steps are performed, we can start to measure the clock transition and detect the number of atoms in each state. All of these operations around a small volume require a detailed and careful design of a complicated optical setup which will be described in the following.

The 399 nm slowing beam enters the chamber through the CF16 viewport opposite the DPT.

The 556 nm light for the 3D MOT enters the cell via three orthogonal windows as explained in Sec. 3.5 and shown in Figs. 8.1 and 8.2.

The 759 nm lattice beam enters the cell via the bottom CF16 viewport. To enhance the lattice potential, it is designed in a concentric FP resonator that supports a standing-wave with a narrow waist in the center of the cell. The FP resonator is made from two concave mirrors (Thorlabs CM254-150-E03, ROC=150 mm), which are mounted 300 mm apart. The FP is stabilized by placing one of the mirrors on a PZT. The input lattice beam is focused in the middle of the octagon to a waist of few tens of μm[88,89].

The 578 nm clock laser beam is overlapped with the lattice beam by a dichroic mirror (Thorlabs DMBP740B) as shown in Fig. 8.1. This mirror has a transmission window for $\lambda<740$ nm and for $\lambda>940$ nm, so we can also take advantage of the same dichroic mirror to transmit the repumper beam on the same axis.
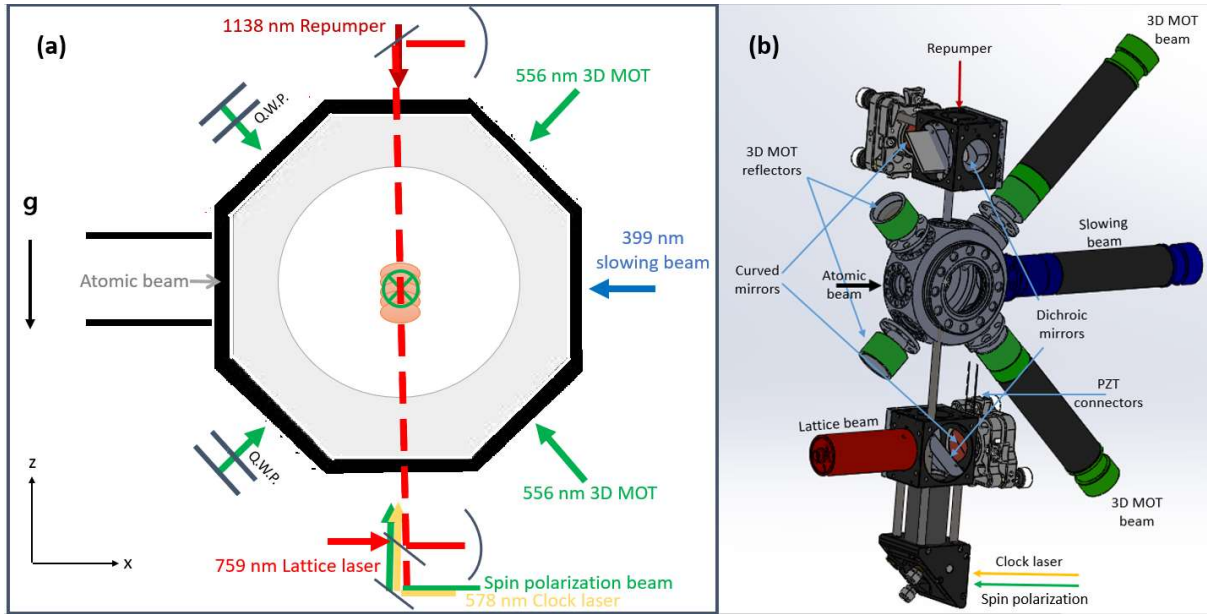
Figure 8.1: (a) A schematic 2D view and (b) 3D view of the octagon cell including the optical elements in the X-Z plane. These include: A collimator for the slowing 399 nm beam, two collimators for the retro-reflecting green MOT beams and holders for the λ/4 waveplates and mirrors on the opposite sides. The lattice beam optical assembly comprising a FP resonator made by two concave mirrors. The lattice beam enter the cell via a 45° dichroic mirror. The clock and the repumper beams enter the cell via the same dichroic mirror. The green X in the middle of (a) depicts the third beam axis for the 556 nm 3D MOT, along the y axis.

We perform fluorescence detection by collecting the blue 399 nm fluorescence light, caused by a pulse of 399 nm excitation beam originating from the same direction as the 399 nm slowing beam. The fluorescence detection is done at a 90° angle from the excitation beam. To optimize the signal to noise ratio we need to collect as many photons as possible by increasing the detection solid angle as much as possible. For this reason, we position a 2" lens (Thorlabs LA1401-A, f = 60 mm) close to the CF40 viewport, only 50 mm from atoms (see Fig. 8.2). The diameter of the optical aperture of the CF40 viewport is 1.42", and its distance from the center of the cell is 25 mm, so we collect light from solid angle of 1.16 sr (about 9.2% of a full sphere). The difficulty in this configuration is that the third beam of the green MOT also needs to enter the chamber through this lens and window. We can overcome this problem by selecting a second lens (Thorlabs LA1399-A, f=175 mm), which is placed 85 mm from atoms. The combination of these two lenses allow to focus the collected fluorescence signal further away from the center of the octagon on a PMT after it is reflected by a dichroic mirror (Thorlabs DMLP490R). The collimated green MOT beam is achieved by entering a 15 mm diameter circularly polarized beam into the cell through the opposite CF40 viewport. As this beam exits

the cell, it passes through the abovementioned two lenses and is focused before transmitted through the dichroic mirror. We then use a third, f=125 mm lens (Thorlabs LA1384-A), which is positioned 190 mm from the center of the octagon to re-collimate the beam. The collimated beam then continues to travel through a λ/4 waveplate before being retroreflected by a mirror.
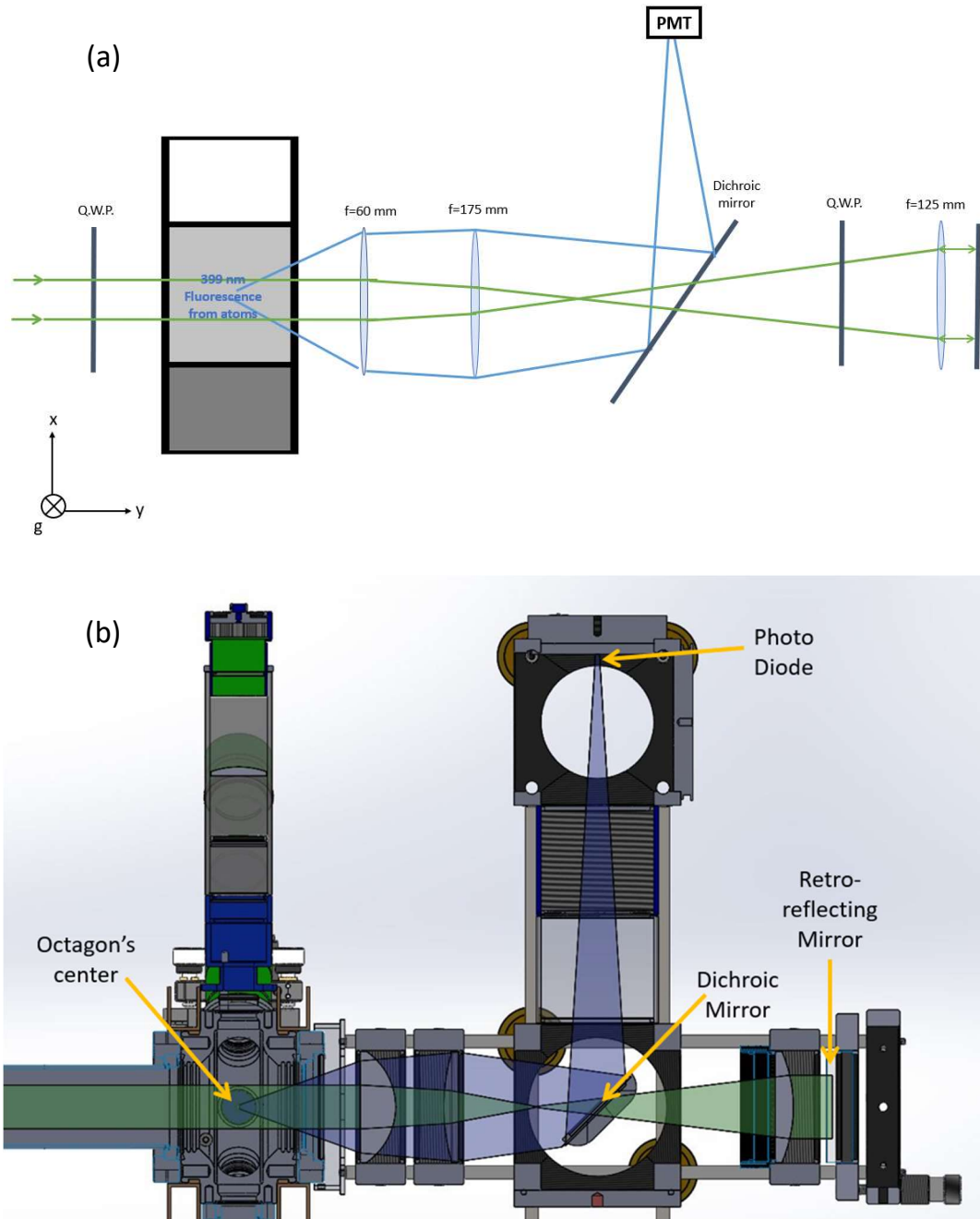

Figure 8.2: (a) A schematic drawing to demonstrate the optical bench designed in order to perform 399 nm fluorescence detection and enter a 556 nm MOT beam on the same axis. (b) A SolidWorks simulation of the octagon in the X-Y plane demonstrating how all the optical elements are mounted. The green beam is not to scale. The clock interrogation sequence is described in Sec. 3.1.

9. The Optical Frequency Comb (OFC)

9.1 History and Basics of the OFC

One of the major difficulties in the realization of optical clocks is the need to bridge the gap between the clock frequency (in the order of hundreds of terahertz) and the frequency of digital electronic devices (which have an operational bandwidth of few GHz at most), without degrading the frequency stability which is realized in the optical domain. This down-conversion step is necessary for making comparisons with other clocks and for time and frequency dissemination for the purpose of synchronization of remote systems. During the last decades of the previous century, frequency down-conversion was performed by means of complex frequency chains capable of filling the frequency gap[11]. However, these devices were based on a combination of several intermediate transfer oscillators that generated a progressively higher frequency, always related to the reference microwave that, in turn, was referenced to the primary frequency standard. Because of the complexity of this process, it was unreliable and could not form a base for an optical frequency standard.

The OFC was developed in the late 1990's by J. L. Hall and T. W. Hänsch (Nobel prize in 2005). Around the year 2000, the realization of the optical frequency comb (OFC) allowed for the replacement of these complex frequency chains, thus enabling a vast simplification in precision optical measurements and rapid progress in the development of various types of optical atomic standards.

The OFC is based on a mode-locked laser (MLL) producing a train of ultra-short optical pulses at a repetition rate $f_{rep} = c/2L$, determined by the length of the laser cavity, L. According to Fourier theory, an ultrashort pulse will incorporate a broad range of frequencies, the extent of which is proportional to the inverse of the pulse duration, τ_{FWHM}. However, for an infinite periodic train of pulses, the frequency spectrum will consist of discrete, infinitely narrow frequency components, creating an optical frequency comb instead of a continuous band of frequencies: $\nu_n = \omega_n/(2\pi)$, with Fourier amplitude components, A_n, and mode number, n, such that

$$E(t) = A(t)e^{i\omega_c t} = \sum_{n=n_i}^{n_f} A_n e^{i\omega_n t}, \qquad (9.1)$$

where ω_c is the fundamental mode of the laser (the carrier) angular-frequency. These components, corresponding to the coherent modes of the laser cavity, are spaced by the repetition frequency of the laser which depends on the round-trip time in the laser cavity, T,

adhering to the relation $f_{rep} = 1/T$ (see Fig. 9.1). Because the carrier frequency, $\nu_c = \omega_c/2\pi$, is not necessarily an exact multiple of the mode spacing, f_{rep}, the individual Fourier frequencies are shifted from integer multiples of f_{rep} by a common offset, $f_{ceo} \leq f_{rep}$, such that

$$\nu_n = n \cdot f_{rep} + f_{ceo}, \qquad (9.2)$$

where n is a large integer of the order of 10^6 that indexes the comb line, and f_{ceo} is the carrier - envelope offset (CEO) frequency[90]. Eq. 9.2 is referred to as the comb equation.

The physical source of this offset is the dispersion of the laser cavity. The dispersion causes the pulse envelope, which propagates at the group velocity, v_g, to lag behind the carrier electric field, which propagates at the phase velocity, v_p. Fig. 9.1(a) shows how this phenomenon causes a constant phase difference between the carrier and the envelope of

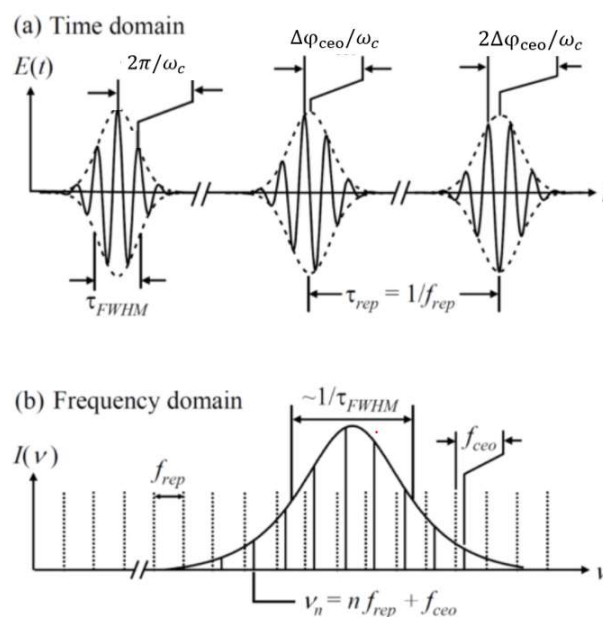$$\Delta\varphi_{ceo} = L \cdot \omega_c \left(\frac{1}{v_g} - \frac{1}{v_p} \right). \qquad (9.3)$$

Figure 9.1: (a) The output of an MLL in the time domain. The laser produces a periodic train of ultrashort pulses having a duration of τ_{FWHM} and a repetition frequency of $f_{rep}=1/T$ (in this figure T represented as τ_{rep}). The difference between the group and phase velocities in the laser cavity causes the peak of the oscillating carrier electric field to shift with respect to the peak of the envelope from one pulse to the next by an amount $\Delta\varphi_{ceo}$, the CEO phase shift. (b) The corresponding frequency-domain output of an MLL. The periodic train of pulses produces a comb of discrete frequency components with an extent that is inversely proportional to the duration of each pulse and a spacing that is given by the repetition frequency of the pulse train. The CEO phase-shift uniformly shifts the components of the optical frequency comb from integer multiples of the repetition frequency. This uniform shift, or CEO frequency, f_{ceo}, is proportional to $\Delta\varphi_{ceo}$. Every component of the frequency comb is uniquely determined by the two degrees of freedom of the comb, f_{rep} and f_{ceo}. Taken from [91].

In the spectral domain, a rigid shift will occur for the frequencies at which the pulses add constructively. Since the same phase difference, $\Delta\varphi_{ceo}$, is accumulated for any round-trip with period time T (see Fig. 9.1), this shift is determined to be $f_{ceo} = \Delta\varphi_{ceo}/2\pi T = \Delta\varphi_{ceo}f_{rep}/2\pi$.

According to the comb equation (Eq. 9.2), in order to achieve a stabilized comb, both f_{ceo} and f_{rep} must be stabilized. Nonetheless, it is sufficient to use a microwave clock with a fractional uncertainty $< 10^{-12}$ to achieve a fractional uncertainty $< 10^{17}$ in the optical frequency.

9.2 Stabilization of f_{ceo} and f_{rep}

The CEO frequency is detected and stabilized by the f-to-2f technique. First, it is necessary to broaden the spectrum wider than one octave. However, the spectrum bandwidth generated from an ordinary mode-locked Ti:sapphire oscillator is generally less than 100 nm. To produce an octave-spanning spectrum, photonic crystal fiber (PCF), an ideal material with high effective nonlinearity, is used to extend the spectrum by the self-phase-modulated femtosecond laser pulse generated from ordinary Ti:sapphire oscillators.

If the spectrum is sufficiently broad, for example covering over a full octave, then it is possible by the heterodyne beating technique to isolate and stabilize f_{ceo}. This is carried out by separating the low frequency end of the spectrum from the high end by a dichroic mirror. The low end of the spectrum is frequency-doubled using a nonlinear LBO crystal to obtain $2\nu_n$. The frequency of the tooth index 2n at the high end of the spectrum is given by $\nu_{2n} = 2nf_{rep} + f_{ceo}$. Next, we combine the two beams so the beating frequency, which is detected on a fast photodiode, is the CEO frequency

$$2\nu_n - \nu_{2n} = 2(nf_{rep} + f_{ceo}) - (2nf_{rep} + f_{ceo}) = f_{ceo}. \tag{9.3}$$

This "f-to-2f" measurement technique is also termed "self-referencing". The detected f_{ceo} can be stabilized by comparing it to a reference frequency from a microwave atomic standard and a servo loop which operates on the pumping power of the MLL.

The repetition frequency, f_{rep}, is stabilized by phase-locking the heterodyne beat between an optical standard reference frequency and the nearest comb component to a microwave reference. The heterodyne output drives a servo system that operates on a piezo crystal that controls the cavity length and consequently varies f_{rep}.

An alternative method to avoid the stabilization of f_{ceo} is to generate a difference frequency generation (DFG) comb (see Fig 9.2)[92]. The DFG comb (red line) is produced by mixing of the high frequency part (n_h) and the low frequency part (n_l) of the fundamental comb spectrum (blue line), given by

$$\nu_{DF} = (n_h f_{rep} + f_{ceo}) - (n_l f_{rep} + f_{ceo}) = (n_h - n_l) f_{rep} \qquad (9.4)$$

The resulting difference comb is independent of f_{ceo}, meaning that the CEO of the DF pulse train is zero and the carrier-envelope phase of every pulse is the same.
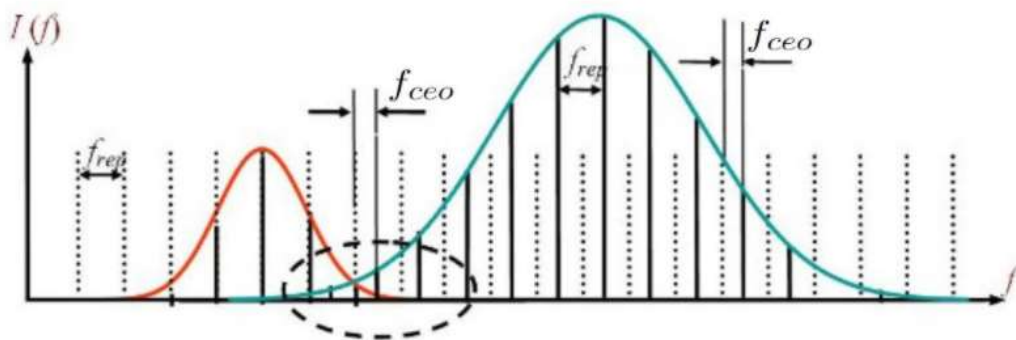

Figure 9.2: (Blue) The original super continuum frequency comb. (Red) The f_{ceo}–free difference frequency comb generated by subtracting the low-end from the high-end parts of a supercontinuum comb in a nonlinear crystal.

9.3 Menlo Systems FC1500-ULNplus OFC

There are only few companies that produce optical frequency combs. As noted, this sophisticated equipment must not degrade the stability of the optical standard when used for frequency dissemination for comparisons between various optical frequency standards or synchronization. This is not easy to realize and, to date, comparisons between optical clocks in national metrology centers are performed with Menlo Systems combs[93]. We have decided to purchase the latest model: FC1500-ULNplus OFC. This comb is based on a femtosecond Er-doped polarization-maintaining fiber oscillator operating at a repetition rate (f_{rep}) of 250 MHz and a center wavelength of 1560 nm. The oscillator contains two intra-cavity EOMs that enable MHz bandwidth stabilization of both f_{rep} and f_{ceo} with minimal cross-talk. Additional low-bandwidth piezo and thermal actuators extend the tuning range of f_{rep} , while enabling the comb to remain locked for months at a time[94]. Data of the comb are shown in table 9.1.

SPECIFICATIONS	FC1500-250-ULN**PLUS**
Comb Spacing	250 MHz
Accuracy	1×10^{-18} for $\tau > 100s$*
Stability▲	5×10^{-18} in 1s*△, 5×10^{-19} in 1000 s*△
Integrated Phase Noise	<80 mrad [1 Hz-2 MHz]
Linewidth	<1 Hz*♦
Tuning Range of Spacing Between Individual Comb Lines	>4 MHz
Tuning Range of CEO Frequency	>250 MHz
Laser Outputs	five fiber-coupled, linearly polarized, PM output ports, 1560 nm
Spectral Range	>25 nm (500-1050 nm with M-VIS, 1050-2100 nm with M-NIR)
Average Output Power	>10 mW from each laser port (>100 mW with M-VIS, >200 mW with M-NIR)
CW Laser Inputs	approx. 1 mW optical power required, wavelength user-defined in the 500-2100 nm range (more upon request)

▲ *spectral purity transfer between fundamental and a user-defined wavelength in the 500-2100 nm range,* *phase lock to optical reference,* △ *modified Allan deviation (λ-type counter, timebase 1ms),* ♦ *limited by resolution bandwidth of analyzer*

Table 9.1: manufacturer data of the FC1500-ULNplus OFC.

9.4 State-of-the-Art of OFC Field

As the field of OFC becomes more mature and the technology is advancing, various producers of OFC enter the market. Below is a list of links to companies that produce frequency combs. Nonetheless, to this date, the only company that reports on specifications similar to Menlo Systems is Toptica Photonics, which uses a DFG comb scheme.

- https://www.menlosystems.com/
- https://www.laserquantum.com/products/detail.cfm?id=100
- http://avesta.ru/en/product/efo-comb-optical-frequency-comb-synthesizer/
- https://www.toptica.com/products/frequency-combs/
- https://www.imra.com/products/imra-scientific/frequency-comb
- https://www.vescent.com/products/lasers/ffc-100-frequency-comb/

In addition to the traditional technology of OFC which is based on comb generation by an MLL, recent developments of micro OFCs which are based on micro-disk resonators driven by a CW laser begin to evolve[95,96]. For an updated review on the field of microcomb resonators, I direct the reader to Ref. 97.

10. Phase Stabilization of Optical Fiber Links

The clock system requires the use of optical fibers to transmit light from the clock laser to other components, i.e., the reference cavity and the frequency comb. Furthermore, the lattice clock is designed to disseminate its stable frequency via optical fibers to other centers in order to perform frequency comparisons[98] or synchronization. The use of optical fibers may cause instabilities in the laser light phase due to changes in length and index of refraction in the fiber, which are mainly caused by temperature fluctuations, torsion, vibrations, and so on.

To compensate these phase variations, a Michelson interferometer scheme is implemented (see Fig. 10.1). The input light from the laser is reflected by a PBS cube towards an AOM operating at 80-125 MHz. The local (reference) arm of the interferometer includes the zero-order beam which is not affected by the AOM. This beam is passed through a $\lambda/4$ waveplate before it is retroreflected by a mirror. The returning beam is transmitted through the input PBS and is aligned by a mirror to hit a fast amplified PD (EOT ET-3000A). The remote arm of the interferometer includes the first-order diffraction from the AOM which is passed through the optical fiber. At the exit from the fiber, a fraction of the light is reflected by a non-polarizing beam splitter (BS) cube, while the other fraction is transmitted towards the other clock components such as the cavity and the comb. This reflected fraction is passed in a $\lambda/4$ waveplate before it is retroreflected by a mirror through the same $\lambda/4$ waveplate and all the way back through the fiber, the AOM, and the input PBS until it also hits the same PD. The beams from the local and the remote arms of the interferometer have the same polarization and interfere with each other on the PD. The detected beat note will appear at twice the modulation frequency of the AOM (160-250 MHz). The noise added by the round trip through the fiber is considered to be identical in both directions due to the fact that the speed of light is much faster than the rate at which the fiber noise is changed.

This beat note is compared in a phase locked loop (PLL) to the original drive frequency of the AOM. This frequency is synthesized from a 10 MHz signal from an atomic clock (AccuBeat AR76) having a long-term fractional instability of 10^{-11}. Any detected deviations of the beat note frequency from the AOM driving RF frequency are attributed to phase fluctuations which are acquired in the remote arm. These fluctuations can be compensated by implementing fast corrections on the AOM frequency[99] (see details in the appendix).
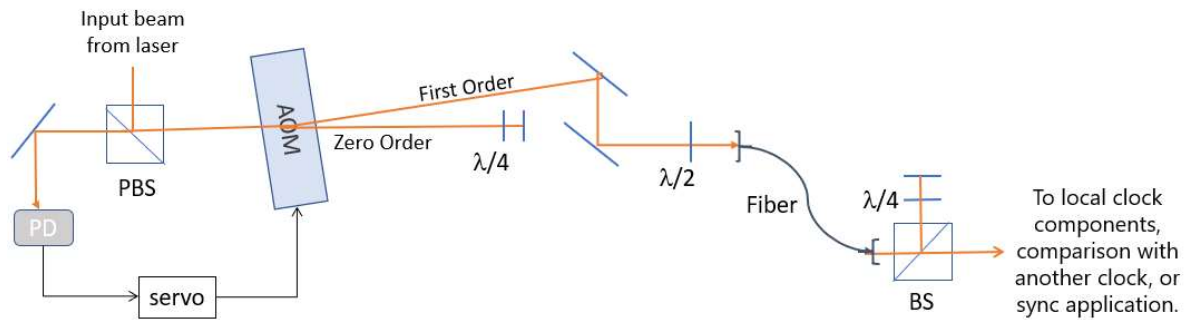
Figure 10.1: A typical scheme of a fiber-link phase stabilization system. In this design, care is given to avoid reflections from the returning beams towards the laser source.

In addition to such local optical links, which are necessary for the clock operation, optical fibers are ideal for frequency dissemination over long distances. This can be realized by transmitting the light of a telecom wavelength laser, which is locked to the stabilized frequency comb. The stabilized light can travel in a dedicated dark fiber link[100] or via a dark channel link[98]. In both cases, the realization of the Michelson interferometer stabilization scheme is used to ensure that the transmitting medium will not introduce phase and amplitude noises in the signal. In addition, it is necessary to overcome attenuation problems due to insertion losses into the fibers and due to absorption and scattering along the fiber length. Therefore, amplifiers must be inserted for long haul frequency dissemination, while the amplifiers must be bi-directional and must keep the phase of the carrier frequency[20].

As noted, two different approaches are used, either a 'dark fiber' or a 'dark channel'. The first approach relies on a fiber that is solely used for the frequency transfer. In the second approach, wavelength-division multiplexing is employed where several optical carrier signals travel in a single optical fiber in different channels and only one channel is free from internet traffic. The dark fiber approach is more expensive but has the advantage that more extensive modifications of the fiber lines are possible, for example, Brillouin amplification[101] with higher power, thereby reducing the number of repeater stations considerably[20].

A use of a dark channel, for example, can be found in the European clocks network[99], with a robust long distance (540 km) phase stabilized optical link along public telecommunication lines. In this "dark channel" technique, the C-band is divided to $100\,\mathrm{GHz}$ channels ($0.8\,\mathrm{nm}$) by dense wavelength division multiplexing (DWDM). One channel is sufficient and can easily support the propagation of the ultra-stable signal, leaving the rest of the wavelength window available for data transmission. Depending on many parameters, such as length, fiber noise, amplifiers along the way, etc. in the general case, for a $\sim 200\,\mathrm{km}$ link, the frequency instability

can be expected to be $< 10^{-15}\tau^{-1}$, allowing to reach 10^{-19} accuracy in only 10,000 seconds. The dark channel technique is enabled by applying various elements such as passive optical filters, and optical add/drop multiplexers (OADM) to inject or extract a single channel from the DWDM flux. The typical design of a dark channel link between two optical clocks is shown in Fig. 10.2.
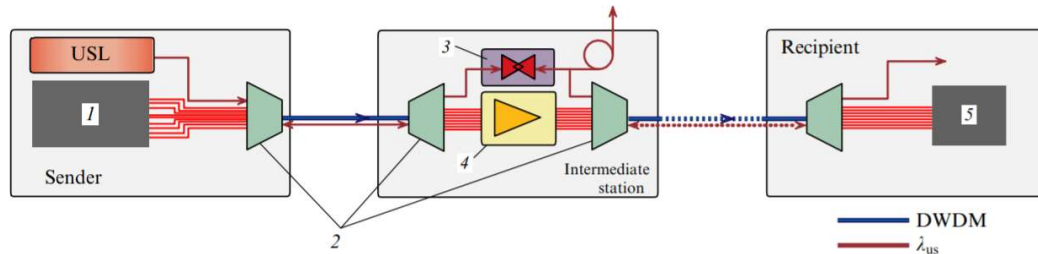

Figure 10.2: Frequency dissemination scheme using internet links. The distance between the intermediate stations is less than 50 km. 1- transmitter, 2 - optical add/drop multiplexor (OADM), 3 - bidirectional erbium-doped fiber amplifier, 4 - unidirectional optical amplifier, 5 – detector, DWDM – traffic of data converted using the dense wavelength division multiplexing method; here λ_{us} is the ultra-stable frequency signal. Taken from[99].

In the coming years we aim to form an optical clocks network. The first node of this network will connect between our ^{171}Yb lattice clock and the Sr$^+$ and Ca$^+$ optical ion clocks, built at the Weizmann Institute (by Prof. Roee Ozeri's group[49]). This is in order to perform comparisons against an external and independent source of an optical frequency standard. Without such a comparison, the performance of our clock can be evaluated only by systematic analysis of the most dominant perturbations, where the comparison with another clock, with accuracy of similar level, provides us with an external estimation of the clock systematic uncertainty.

Figure 10.3: The IUCC optical network grid in Israel.

The straightforward way for linking between the optical clock labs in BGU and the Weizmann Institute of Science will be based on the infrastructure of the inter-university computation center (IUCC) optical fiber network. The layout of this network is depicted in Fig. 10.3. The plan is that both the Weizmann institute and BGU will be connected through Tel-Aviv university. The distances from each lab to the connecting junction in Tel-Aviv are relatively short and the number of amplifiers that will have to be installed along the route is minimal. In average it is necessary to put an amplifier every 20 dB of losses. Hence, we expect that the degradation of the signal between the labs will not require installing complicated components such as regeneration laser stations along the path, like there are in similar systems in Europe[98], where the distances are much larger.

11. Summary and Outlook

The optical clock project presented in this thesis is a very complex project. During my M.Sc. I have built and/or operated and optimized the following components:

1. Locking the clock laser to the 30 cm high-finesse cavity.
2. Locking the 798 nm and 1112 nm lasers to the 5 cm long cavity.
3. Designing and winding the Zeeman slower coils.
4. Designing and assembling the vacuum system, include the oven, the two MOT cells, the coils and the optical components.
5. Assembling the bow-tie cavity, and optimizing the SHG of the 399 nm light from the 798 nm beam.
6. Operating and characterizing the commercial Menlo System frequency comb.

The optical clock is still under development and we aim to complete it as soon as possible for initial characterization. Later, there will certainly be a process of improvements and implementations. We can divide these activities to short- and long-term goals.

Short-term goals:

a. Optimizing the laser lock to the cavity and measuring the laser linewidth against an independent sub-Hz laser system from Menlo systems.
b. Comparing the 2D MOT loading from the Zeeman slower vs. the dispenser.
c. Comparing the loading time, and size of the 3D MOT when loaded from a 2D MOT or when loaded by optical deflection of the atomic beam which is emitted from the Zeeman slower.

Long-term goals:

a. Realizing a stable optical link between the lattice clock in BGU and the ion clocks in the Weizmann Institute.
b. Improving the systematic uncertainties in our current system e.g., reducing BBR uncertainty by replacing the stainless-steel chamber with a copper chamber or a cryogenic lattice environment.
c. Investigation of different lattice configurations.
d. Continuous long-term stable operation of the clock.
e. Contribution to synchronization of advanced high-rate systems in Israel.

f. Shortening the clock cycle by implementing non-destructive measurements for counting the atoms.

g. Exploring methods to improve the standard quantum limit stability by implementing squeezing protocols.

h. Finally, incorporating this unique metrological device in investigations of the foundations of quantum theory by pushing the boundaries of precision measurements, as well as testing exotic theories concerning dark matter, dark energy, supersymmetry, and extensions to quantum mechanics.

Appendix: Phase Noise Cancelation in an Optical Fiber-Link

This appendix includes a general mathematical analysis of a phase-locked loop (PLL), and in particular a fiber phase stabilization loop as exists in our clock system. At the end of the discussion, an idea is obtained regarding the filter $F(\omega)$ component that corresponds to the system, depending on its parameters (fiber length and refracting index, etc.), and also an expression of phase noise that cannot be eliminated by the PLL system as a function of ω.

Frequency Dependence Phase-Locked Loops

The basic principle of any PLL is as follows: the oscillator to be stabilized has a tuning input that can be controlled by applying a voltage. This is commonly referred to as a *voltage-controlled oscillator* (VCO). The VCO frequency is compared to a stable reference by feeding both into a phase detector. The phase detector (e.g., a frequency mixer) returns a voltage V_{PD} that depends on the phase difference $(\varphi_{in} - \varphi_{out})$ [100]

$$V_{PD} = G_0 \cdot (\varphi_{in} - \varphi_{out}), \tag{A.1}$$

with the device-dependent gain factor G_0. The loop filter transforms this error signal into a control signal that suppresses noise and high frequency components. The VCO is steered by the control voltage with a transfer function $h(t)$. In the Laplace domain it is transformed into the loop filter response function H(s): $h(t) \xrightarrow{\mathcal{L}} H(s)$, with the imaginary variable $s = i\omega$

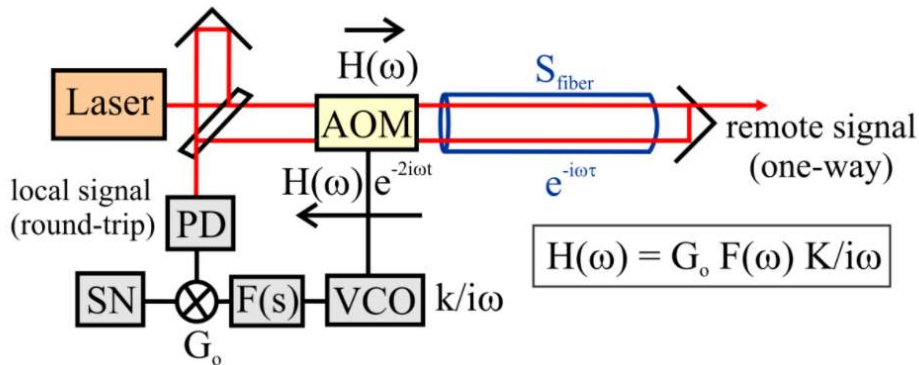$$H(s) = \int_{-\infty}^{\infty} h(t)e^{-st}dt. \tag{A.2}$$

Figure A.1: An experimental setup for a phase noise compensation scheme of an optical fiber link. Taken from[102].

For Laplace transform pairs (as for Fourier transform), the following relations are useful[100]:

$$\frac{d^n h(t)}{dt} \overset{\mathcal{L}}{\leftrightarrow} s^n H(s); \tag{A.3}$$

$$g(t) = \int_{-\infty}^{t} h(\tau)d\tau \overset{\mathcal{L}}{\leftrightarrow} H(s)/s; \tag{A.4}$$

$$g(t-\tau) \overset{\mathcal{L}}{\leftrightarrow} G(s)e^{-s\tau}. \tag{A.5}$$

Using Eqs. A.1 - A.5 yields the characteristic loop parameters

$$\tilde{V}_{PD}(s) = G_0[\tilde{\varphi}_{in}(s) - \tilde{\varphi}_{out}(s)]; \tag{A.6}$$

$$\tilde{V}_C(s) = F(s)\tilde{V}_{PD}(s); \tag{A.7}$$

$$\tilde{\varphi}_{out}(s) = K_{VCO}\tilde{V}_C(s)/s, \tag{A.8}$$

with the loop filter function $F(s)$. The system transfer function for the forward light, $H(s)$, is

$$H(s) = G_0 K_{VCO} F(s)/s. \tag{A.9}$$

Fig. A.1 shows a phase noise compensation scheme which is applied to the stabilization of an optical fiber link. The phase noise induced by the fiber link is detected by beating the round trip beam with the input reference beam on a fast PD. The beating frequency is compared to a stable reference using a mixer. Any detected phase difference is converted to voltage with a gain G_0, filtered with a transfer function $F(s)$, converted to frequency using VCO with transfer function (K_{VCO}/s), and then sent to VCO to control an AOM which compensates the phase changes in the transferred frequency.

We can analyze the effect of the compensation system on the light that propagates forwards and backwards in the link. The system transfer function for the forward light is $H(s)$ and for the return light after round-trip time of 2τ is $H(s) \cdot e^{-2i\omega\tau}$. Therefore, the transfer function of the compensation system (open loop gain) is

$$G(s) = (1 + e^{-2i\omega\tau})G_0 K_{VCO} F(s)/s. \tag{A.10}$$

Finally, the phase noise is suppressed by the error transfer function $(1+G(s))^{-1}$, so the phase noise spectral density is[103]

$$S_{out}(s) = \left|\frac{1}{1+G(s)}\right|^2 S_{in}(s). \tag{A.11}$$

Phase Noise Cancelation in Fiber Links

Thermal and acoustic noises along a fiber may induce a phase shift $\delta\varphi(z, t)$ on the light passing the fiber at time t and position z.
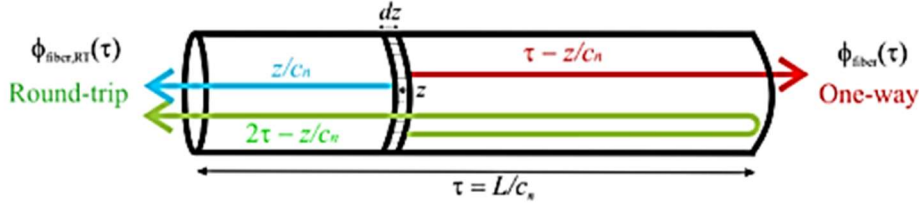

Figure A.2: A round-trip and a one-pass detection of an event takes place at position z along a fiber with length L. Taken from[102].

The accumulated phase noise in the forward direction from the position $z = 0$ to $z = L$ at time t is [102]

$$\varphi_{fib} \ (t) = \int_0^L \delta\varphi\big(z, t - (\tau - z/c_n)\big)dz, \tag{A.12}$$

where $\tau = L/c_n$ is the propagation time delay in the fiber and c_n is the speed of light in the fiber.

Part of this light is then returned in the fiber for phase noise detection and compensation. The phase noise accumulated by the round-trip at a time t is

$$\varphi_{fiber,RT}(t) = \int_0^L [\delta\varphi(z, t - z/c_n) + \delta\varphi(z, t - (2\tau - z/c_n))]dz. \tag{A.13}$$

The above equations are in the time domain. Using a Fourier transformation, the two equations are represented in the frequency domain

$$\tilde{\varphi}_{fiber}(\omega) = \int_0^L e^{-i \ (\tau - z/c_n)} \delta\tilde{\varphi}(z, \omega)dz; \tag{A.14}$$

$$\tilde{\varphi}_{fiber,RT}(\omega) = \int_0^L [e^{-i \ (z/c_n)} + e^{-i\omega(2\tau - z/c_n)}]\delta\tilde{\varphi}(z, \omega)dz; \tag{A.15}$$

or

$$\tilde{\varphi}_{fiber,RT}(\omega) = \int_0^L e^{-i\omega\tau}[e^{i\omega(\tau - z/c_n)} + e^{-i\omega(\tau - z/c_n)}]\delta\tilde{\varphi}(z, \omega)dz.$$

Using the relation: $\cos(x) = \frac{e^{ix} + e^{-i}}{2}$, we get

$$\tilde{\varphi}_{fiber,RT}(\omega) = 2\int_0^L e^{-i\omega\tau}\cos(\omega(\tau - z/c_n))\delta\tilde{\varphi}(z, \omega)dz. \tag{A.16}$$

The phase noise spectral density is defined as: $S(\omega) = |\tilde{\varphi}(\omega)|^2$. Under the assumption that the phase noise of the light inside the fiber is uncorrelated in position, we can get the phase spectral

density for a length element of the fiber, and then integrate it for all the fiber length. Using Eq. A.14 and the relation $|e^{ix}|^2 = 1$ we can find the phase noise spectral density for a fiber element

$$dS_{fiber}(\omega, z) = \langle |\delta\tilde{\varphi}(z, \omega)|^2 \rangle, \tag{A.17}$$

and for the total fiber length in the one pass

$$S_{fiber}(\omega) = \int_0^L \langle |\delta\tilde{\varphi}(z, \omega)|^2 \rangle dz = L \cdot dS_{fiber}(\omega, z). \tag{A.18}$$

In the same way, the phase noise spectral density element $dS_{fiber,RT}(\omega, z)$ in the round-trip light is

$$dS_{fiber,RT}(\omega, z) = 4\langle |\cos[\omega(\tau - z/c_n)]|^2 \rangle \langle |\delta\tilde{\varphi}(z, \omega)|^2 \rangle. \tag{A.19}$$

Since $\langle |\delta\tilde{\varphi}(z, \omega)|^2 \rangle = dS_{fiber}(\omega, z) = \frac{S_{fiber}(\omega)}{L}$, and using the relation $cos^2(x) = \frac{1}{2}(1 + \cos(2x))$, we get

$$S_{fiber,RT}(\omega) = 4\frac{S_{fiber}(\omega)}{L}\int_0^L \langle |\cos(\omega(\tau - z/c_n)|^2 \rangle\, dz = \tag{A.20}$$

$$= 2\frac{S_{fiber}(\omega)}{L}\langle \int_0^L \left[1 + \cos\left\{2\omega\left(\tau - \frac{z}{c_n}\right)\right\}\right] dz \rangle,$$

and by integration

$$S_{fiber,RT}(\omega) = 2\frac{S_{fiber}(\omega)}{L}\left[L + \frac{L}{2\omega\tau}\sin(2\omega\tau)\right] = 2S_{fiber}(\omega)[1 + sinc(2\omega\tau)]. \tag{A.21}$$

It is important to note that at low frequencies the round-trip phase noise is four times higher than the one-pass phase noise, and at higher frequencies it is only two times higher (sinc(0) = 1, sinc(x>>1)≈0).

The transfer function (open loop gain) of the compensation system is (see Eq. 11. Here we use ω=s/i)

$$G(\omega) = G_0 F(\omega)K\frac{(1 + e^{-2i\omega})}{i\omega} = G_0 F(\omega)K\left[\frac{1}{i\omega} + \frac{\cos(2\omega\tau) - i\sin(2\omega\tau)}{i\omega}\right] = \tag{A.22}$$

$$= -\frac{G_0 F(\omega)K}{\omega}[\sin(2\omega\tau) + i(1 + \cos(2\omega\tau))].$$

The compensated round-trip signal is obtained by applying the error transfer function $(1+G(\omega))^{-1}$ to the round-trip phase noise, and obtain the local spectral density (see Eq. A.11)

$$S_{local}(\omega) = \left|\frac{1}{1+G(\omega)}\right|^2 \cdot S_{fiber,RT}(\omega). \tag{A.23}$$

The phase change and the magnitude of the gain that result from the PLL are obtained as follows:

$$|G(\omega)|^2 = \left(\frac{G_0F(\omega)K}{\omega}\right)^2 [sin^2(2\omega\tau) + 1 + 2\cos(2\omega\tau) + cos^2(2\omega\tau)] = 2\left(\frac{G_0F(\omega)K}{\omega}\right)^2 [1 + \cos(2\omega\tau)].$$

And using the relation $1 + \cos(2\omega\tau) = 2\,cos^2(\omega\tau)$ we get an expression for the gain magnitude $A(\omega)$

$$A(\omega) = |G(\omega)| = 2\left(\frac{G_0F(\omega)K}{\omega}\right)\cos(\omega\tau). \tag{A.24}$$

The phase of the gain transfer function $\phi = tan^{-1}(\frac{Im(G)}{Re(G)})$, (using the trigonometric identities for double angle), is

$$\phi = tan^{-1}\left[\frac{1 + cos(2\omega\tau)}{sin(2\omega\tau)}\right] = tan^{-1}\left[\frac{2cos^2(\omega\tau)}{2\sin(\omega\tau)\cos(\omega\tau)}\right] = tan^{-1}[cotan(\omega\tau)] =$$

$$= tan^{-1}[-\tan(\omega\tau + \pi/2)],$$

and hence

$$\phi = -(\omega\tau + \pi/2). \tag{A.25}$$
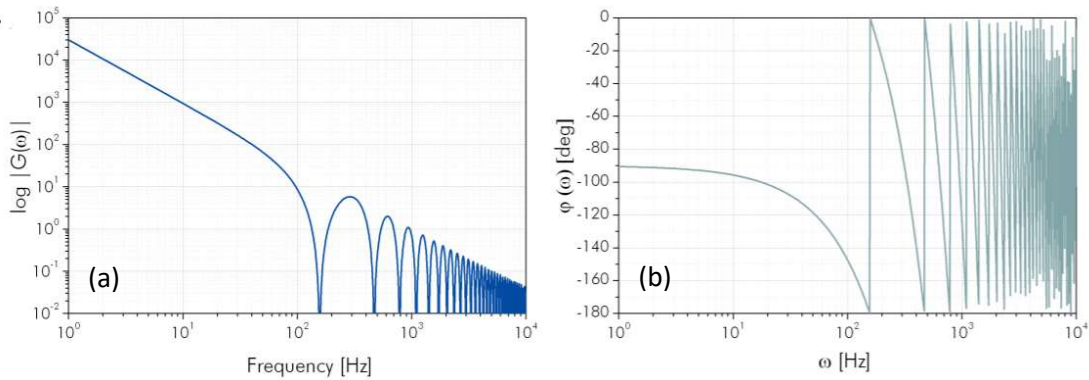
Figure A.3: Bode plots for the gain magnitude (a) and phase (b), here for a 920 km fiber interferometer (round-trip delay $\sim$10ms). At multiple integers of $1/4\tau$ the gain amplitude is zero and the phase diverges. Taken from[100].

According to Eqs. A.24 and A.25, the magnitude of the gain becomes zero and the phase becomes $-\pi$ when f= $\omega/2\pi$= n/4τ, where n is an integer. That means that $G_0(\omega)$ and especially

$F(\omega)$ have to be chosen carefully to assure a stable loop operation by filtering specific frequencies. Actually, we can compensate for phase noise when $\phi \leq \pi/2$, and hence for frequencies below $f = 1/2\tau$. Oscillations in the compensated phase noise occur if we try to compensate for noises at Fourier frequencies $f > 1/4\tau$, as shown in Fig. A.3.

However, even for an optimized loop filter, the one-pass phase fluctuations are not perfectly canceled due to the large delay. This is denoted as *delay unsuppressed fiber noise*. The residual phase error $\tilde{\varphi}_{remote}(\omega)$ at the remote end is given by subtracting the compensated one-pass phase noise from the uncompensated one. Here, the compensated phase noise is given by

$$\tilde{\varphi}_{remote}(\omega) = \tilde{\varphi}_{fiber}(\omega) - H(\omega)e^{-i\omega\tau}\tilde{\varphi}_{local}(\omega) = \tag{A.26}$$

$$= \tilde{\varphi}_{fiber}(\omega) - \frac{G(\omega)}{1+G(\omega)}\frac{1}{2\cos{(\omega\tau)}}\tilde{\varphi}_{fiber,RT}(\omega).$$

As mentioned above, the spectral power density is $S(\omega) = |\tilde{\varphi}(\omega)|^2$, so

$$S_{remote}(\omega) = \left|\tilde{\varphi}_{fiber}(\omega) - \frac{G(\omega)}{1+G(\omega)}\frac{1}{2\text{ co }(\omega\tau)}\tilde{\varphi}_{fiber,RT}(\omega)\right|^2. \tag{A.27}$$

By some algebraic manipulation (see [102]), and under the assumption of equal propagation times $\tau_1 = \tau_2 = 1/2\tau_{RT}$ one can derive the corresponding spectral power density

$$S_{remote}(\omega) = \frac{(\omega\tau)^2}{3}S_{fiber}(\omega) = S_{remote}(f) = \frac{4\pi^2}{3}\left(f\frac{L}{c_n}\right)^2 S_{fiber}(f). \tag{A.28}$$

This term becomes non-negligible while the length of the fiber is long enough in comparison to f/c_n.

References

1.   Ramsey NF. History of early atomic clocks. Metrologia 2005;42(3):S1.

2.   Lombardi MA. The evolution of time measurement, part 3: atomic clocks [Recalibration]. IEEE Instrumentation & Measurement Magazine 2011;14(6):46-49.

3.   Essen L, Parry JVL. An atomic standard of frequency and time interval: a caesium resonator. Nature 1955;176(4476):280-282.

4.   2020 BIPM - measurement units. <https://www.bipm.org/en/measurement-units/>.

5.   Nicholson TL, Campbell SL, Hutson RB, Marti GE, Bloom BJ, McNally RL, Zhang W, Barrett MD, Safronova MS, Strouse GF. Systematic evaluation of an atomic clock at 2×10^{-18} total uncertainty. Nature communications 2015;6(1):1-8.

6.   Riley WJ. Handbook of frequency stability analysis. US Department of Commerce, National Institute of Standards and Technology ; 2008.

7.   Riehle F. Frequency standards: basics and applications. John Wiley & Sons; 2006.

8.   Lemke ND. Optical Lattice Clock with Spin-1/2 Ytterbium Atoms. Diss. 2012.

9.   Weyers S, Gerginov V, Kazda M, Rahm J, Lipphardt B, Dobrev G, Gibble K. Advances in the accuracy, stability, and reliability of the PTB primary fountain clocks. Metrologia 2018;55(6):789.

10.   Hendricks RJ, Ozimek F, Szymaniec K, Dunst P, Nagorny B, Nawrocki J, Beattie S, Jian B, Chen W, Gibble K. Design and performance of Cs fountain frequency standards constructed for metrology laboratories. 2017. IEEE. p 477-478.

11.   Fortier T, Baumann E. 20 years of developments in optical frequency comb technology and applications. Communications Physics 2019;2(1).

12.   Riehle F. Towards a redefinition of the second based on optical atomic clocks. Comptes Rendus Physique 2015;16(5):506-515.

13.   Lodewyck J. On a definition of the SI second with a set of optical clock transitions. Metrologia 2019;56(5):055009.

14.   2020 ROCIT: Robust optical clocks for international timescales. <http://empir.npl.co.uk/rocit/>.

15.   Kobayashi T, Akamatsu D, Hosaka K, Hisai Y, Wada M, Inaba H, Suzuyama T, Hong F-L, Yasuda M. Demonstration of the nearly continuous operation of an ^{171}Yb optical lattice clock for half a year. Metrologia 2020;57(6):065021.

16.   Takamoto M, Ushijima I, Ohmae N, Yahagi T, Kokado K, Shinkai H, Katori H. Test of general relativity by a pair of transportable optical lattice clocks. Nature Photonics 2020:1-5.

17.   Delva P, Lodewyck J, Bilicki S, Bookjans E, Vallet G, Le Targat R, Pottie PE, Guerlin C, Meynadier F, Le Poncin-Lafitte C. Test of special relativity using a fiber network of optical clocks. Physical review letters 2017;118(22):221102.

18.   Bongs K, Singh Y. Earth-based clocks test general relativity. Nature Photonics 2020;14(7):408-409.

19.   Zhou Z, Margalit Y, Rohrlich D, Japha Y, Folman R. Quantum complementarity of clocks in the context of general relativity. Classical and Quantum Gravity 2018;35(18):185003.

20.   Riehle F. Optical clock networks. Nature Photonics 2017;11(1):25.

21.   Blatt S, Ludlow AD, Campbell GK, Thomsen JW, Zelevinsky T, Boyd MM, Ye J, Baillard X, Fouché M, Le Targat R. New limits on coupling of fundamental constants to gravity using Sr-87 optical lattice clocks. Physical Review Letters 2008;100(14):140801.

22. Roberts BM, Delva P, Al-Masoudi A, Amy-Klein A, Baerentsen C, Baynham CFA, Benkler E, Bilicki S, Bize S, Bowden W. Search for transient variations of the fine structure constant and dark matter using fiber-linked optical atomic clocks. New Journal of Physics 2020;22(9):093010.

23. Daykin T, Bradley C, Panelli G, Maddox T, Roberts B, Blewitt G, Derevianko A. Update on the search for dark matter transient signatures using the GPS atomic clocks. Bulletin of the American Physical Society 2020.

24. Kennedy CJ, Oelker E, Robinson JM, Bothwell T, Kedar D, Milner WR, Marti GE, Derevianko A, Ye J. Precision metrology meets cosmology: improved constraints on ultralight dark matter from atom-cavity frequency comparisons. Physical Review Letters 2020;125(20):201302.

25. Grotti J, Koller S, Vogt S, Häfner S, Sterr U, Lisdat C, Denker H, Voigt C, Timmen L, Rolland A. Geodesy and metrology with a transportable optical clock. Nature Physics 2018;14(5):437-441.

26. Koller SB, Grotti J, Al-Masoudi A, Dörscher S, Häfner S, Sterr U, Lisdat C. Transportable optical lattice clock with 7×10^{-17} uncertainty. Physical review letters 2017;118(7):073601.

27. Hollberg L, Oates CW, Curtis EA, Ivanov EN, Diddams SA, Udem T, Robinson HG, Bergquist JC, Rafac RJ, Itano WM. Optical frequency standards and measurements. IEEE Journal of Quantum Electronics 2001;37(12):1502-1513.

28. Katori H. Optical lattice clocks and quantum metrology. Nature Photonics 2011;5(4):203-210.

29. Huntemann N, Sanner C, Lipphardt B, Tamm C, Peik E. Single-ion atomic clock with 3×10^{-18} systematic uncertainty. Physical review letters 2016;116(6):063001.

30. McGrew WF, Zhang X, Fasano RJ, Schäffer SA, Beloy K, Nicolodi D, Brown RC, Hinkley N, Milani G, Schioppo M. Atomic clock performance enabling geodesy below the centimetre level. Nature 2018;564(7734):87-90.

31. Tan TR, Kaewuam R, Arnold KJ, Chanu SR, Zhang Z, Safronova MS, Barrett MD. Suppressing inhomogeneous broadening in a lutetium multi-ion optical clock. Physical review letters 2019;123(6):063201.

32. Beloy K, Hinkley N, Phillips NB, Sherman JA, Schioppo M, Lehman J, Feldman A, Hanssen LM, Oates CW, Ludlow AD. Atomic clock with $1{\times}10^{-18}$ room-temperature blackbody stark uncertainty. Physical review letters 2014;113(26):260801.

33. Madjarov IS, Cooper A, Shaw AL, Covey JP, Schkolnik V, Yoon TH, Williams JR, Endres M. An atomic-array optical clock with single-atom readout. Physical Review X 2019;9(4):041052.

34. Band YB, Vardi A. Collisional shifts in optical-lattice atom clocks. Physical Review A 2006;74(3):033807.

35. Ludlow AD, Boyd MM, Ye J, Peik E, Schmidt PO. Optical atomic clocks. Reviews of Modern Physics 2015;87(2):637.

36. Bilicki S. Strontium optical lattice clocks: clock comparisons for timescales and fundamental physics applications. Diss. 2017.

37. Boyd MM, Zelevinsky T, Ludlow AD, Foreman SM, Blatt S, Ido T, Ye J. Optical atomic coherence at the 1-second time scale. science 2006;314(5804):1430-1433.

38. Ning C, Min Z, Hai-Qin C, Su F, Liang-Yu H, Xiao-Hang Z, Qi G, Yan-Yi J, Zhi-Yi B, Long-Sheng M. Clock-transition spectrum of ^{171}Yb atoms in a one-dimensional optical lattice. Chinese Physics B 2013;22(9):090601.

39. Taichenachev AV, Yudin VI, Oates CW, Hoyt CW, Barber ZW, Hollberg L. Magnetic field-induced spectroscopy of forbidden optical transitions with application to lattice-based optical atomic clocks. Physical review letters 2006;96(8):083001.

40. Ovsiannikov VD, Pal'chikov VG, Taichenachev AV, Yudin VI, Katori H, Takamoto M. Magic-wave-induced $^1S_0- {}^3P_0$ transition in even isotopes of alkaline-earth-metal-like atoms. Physical Review A 2007;75(2):020501.

41. Hong T, Cramer C, Nagourney W, Fortson EN. Optical clocks based on ultranarrow three-photon resonances in alkaline earth atoms. Physical review letters 2005;94(5):050801.

42. Takamoto M, Ushijima I, Das M, Nemitz N, Ohkubo T, Yamanaka K, Ohmae N, Takano T, Akatsuka T, Yamaguchi A. Frequency ratios of Sr, Yb, and Hg based optical lattice clocks and their applications. Comptes Rendus Physique 2015;16(5):489-498.

43. Bothwell T, Kedar D, Oelker E, Robinson JM, Bromley SL, Tew WL, Ye J, Kennedy CJ. JILA SrI optical lattice clock with uncertainty of. Metrologia 2019;56(6):065004.

44. Ushijima, I., Takamoto, M., Das, M. et al. Cryogenic optical lattice clocks. Nature Photonics 2015;9(3): 185–189.

45. Ablewski P, Bober M, Zawada M. Reducing blackbody radiation shift uncertainty in optical lattice clocks. 2018. IEEE. p 352-355.

46. Kawasaki A. Towards spin squeezed ^{171}Yb atomic clock beyond the standard quantum limit. Diss. 2017.

47. Milani G. Realization of advanced ^{171}Yb optical lattice frequency standard. Diss. 2018.

48. Young AW, Eckner WJ, Milner WR, Kedar D, Norcia MA, Oelker E, Schine N, Ye J, Kaufman AM. Half-minute-scale atomic coherence and high relative stability in a tweezer clock. Nature 2020;588(7838):408-413.

49. Akerman N, Ozeri R. Atomic combination clocks. New Journal of Physics 2018;20(12):123026.

50. Metcalf HJ, van der Straten P. Laser cooling and trapping of atoms. JOSA B 2003;20(5):887-908.

51. Katori H, Ido T, Kuwata–Gonokami M. Optimal design of dipole potentials for efficient loading of Sr atoms. Journal of the Physical Society of Japan 1999;68(8):2479-2482.

52. Taichenachev AV, Yudin VI, Ovsiannikov VD, Pal'Chikov VG, Oates CW. Frequency shifts in an optical lattice clock due to magnetic-dipole and electric-quadrupole transitions. Physical review letters 2008; 101(19): 193601.

53. Barber ZW, Stalnaker JE, Lemke ND, Poli N, Oates CW, Fortier TM, Diddams SA, Hollberg L, Hoyt CW, Taichenachev AV. Optical lattice induced light shifts in an Yb atomic clock. Physical Review Letters 2008;100(10):103002.

54. Häffner H, Roos CF, Blatt R. Quantum computing with trapped ions. Physics reports 2008;469(4):155-203.

55. Eschner J, Morigi G, Schmidt-Kaler F, Blatt R. Laser cooling of trapped ions. JOSA B 2003;20(5):1003-1015.

56. Diedrich F, Bergquist JC, Itano WM, Wineland DJ. Laser cooling to the zero-point energy of motion. Physical Review Letters 1989;62(4):403.

57. Brown RC, Phillips NB, Beloy K, McGrew WF, Schioppo M, Fasano RJ, Milani G, Zhang X, Hinkley N, Leopardi H. Hyperpolarizability and operational magic wavelength in an optical lattice clock. Physical Review Letters 2017;119(25):253001.

58. Inguscio M, Fallani L. Atomic physics: precise measurements and ultracold matter. OUP Oxford; 2013.

59. Ramsey NF. A molecular beam resonance method with separated oscillating fields. Physical Review 1950;78(6):695.

60. Zanon-Willette T, Minissale M, Yudin VI, Taichenachev AV. Composite pulses in Hyper-Ramsey spectroscopy for the next generation of atomic clocks. 2016. p 012057.

61. Pizzocaro M, Thoumany P, Rauf B, Bregolin F, Milani G, Clivati C, Costanzo GA, Levi F, Calonico D. Absolute frequency measurement of the– transition of 171Yb. Metrologia 2017;54(1):102.

62. Schioppo M, Brown RC, McGrew WF, Hinkley N, Fasano RJ, Beloy K, Yoon TH, Milani G, Nicolodi D, Sherman JA. Ultrastable optical clock with two cold-atom ensembles. Nature Photonics 2017;11(1):48.

63. Saskin S, Wilson JT, Grinkemeyer B, Thompson JD. Narrow-line cooling and imaging of ytterbium atoms in an optical tweezer array. Physical review letters 2019;122(14):143002.

64. Rathod KD. Continuous Beam of Laser-Cooled Ytterbium Atoms for Precision Measurements. Diss. 2017.

65. Habermann CE, Daane AH. Vapor pressures of the rare-earth metals. The Journal of Chemical Physics 1964;41(9):2818-2827.

66. Schioppo M, Poli N, Prevedelli M, Falke S, Lisdat C, Sterr U, Tino GM. A compact and efficient strontium oven for laser-cooling experiments. Review of Scientific Instruments 2012;83(10):103101.

67. Zhao P-Y, Xiong Z-X, Liang J, He L-X, Lu B-L. Magneto-Optical Trapping of Ytterbium Atoms with a 398.9 nm Laser. Chinese Physics Letters 2008;25(10):3631-3634.

68. Ramsey N. Molecular beams. Oxford University Press; 1985.

69. Dörscher S, Thobe A, Hundt B, Kochanke A, Le Targat R, Windpassinger P, Becker C, Sengstock K. Creation of quantum-degenerate gases of ytterbium in a compact 2D-/3D-magneto-optical trap setup. Review of Scientific Instruments 2013;84(4):043109.

70. Degiorgio V. Phase shift between the transmitted and the reflected optical fields of a semireflecting lossless mirror is $\pi/2$. American Journal of Physics 1980;48(1):81-81.

71. Nickerson M. A review of Pound-Drever-Hall laser frequency locking. JILA, University of Colorado and Nist 2019.

72. Black ED. An introduction to Pound–Drever–Hall laser frequency stabilization. American journal of physics 2001;69(1):79-87.

73.   Matei DG, Legero T, Häfner S, Grebing C, Weyrich R, Zhang W, Sonderhouse L, Robinson JM, Ye J, Riehle F. 1.5 μm lasers with sub-10 mHz linewidth. Physical review letters 2017;118(26):263202.

74.   Pollnau M, Eichhorn M. Spectral coherence, Part I: Passive-resonator linewidth, fundamental laser linewidth, and Schawlow-Townes approximation. Progress in Quantum Electronics 2020;72:100255.

75.   Schawlow AL, Townes CH. Infrared and optical masers. Physical Review 1958;112(6):1940.

76.   Milani G, Rauf B, Barbieri P, Bregolin F, Pizzocaro M, Thoumany P, Levi F, Calonico D. Multiple wavelength stabilization on a single optical cavity using the offset sideband locking technique. Optics letters 2017;42(10):1970-1973.

77.   Barré N, Romanelli M, Lebental M, Brunel M. Waves and rays in plano-concave laser cavities: I. Geometric modes in the paraxial approximation. European Journal of Physics 2017;38(3):034010.

78.   Pizzocaro M, Costanzo GA, Godone A, Levi F, Mura A, Zoppi M, Calonico D. Realization of an ultrastable 578-nm laser for an Yb lattice clock. IEEE transactions on ultrasonics, ferroelectrics, and frequency control 2012;59(3):426-431.

79.   Pizzocaro M, Calonico D, Pastor PC, Catani J, Costanzo GA, Levi F, Lorini L. Efficient frequency doubling at 399 nm. Applied optics 2014;53(16):3388-3392.

80.   Hansch TW, Couillaud B. Laser frequency stabilization by polarization spectroscopy of a reflecting reference cavity. Optics communications 1980;35(3):441-444.

81.   Boyd GD, Kleinman DA. Parametric interaction of focused Gaussian light beams. Journal of Applied Physics 1968;39(8):3597-3639.

82.   Patimisco P, Sampaolo A, Tittel FK, Spagnolo V. Mode matching of a laser-beam to a compact high finesse bow-tie optical cavity for quartz enhanced photoacoustic gas sensing. Sensors and Actuators A: Physical 2017;267:70-75.

83. Hannig S, Mielke J, Fenske JA, Misera M, Beev N, Ospelkaus C, Schmidt PO. A highly stable monolithic enhancement cavity for second harmonic generation in the ultraviolet. Review of Scientific Instruments 2018;89(1):013106.

84. Pizzocaro M, Bregolin F, Barbieri P, Rauf B, Levi F, Calonico D. Absolute frequency measurement of the $^1S_0$–$^3P_0$ transition of ^{171}Yb with a link to international atomic time. Metrologia 2020;57(3):035007.

85. Bregolin F. ^{171}Yb optical frequency standards towards the redefinition of the second. Diss. 2019.

86. Saliba SD, Junker M, Turner LD, Scholten RE. Mode stability of external cavity diode lasers. Applied optics 2009;48(35):6692-6700.

87. Ito I, Silva A, Nakamura T, Kobayashi Y. Stable CW laser based on low thermal expansion ceramic cavity with 4.9 mHz/s frequency drift. Optics Express 2017;25(21):26020-26028.

88. Yu D-H, Park CY, Lee W-K, Lee S, Park SE, Mun J, Lee S-B, Kwon TY. An Yb optical lattice clock: Current status at KRISS. Journal of the Korean Physical Society 2013;63(4):883-889.

89. Kobayashi T, Akamatsu D, Hisai Y, Tanabe T, Inaba H, Suzuyama T, Hong F-L, Hosaka K, Yasuda M. Uncertainty Evaluation of an ^{171}Yb Optical Lattice Clock at NMIJ. IEEE Transactions on Ultrasonics, Ferroelectrics, and Frequency Control 2018;65(12):2449-2458.

90. Ye J, Cundiff ST. Femtosecond optical frequency comb: principle, operation and applications. Springer Science & Business Media; 2005.

91. Holman, K. W. Distribution of an ultrastable frequency reference using optical frequency combs. Diss. 2005.

92. Zimmermann M, Gohle C, Holzwarth R, Udem T, Hänsch TW. Optical clockwork with an offset-free difference-frequency comb: accuracy of sum- and difference-frequency generation. Optics letters 2004;29(3):310-312.

93. Oelker E, Hutson RB, Kennedy CJ, Sonderhouse L, Bothwell T, Goban A, Kedar D, Sanner C, Robinson JM, Marti GE. Demonstration of 4.8×10^{-17}

stability at 1 s for two independent optical clocks. Nature Photonics 2019;13(10):714-719.

94. Oelker E, Hutson RB, Kennedy CJ, Sonderhouse L, Bothwell T, Goban A, Kedar D, Sanner C, Robinson JM, Marti GE. Optical clock intercomparison with 6×10^{-19} precision in one hour. arXiv preprint arXiv:1902.02741 2019.

95. Shen B, Chang L, Liu J, Wang H, Yang Q-F, Xiang C, Wang RN, He J, Liu T, Xie W. Integrated turnkey soliton microcombs. Nature 2020;582(7812):365-369.

96. Newman ZL, Maurice V, Drake T, Stone JR, Briles TC, Spencer DT, Fredrick C, Li Q, Westly D, Ilic BR. Architecture for the photonic integration of an optical atomic clock. Optica 2019;6(5):680-685.

97. Diddams SA, Vahala K, Udem T. Optical frequency combs: Coherently uniting the electromagnetic spectrum. Science 2020;369(6501).

98. Lisdat C, Grosche G, Quintin N, Shi C, Raupach SMF, Grebing C, Nicolodi D, Stefani F, Al-Masoudi A, Dörscher S. A clock network for geodesy and fundamental science. Nature communications 2016;7(1):1-7.

99. Khabarova KY, Kalganova ES, Kolachevsky NN. Accurate frequency and time dissemination in the optical domain. Physics-Uspekhi 2018;61(2):203.

100. Predehl K. A 920-kilometer optical fiber link for frequency metrology at the 19th decimal place. Diss. 2012.

101. Raupach SMF, Koczwara A, Grosche G. Brillouin amplification supports 1×10^{-20} uncertainty in optical frequency transfer over 1400 km of underground fiber. Physical Review A 2015;92(2):021801.

102. Terra O. Dissemination of ultra-stable optical frequencies over commercial fiber networks. Diss. 2010.

103. Gardner FM. Phaselock techniques. John Wiley & Sons; 2005.